ENVIRONMENTAL RESEARCH
LETTERS

CrossMark

OPEN ACCESS

RECEIVED
27 April 2022

REVISED
29 August 2022

ACCEPTED FOR PUBLICATION
7 September 2022

PUBLISHED
16 September 2022

LETTER

Multi-decadal monsoon characteristics and glacier response in High Mountain Asia

T E Shaw[1,*], E S Miles[1], D Chen[2], A Jouberton[1,3], M Kneib[1,3], S Fugger[1,3], T Ou[2], H-W Lai[2], K Fujita[4], W Yang[5,6], S Fatichi[7] and F Pellicciotti[1,8]

1 High Mountain Glaciers and Hydrology Group, Swiss Federal Institute, WSL, Birmensdorf, Switzerland
2 Department of Earth Sciences, University of Gothenburg, Gothenburg, Sweden
3 Institute of Environmental Engineering, ETH Zurich, 8093 Zurich, Switzerland
4 Graduate School of Environmental Studies, Nagoya University, Nagoya, Japan
5 Key Laboratory of Tibetan Environment Changes and Land Surface Processes, Institute of Tibetan Plateau Research, Chinese Academy of Sciences, Beijing, People's Republic of China
6 CAS Center for Excellence in Tibetan Plateau Earth Sciences, Beijing, People's Republic of China
7 Department of Civil and Environmental Engineering, National University of Singapore, Singapore
8 Department of Geography, Northumbria University, Newcastle, United Kingdom
* Author to whom any correspondence should be addressed.

E-mail: thomas.shaw@wsl.ch

Keywords: glacier, long-term mass balance, monsoon, snowfall

Supplementary material for this article is available online

Abstract

Glacier health across High Mountain Asia (HMA) is highly heterogeneous and strongly governed by regional climate, which is variably influenced by monsoon dynamics and the westerlies. We explore four decades of glacier energy and mass balance at three climatically distinct sites across HMA by utilising a detailed land surface model driven by bias-corrected Weather Research and Forecasting meteorological forcing. All three glaciers have experienced long-term mass losses (ranging from -0.04 ± 0.09 to -0.59 ± 0.20 m w.e. a^{-1}) consistent with widespread warming across the region. However, complex and contrasting responses of glacier energy and mass balance to the patterns of the Indian Summer Monsoon were evident, largely driven by the role snowfall timing, amount and phase. A later monsoon onset generates less total snowfall to the glacier in the southeastern Tibetan Plateau during May–June, augmenting net shortwave radiation and affecting annual mass balance (-0.5 m w.e. on average compared to early onset years). Conversely, timing of the monsoon's arrival has limited impact for the Nepalese Himalaya which is more strongly governed by the temperature and snowfall amount during the core monsoon season. In the arid central Tibetan Plateau, a later monsoon arrival results in a 40 mm (58%) increase of May–June snowfall on average compared to early onset years, likely driven by the greater interaction of westerly storm events. Meanwhile, a late monsoon cessation at this site sees an average 200 mm (192%) increase in late summer precipitation due to monsoonal storms. A trend towards weaker intensity monsoon conditions in recent decades, combined with long-term warming patterns, has produced predominantly negative glacier mass balances for all sites (up to 1 m w.e. more mass loss in the Nepalese Himalaya compared to strong monsoon intensity years) but sub-regional variability in monsoon timing can additionally complicate this response.

1. Introduction

Melt water from glacier ice and snow is a vital component of the world's water towers which serve billions of people globally (Immerzeel *et al* 2020), particularly in the lowland regions surrounding High Mountain Asia (HMA). Glacier melt at the world's 'Third Pole' can significantly modify regional hydrology and buffer periods of very dry conditions (Pritchard *et al* 2017, Viviroli *et al* 2020), promote natural hazards such as glacier lake outburst floods (Veh *et al* 2020) and contribute to global sea level rise (Zemp et al 2019). Accordingly, glacier health in HMA is highly important to water security, though it is highly heterogeneous in space and largely unsustainable (Sakai and Fujita 2017, Hugonnet et al 2021, Miles et al 2021). This high heterogeneity is governed, at least in part, by the dynamics and varying extent of the Indian Summer Monsoon (hereafter 'monsoon'), and intrusion of mid-latitude westerlies (Mölg et al 2014, Forsythe et al 2017, Li et al 2018). The monsoon controls the summer-season energy-mass-balance of HMA glaciers due to the coincidence of warm, overcast and wet weather conditions (Fugger et al 2022), and the timing of monsoon arrival, as well as its duration, has been shown to control the surface energy and mass balance of some mountain glaciers due to its determination of the phase and intensity of early summer precipitation (Mölg et al 2012). However, westerly intrusions during the pre-monsoon period can also greatly affect the annual glacier mass balance (Mölg et al 2014), particularly for regions where the monsoon accounts for a smaller proportion of the total annual precipitation (figure 1(a)).

Changing monsoon dynamics over the past few decades (Bollasina et al 2011, Ha et al 2020) have implications for changing spatio-temporal patterns of seasonal precipitation across HMA (Zhu et al 2020). For example, the suggested weakening of the South Asian Summer Monsoon since the 1950s, exacerbated by anthropogenic aerosol emissions, has resulted in observed summertime drying across much of northern India and towards the Nepalese Himalaya (Bollasina et al 2011). Conversely, a tendency towards earlier monsoon onset over the Bay of Bengal can be linked to increases in May precipitation in the southeastern Tibetan Plateau (Zhu et al 2020, Jouberton et al 2022), accelerating wetting and greening in recent decades (Zhang et al 2017). While the full mechanisms remain elusive (e.g. Saha and Ghosh 2019), the complex interaction of temperature and precipitation changes have important implications for both glacier accumulation and ablation, largely through precipitation phase and albedo (Jouberton et al 2022). While it has been established that the dynamics of the summer monsoon, as well as long-term climatic trends, local geography (Yao et al 2012, Maussion et al 2014, Mölg et al 2014, Zhu et al 2018, de Kok et al 2020) and even land use change (de Kok et al 2018) all contribute to the heterogeneity of glacier mass balance in HMA, responses of glaciers' mass balances in different sub-regions to multi-decadal variability in the monsoon remains largely unexplored (Arndt et al 2021).

We utilise a recently developed, 9 km resolution atmospheric model simulation (Ou et al 2020) in order to unravel the multi-decadal response of mountain glacier energy-mass-balance to the changes of the summer monsoon within distinct sites across HMA. By combining recent advances in atmospheric and land surface modelling with robust bias-correction techniques and detailed ground-based meteorological information, we aim to address the following specific questions: (1) How has the timing, duration and intensity of the summer monsoon evolved since the 1980s and what is its impact upon the spatial-temporal patterns of summer climate across HMA?; (2) How has energy and mass balance of three mountain glaciers in HMA responded to changes in monsoon dynamics over four decades?; and (3) What are the main drivers of these changes in distinct climatic sub-regions?

2. Data and methods

2.1. Study area

The present study focuses on three debris-free, mountain glaciers distributed across distinct climatic sub-regions of HMA (figure 1). Yala Glacier (28.237° N 85.619° E) is a small, 1.5 km^2 glacier situated in Langtang Valley, Nepal which has been the subject of long-term mass balance campaigns (e.g. Fujita et al 1998, Baral et al 2014, Stumm et al 2021, Sunako et al 2020) as well as the focus of research on energy balance and surface processes (Stigter et al 2018, Litt et al 2019). Parlung Glacier Number 4 (29.245° N 96.928° E, hereafter 'Parlung 4' or 'PAR4') is a 11.7 km^2, spring-type accumulation glacier in the southeastern Tibetan Plateau. The glacier has been the focus of several recent studies that have explored meteorological processes (Yang et al 2011, Shaw et al 2021), glacier dynamics (Yang et al 2020) and energy/mass balance (Zhu et al 2015, 2018, Jouberton et al 2022). Mugagangqiong Glacier (34.248° N 87.490° E, hereafter 'MUGA' for tables and figures) is a 2 km^2 glacier in the arid central Tibetan Plateau. The glacier has been the focus of few studies, typically regarding ice cores and historic atmospheric dust concentrations (Feng et al 2020), though is also one of several investigation sites established across the Tibetan Plateau in the last decade (Yang et al 2022). The site specific information of each glacier is given in table 1.

2.2. Datasets

We utilise hourly meteorological data from off- and on-glacier automatic weather stations (AWSs) at each study site (figure 1) to bias-correct the long-term forcing data. AWS data are available for the period 2012–2019 for Parlung 4 and Yala (figure S7), and 2015–2019 for Mugagangqiong. At each site, distributed ablation stake data are available, spanning partial (Parlung 4) or full elevation ranges (Yala/Mugagangqiong) of the glaciers.

Gridded atmospheric data for HMA (1980–2019) are extracted from simulations carried out with the weather research and forecasting (WRF) model at 9 km horizontal resolution (Ou et al 2020, Sun et al 2021). The WRF model (v. 3.7.1) is driven by three-hourly ERA5 pressure and surface level variables.

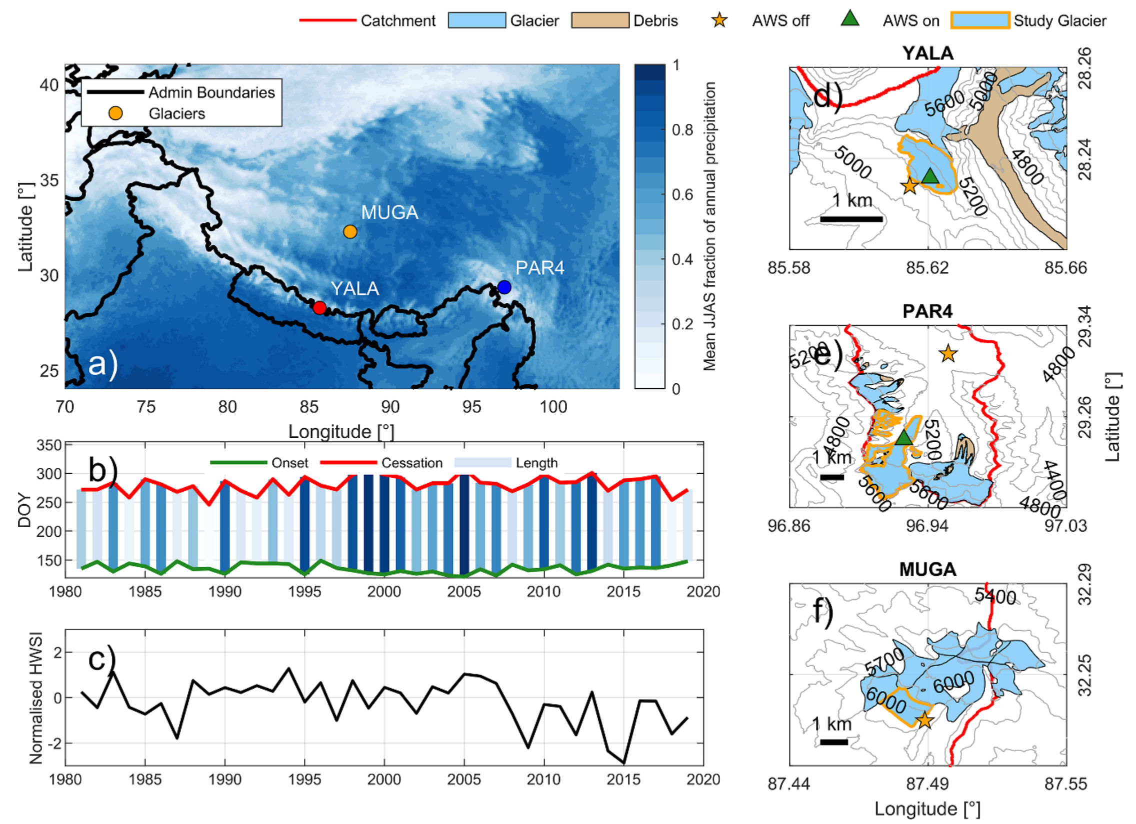

Figure 1. The monsoon characteristics and location of the three glacier study sites across HMA. (a) indicates the mean summer (June–September) fraction of annual total precipitation across HMA derived from WRF (1981–2019). The onset and cessation dates derived for the Bay of Bengal region are indicated in (b). (c) shows the normalised June–September horizontal wind shear index (HWSI—section 2.5) which is used here as a measure of interannual monsoon intensity. Study sites are shown for YALA (d), PAR4 (e) and MUGA (f), with the study glaciers highlighted in orange and the catchment delineations shown in red.

Table 1. Summary statistics of the three glacier study sites. Geometric statistics are based upon the median date of the model simulations (2000) and temperature and precipitation information are based upon the glacier-wide average for the whole period (1981–2019).

SITE	Yala Glacier (YALA)	Parlung Glacier No. 4 (PAR4)	Mugagangqiong Glacier (MUGA)
Area (km^2)	1.5	11.7	1.9
Elevation range (m a.s.l.)	5120–5615	4700–5600	5600–6100
Mean slope (°)	22	8	11
Mean summer (June–September) air temperature (°C)	0.1	1.0	−1.2
Mean summer (June–September) precipitation total (mm)	1172	1476	413
Fraction of solid precipitation in summer (June–September)	0.87	0.7	0.95

Spectral nudging is applied to geopotential, horizontal winds and temperatures above the approximate planetary boundary layer top as described in Ou *et al* (2020). The model applies no convection scheme, as found by Ou *et al* (2020) to produce the most appropriate frequency and initiation timing for short (1–3 h) and long (>6 h) precipitation events compared with observations. The full model details are provided in table S1.

2.3. Derivation of meteorological forcing

WRF data are extracted from the nearest corresponding point to each off-glacier AWS (figure 1) which provides a longer series of un-interrupted data for bias correction. Data gaps in the AWS records are ignored such that only hours with all energy balance variables available (air temperature, relative humidity, radiative fluxes, wind speed, air pressure and precipitation) are considered for bias correction. We apply a multivariate bias-correction following Cannon (2018) that combines quantile delta mapping with random orthogonal rotations to match the multivariate distributions of both the WRF and AWS data. This approach has been shown to outperform univariate bias correction methods when used in hydrological modelling applications (Meyer *et al* 2019, Faghih *et al* 2021) and we consider it suitable for correction of cross-correlated variables in complex, high mountain regions. Using at least 5 years of AWS data at each site, we generate quantile correction factors that are applied to the full time series of WRF data at the extracted pixel of interest. The variable correlations and long-term trends are preserved in the bias-corrected data and found to be consistent with long-term climate stations for the different sub-regions (see SI).

With the bias-corrected time series of WRF data, we extrapolate the variables of interest to the elevations of the glaciers (table 1) using empirically determined lapses rates. Multiple station observations available in Langtang Valley (Steiner *et al* 2021) were used to generate hourly-monthly temperature lapse rates, and temperatures were adjusted for the boundary layer cooling effect of Yala using the on-glacier AWS temperatures. For Parlung 4, we consider the off-glacier temperature lapse rates derived from the data of Shaw *et al* (2021) and as applied by Jouberton *et al* (2022). Precipitation is distributed similarly to Jouberton *et al* (2022) who applied a correction factor of 1.75 and gradient of 14% 100 m^{-1} to account for the distinct precipitation regime between valley and the glacier. Given the differences in model forcing and structure, we recalibrate these gradients for the current study against ablation stakes and an upper elevation ice core record (table S3). No on-glacier AWS exists for Mugagangqiong, though the off-glacier AWS is very close to the glacier and is considered to experience a partial cooling effect associated with the glacier boundary layer (e.g. Shaw *et al* 2021). For this site, we distribute temperature considering the lapse rates derived for the Mugagangqiong basin (Yang *et al* 2022). Precipitation gradients and correction factors were calibrated against multi-year ablation stake observations. Use of a precipitation correction factor implicitly accounts for unknown quantities of AWS pluviometer under-catch that were not represented by the bias correction of WRF data.

2.4. Energy/mass balance modelling

We simulate hourly glacier energy and mass balance using the snow, ice and hydrological components of the Tethys-Chloris (T&C) land surface model (Fatichi *et al* 2012, 2021, Mastrotheodoros *et al* 2020, Botter *et al* 2021, Fyffe *et al* 2021, Fugger *et al* 2022) applied in a semi-distributed manner using 50 m intervals for the full range of elevations at each site (table 1). T&C's cryospheric component constitutes a fully-physical energy balance model that simulates the energy fluxes of the ice/snow surface and subsurface, including sublimation. Precipitation phase partitions are dynamically considered based upon the air temperature, relative humidity and air pressure (Ding *et al* 2014) and utilised directly in the albedo model developed by Ding *et al* (2017). We adjust the mean incoming radiative fluxes and snow avalanching according to the topography of each elevation band and the modelled elevational mass balances are area-weighted by time-evolving hypsometries from co-registered DEMs and glacier outlines since the 1970s to produce a continuous time-series of glacier mass balance (figures S16–S18). Avalanching on Parlung 4 Glacier was modelled given a fully-distributed TOPKAPI-ETH simulation of the catchment by Jouberton *et al* (2022) and used to update end-of-year mass balances for the appropriate elevation band. The model is run for 1980–2019 and the results analysed for 1981–2019, taking 1980 as a spin-up year. Temperature and precipitation distribution parameters are perturbed in 1000 Monte Carlo simulations to provide an estimate of mass balance uncertainty. More details about the model are provided in the supplementary information section 2.3.

2.5. Characterisation of the moonsoon

As an estimate of the regional onset of the monsoon, we consider the horizontal wind shear index (HWSI) of Prasad and Hayashi (2005), as previously considered in studies of this type (Mölg *et al* 2012, Li *et al* 2018). Due to the large scale feature of the monsoon, we utilise ERA5 850 hPa zonal wind data to derive this index. Alternative means to classify local monsoon timing (e.g. Bombardi *et al* 2020, Brunello *et al* 2020) resulted in spatial-temporal inconsistencies between study sites for certain years and were thus not applied here. In this study, we analysed the results of the glacier energy- and mass-balance in relation to the monsoon (i) onset dates; (ii) cessation dates; (iii) duration and; (iv) intensity (figure S27). Moreover, we analyse the May–June precipitation amount and phase during the pre-monsoon to monsoon transition and examine its potential influence on the glacier energy and mass balance during the summer. The relevance of the monsoon characteristics is then placed into the context of the prevailing meteorological conditions for the summer. Early (late) onset/cessation dates are considered as those which are less (greater) than one standard deviation from the mean of the whole period and monsoon intensity is taken as the normalised mean HWSI for June–September.

3. Results

3.1. Patterns of monsoon climate

The regional monsoon index reveals a tendency towards an earlier monsoon onset (−3.3 days dec^{-1}) and later cessation (+11.6 days dec^{-1}) between the 1980s and the early 2000s (figures 1(b) and S27), coinciding with a period of relatively strong monsoon intensity (figure 1(c)). Since 2005 the monsoon has arrived later and withdrawn sooner, shortening its total duration and becoming weaker in its intensity (figures 1(c) and S27). All sites see an increase in total precipitation coinciding with this expansion of the monsoon duration (figures 2(c)–(h)), especially for Parlung 4, which also demonstrates a period of relatively cool temperatures and increased cloudiness during the early 2000s, interrupting the overall warming trend (figure 2(d)). The entire HMA reveals a

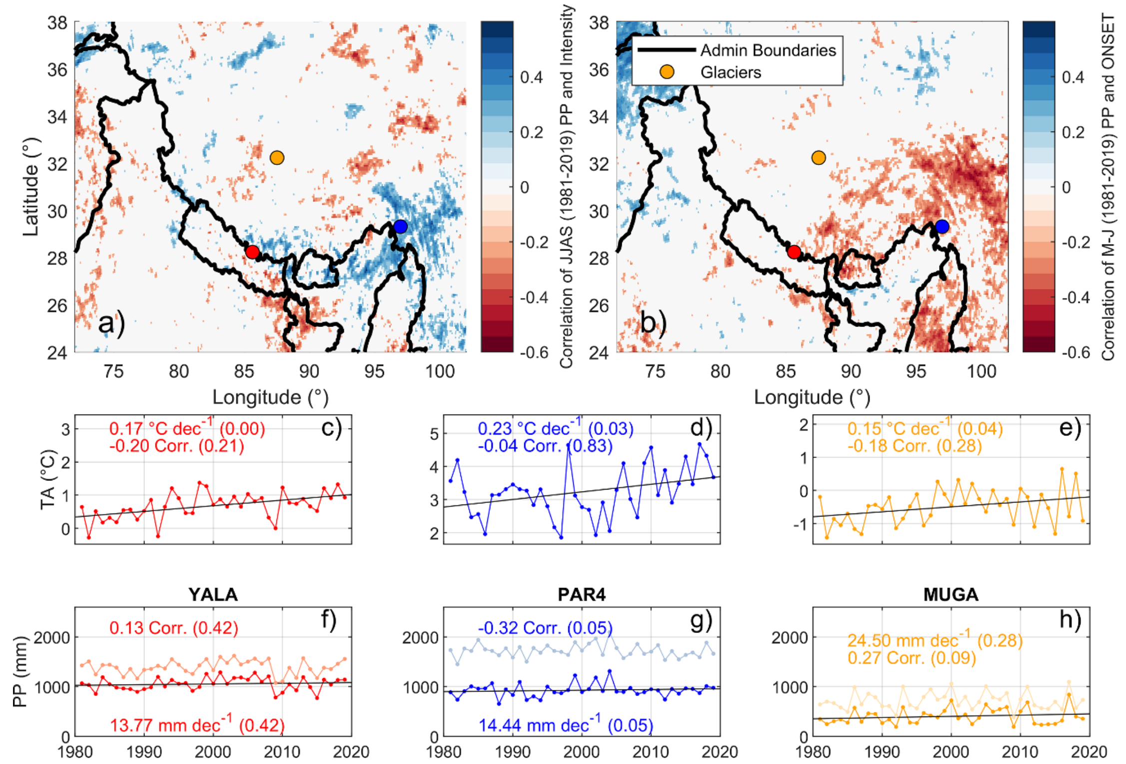

Figure 2. JJAS precipitation (PP) correlation to monsoon intensity (a) and May–June precipitation correlation to onset timing (b) across HMA (1981–2019), whereby positive correlations in (b) indicate increased precipitation for a later monsoon. Correlations (detrended) not significant to the 0.95 level are shown in white. Trends in mean JJAS TA (c)–(e) and total JJAS PP (f)–(h) are given for YALA (c), (f), PAR4 (d), (g) and MUGA (e), (h). Faded lines for (f)–(h) indicate the annual precipitation sum. Annotations also show the correlations of May–June TA and PP with the monsoon onset timing (level of significance (p-value) given in parentheses). Scales for (f)–(h) are equal.

significant warming trend over the past four decades (figure S28), though with markedly different patterns at the study sites: summer (JJAS) temperatures at Yala continue almost unabated at a rate of 0.17 °C dec^{-1}; the stronger warming at Parlung 4 (0.23 °C dec^{-1}) combines a period of relative cooling and no clear trend pre-2000s, with a much stronger warming pattern since 2005, and; Mugagangqiong demonstrates a coincident increase in mean annual air temperature and precipitation during the early millennium (figure 2(e)).

A higher intensity monsoon produces increased total precipitation for Parlung 4 and Yala, but has no significant correlation with precipitation at Mugagangqiong (figure 2(a)). An early monsoon arrival relates to increased precipitation (negative correlation) for much of southeastern and south central Tibet during May–June (figures 2(b) and S48), but shows no clear correlation for the Nepalese Himalaya (figures 2(b) and (f)). The increase in monsoon duration is governed by a tendency towards later cessation (figure S27) and has a more notable influence on summer temperature for the eastern Tibetan Plateau, though with few statistically significant correlations (figure S36). The patterns of radiative fluxes, cloudiness and humidity equally show few statistically significant trends across HMA for the full 40 year period (figures S28–S34), though at the glacier sites, the inter-decadal and long-term patterns suggest an increasing cloudiness and humidity alongside reduced shortwave radiation (figure S35).

3.2. Long-term glacier response to climate

The long term glacier mass balance of Mugagangqiong is highly distinct to the lower elevation, southerly sites (figure 3(a)) with a near-neutral, negative mass balance that has changed little since the 1980s. This is characteristic of its low temperatures, dry environment and low mass turnover rates (figure S44). Yala and Parlung 4, meanwhile, exhibit a much larger total mass loss over the past 40 years, despite significant differences in their inter-annual and inter-decadal mass balances (figure 3(a)). The mass balances of Yala and Parlung 4 closely reflect the inter-annual variability of air temperature and total precipitation (figure 2). Yala, however, experiences an almost continuous mass loss since 1980 with few positive mass balance years (figure 3(c)). Conversely, the mass loss at Parlung 4 is a combination of largely negative mass balance years interspersed by extended periods of positive or near-neutral mass balance (figure 3(d)) resulting in more mass loss during the drier 1980s (mean of -0.35 ± 0.11 m w.e. a^{-1} compared to -0.24 ± 0.20 m w.e. a^{-1} of Yala) followed by minimal mass loss from 2000 to 2005 (mean of -0.03 ± 0.13 m w.e. a^{-1} compared to -0.28

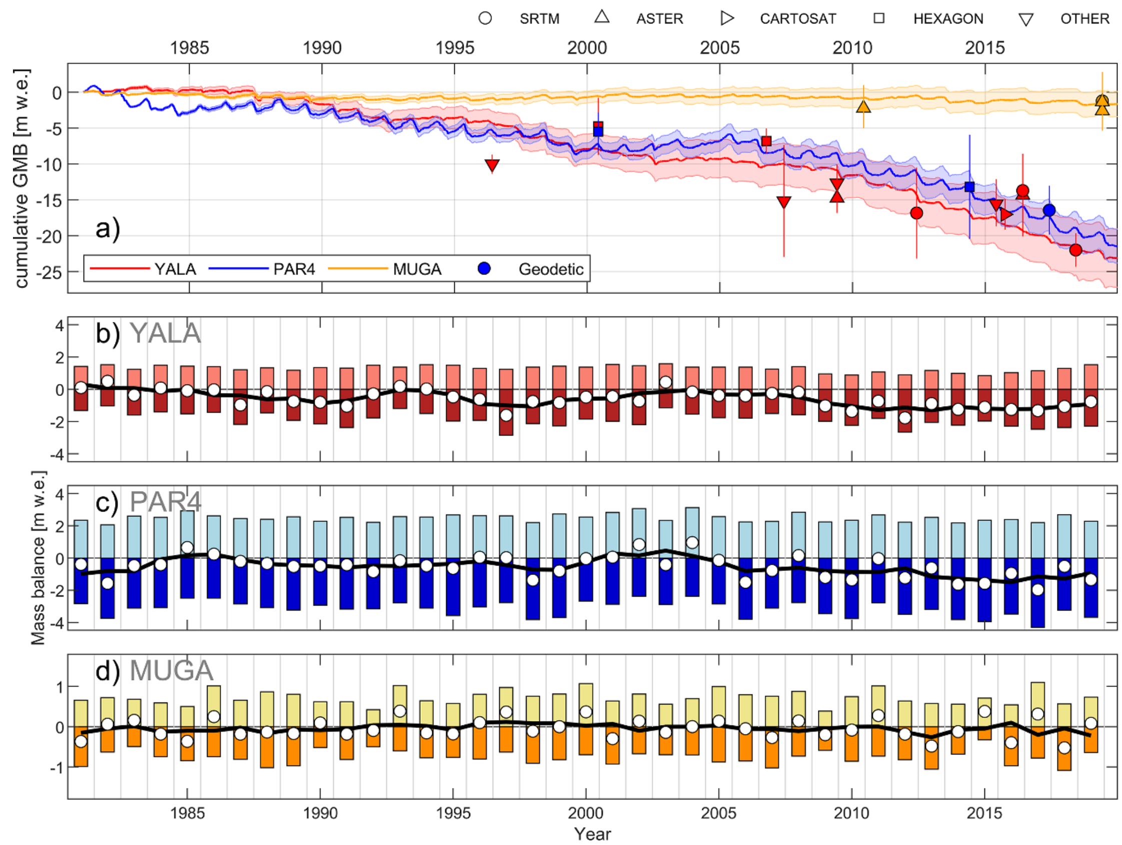

Figure 3. Modelled cumulative hourly (a) and annual specific (b)–(d) glacier mass balance for the three glacier study sites. Shaded areas in (a) indicate the Monte Carlo uncertainties derived from 1000 runs of varying forcing parameters. Panel (a) indicates the observed geodetic-derived mass balances (markers) from the literature (see supplementary material) with the observed uncertainties given as errorbars. Positive and negative bars for (c)–(e) indicate the cumulative positive and negative balances for each calendar year.

$\pm$ 0.17 m w.e. a^{-1} of Yala) and finally a period of more rapid mass loss continuing until 2019 (-1.00 $\pm$ 0.12 m w.e. a^{-1} vs. -1.01 ± 0.19 m w.e. a^{-1} at Yala). Patterns of mass balance at Mugagangqiong indicate no extended periods of negative or positive mass balance, but rather year to year fluctuations between weak positive and negative mass balances (figure 3(e)). On average, modelled glacier mass balances were -0.59 ± 0.20, -0.55 ± 0.12 and -0.04 ± 0.09 m w.e. a^{-1} for Yala, Parlung 4 and Mugagangqiong, respectively.

3.3. Key drivers of distinct glacier mass loss

A key driver of the energy budget at all sites is the pre-monsoon and monsoon snowfall (figures 4 and S43), which dictates the increases in early monsoon albedo and reduction in net shortwave radiation (figure S47). While all sites behave similarly in this regard, the mass balance of Mugagangqiong shows a stronger correlation to both pre-monsoon and monsoon snowfall (figure S43), as its low melt rates and notable sublimation (constituting 20% of total ablation vs 8% at Yala and 3% at Parlung 4) are highly controlled by radiative fluxes under cold temperatures.

Figure 4 emphasises the distinct patterns of snowfall and precipitation phase during the pre-monsoon to monsoon transition in May–June. At Yala, an early monsoon onset coincides with earlier snowfall at the glacier, though the total amount of snowfall is larger (∼37 mm on average) when the monsoon arrives late (figure 4(a)), which appears to be strongly linked to the higher fraction of solid precipitation for those years (figure 4(a)). Despite this average increase in May–June snowfall to the glacier, a late monsoon onset does not significantly alter the mass balance of Yala for the remainder of the year (figure 4(b)).

At Parlung 4, a later monsoon produces slightly cooler average conditions (figure S47), delaying liquid precipitation events during May compared to an early onset year (figure 4(c)). However, because of the substantial decrease in precipitation (∼130 mm on average), a late monsoon onset can sizeably influence the summer mass balance of Parlung 4 (figure 4), because the onset timing itself can explain 32(27)% of the variability in pre-monsoon (monsoon) snowfall. Due to the reduced surface albedo (figure S47—which can explain up to 87% of glacier mass balance variability) and heightened net shortwave radiation, mass balances are almost 0.5 m w.e. more negative on average than early onset years (figures 4 and 5), despite that only a weak correlation (-0.18, $p = 0.2$) to the monsoon onset itself exists (figure S43). While a late

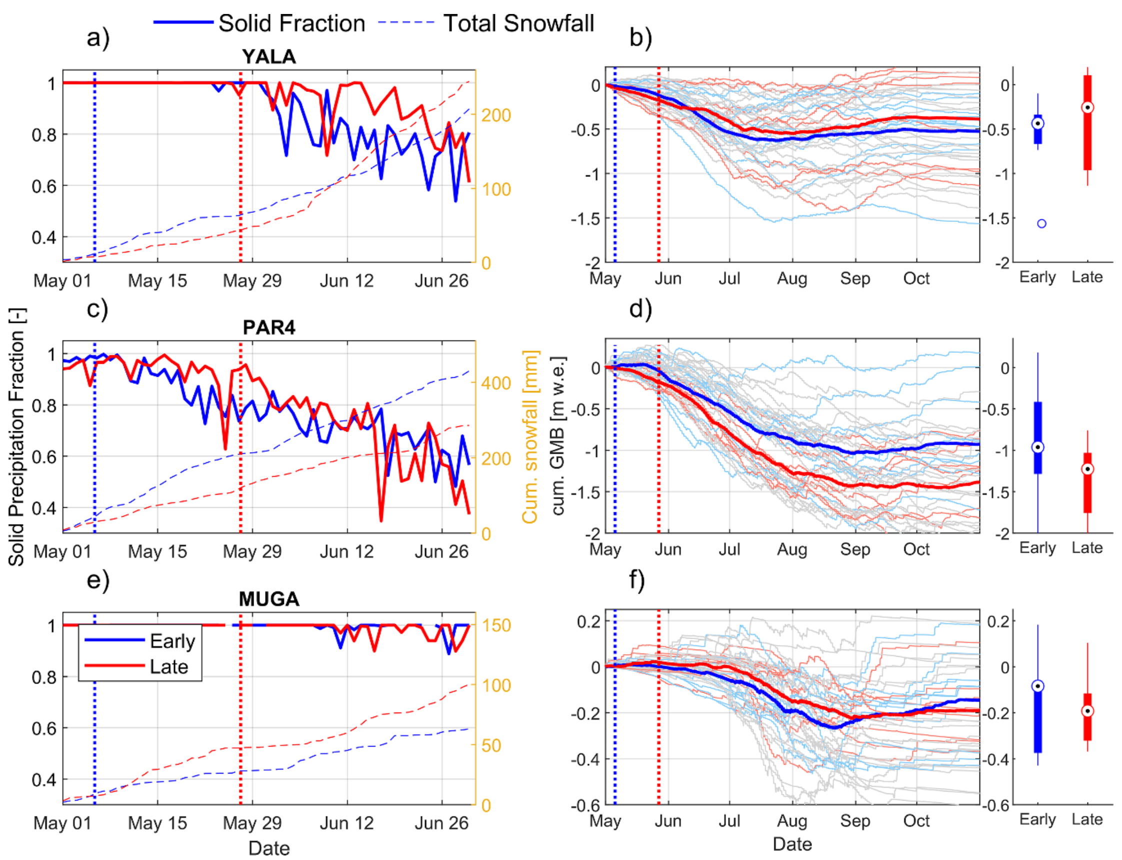

Figure 4. (a), (c), (e) Precipitation phase (solid lines) and cumulative snowfall (dashed lines) during the May–June transition from pre-monsoon to monsoon conditions. Data are presented for the mean of early (blue) and late (red) onset years for YALA (a), (b), PAR4 (c), (d) and MUGA (e), (f). (b), (d), (f) shows the cumulative glacier mass balance since May 1st, where thin lines represent individual years, coloured by the monsoon onset classification and thick lines represent the average conditions for early and late monsoon onset. Vertical dashed lines indicate the mean dates for early (blue) and late (red) onset years. Boxplots to the right indicate the end-of-year mass balances given the early or late monsoon onset.

monsoon onset produces a consistent mass balance response for Parlung 4, early onset years result in a wide range of potential mass balances for the summer months (figure 4(d)). The summer and annual glacier mass balances are, however, significantly distinct between early and late onset years ($p = 0.05$, figure 4(d) boxplots).

Interestingly, for years where the monsoon arrived late, May–June precipitation at Mugagangqiong was augmented (40 mm (58%) increase—figure 4(e)), suggesting a stronger role of westerly storm events in the absence of the monsoon precipitation (figure 1(a)—correlation = 0.27, $p = 0.1$). Given its elevation, however, no notable differences in precipitation phase are apparent for Mugagangqiong during this transition period (figure 4(e)). Average differences in cumulative mass balance are only apparent until late August, however, and are typically ∼0.04 m w.e. Variability in onset timing produces negligible correlations (−0.15) with the amount total monsoon snowfall at this site. As later monsoon onset years were typical for the cooler period of the simulation (figure S40), we also tested early vs late monsoon years only for the pre-2000s period and found a consistent pattern of May–June precipitation amount and phase for all glaciers as described above (figure S45).

Annual mass balances of Parlung 4 are generally affected less by the monsoon cessation date (figure 5). The mass balances of Yala and Mugagangiong are, however, more responsive to the cessation timing of the monsoon, but for different reasons: a later cessation at Yala relates to prolonged warmer air temperatures (figure S48(a)) which drives more melting and more negative mass balances; for Mugagangqiong, a later cessation date provides a longer period with precipitation (up to 200 mm on average compared to early cessation years—figure S48(f)), and thus produces a more positive mass balance. However, a more positive post-monsoon mass balance at Mugagangqiong does not significantly impact to the spring mass balance in the following year (not shown).

Monsoon duration itself balances many of the aforementioned processes to reveal no clear relationship to annual or summer mass balance (figure 5). The years with the weakest monsoon intensity, however, coincide with recent, warmer conditions (Yao *et al* 2022), producing a consistently more negative mass balance at all sites: up to 1 m w.e. more mass

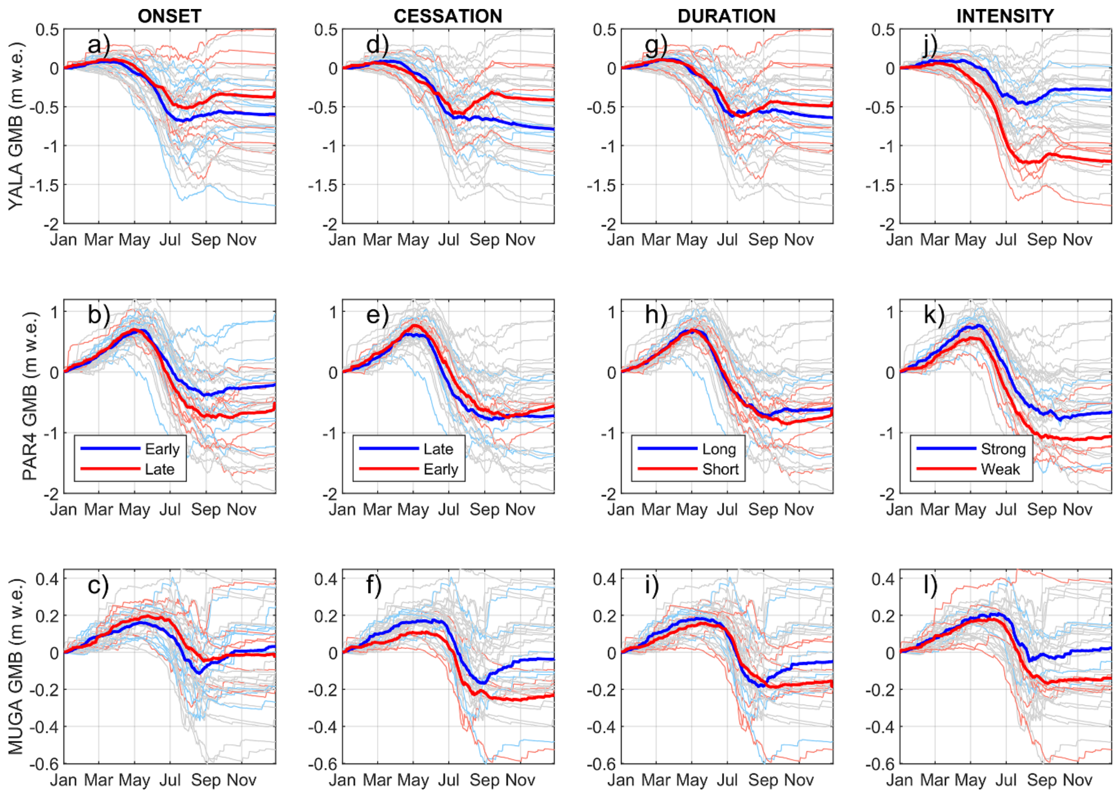

Figure 5. The relationship of cumulative annual mass balance and monsoon onset (a)–(c), cessation (d)–(f), duration (g)–(i) and intensity (j)–(l) for YALA (a), (d), (g), (j), PAR4 (b), (e), (h), (k) and MUGA (c), (f), (i), (l). Thicker lines indicate the mean of each condition highlighted by the legend. Note: cessation colours are the inverse of that for monsoon onset.

loss on average at Yala; 0.45 m w.e. greater mass loss at Parlung 4 and; 0.13 m w.e. more mass loss at Mugagangqiong relative to strong monsoon intensity years. Controlling for the effect of increasing air temperatures in recent years, the monsoon intensity is able to explain ∼50% of the variability in Yala summer mass balance (partial correlation $r = 0.498$, $p = 0.001$), but only 15% for Parlung 4 and <3% at for Mugagangqiong.

Monsoon characteristics (i.e. onset timing) can be associated with variable responses in glacier mass balance at our study sites, but the variability in meteorological conditions during the summer, which are only be partly influenced by the monsoon itself (up to 20% variability in (pre-)monsoon precipitation explained by monsoon timing or intensity—figure S43), play a dominant role in determining surface conditions and resultant mass loss. Figure 6 indicates that air temperature is the strongest control on glacier mass balance for Parlung 4, largely through its impact on the phase of monsoon precipitation (Jouberton *et al* 2022—figures 6(k)and S49(h)) and surface albedo (figure S49(k)—Zhu *et al* 2022). Controlling for the effect of air temperature itself, changes in the solid fraction of precipitation can explain 41% of the variability in glacier mass balance at Parlung 4. Meanwhile, precipitation phase changes had a smaller impact on Yala and Mugagangqiong, and mass balances were mostly responsive to the total amount of monsoon precipitation (figures 6, S49 and S50). Although the role of turbulent heat fluxes was more distinct between each site, increases in net shortwave radiation were consistently associated with the most negative mass balance years for all glaciers (figure S50).

4. Discussion

Earlier studies have emphasised the stark differences in the surface energy balance of different glaciers in HMA (Zhu *et al* 2015, 2018, Fugger *et al* 2022), and the relationship of glacier energy balance with the monsoon (Mölg *et al* 2012, Li *et al* 2018, Fugger *et al* 2022). However, while these works have demonstrated a detailed response of glaciers to prevailing conditions for a number of individual years, few studies, to the authors' knowledge, have provided a long-term perspective on glacier energy/mass balance and monsoon characteristics (Arndt *et al* 2021). Our results reveal a long-term pattern of glacier mass loss (figure 3) Shaw *et al* (2022) consistent with warming trends present in the WRF simulations (figure S28) and ground based climatologies (Ren *et al* 2017, de Kok *et al* 2020) (figure S5). However, notable wet periods during the early 2000s are superimposed on this long-term pattern of decline and have contrasting consequences for the mass balance of our three study glaciers.

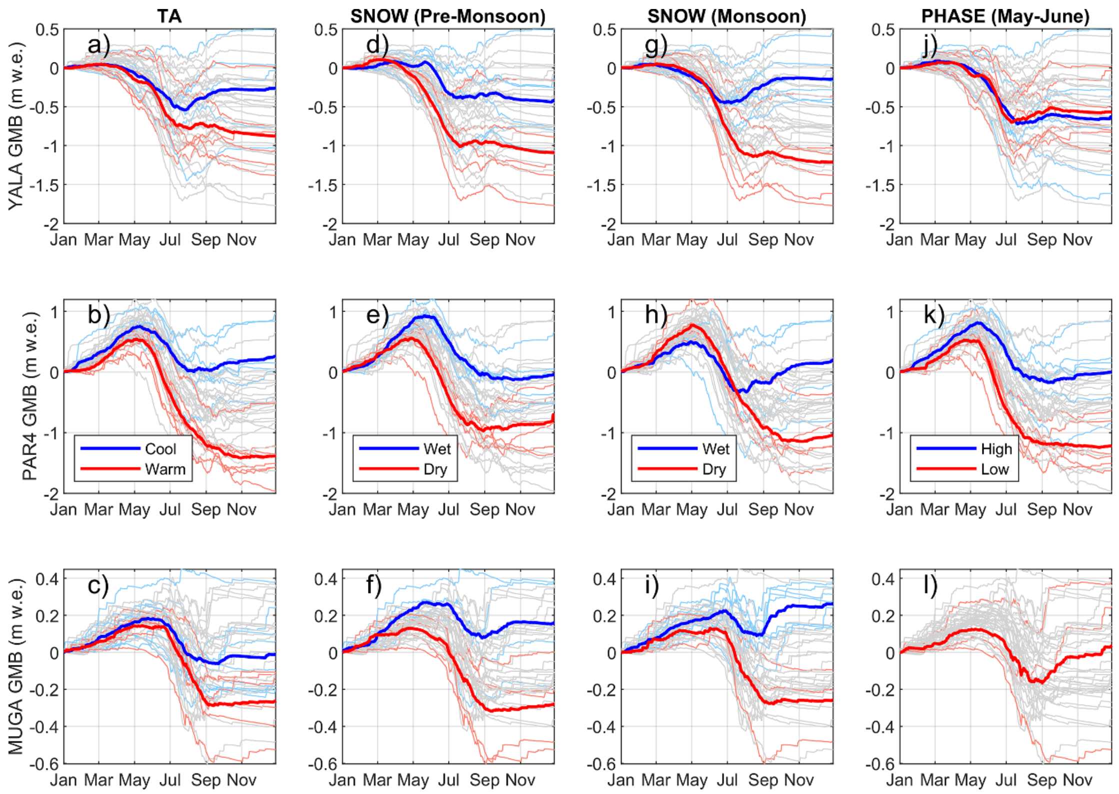

Figure 6. As figure 5, but mapping cumulative annual glacier mass balance of Yala (top), Parlung 4 (middle) and Mugagangqiong (bottom) against anomalously cool (blue) and warm (red) conditions (a)–(c), anomalously wet (blue) or dry (red) pre-monsoon (d)–(f) and monsoon (g)–(i) snowfall and anomalously high (blue) and low (red) solid precipitation fraction (phase) (j)–(l). Anomalies are given as those years above or below 1 standard deviation from the mean of all years. Thicker lines indicate the mean of each condition highlighted by the legend. No anomalously high solid precipitation fraction (phase) years are evident at Mugagangqiong (average is near 1) so no blue line is given.

Because of the larger elevation range of Parlung 4 in the southeastern Tibetan Plateau (table 1), its mass balance sensitivity is more strongly determined by the combination of pre-monsoon snowfall amounts (figure 4(c)) and precipitation phase during the monsoon (Zhu *et al* 2018, Jouberton *et al* 2022), particularly at elevations near the inter-annual ELA (5200 m a.s.l.), which are more responsive to a late arrival of the monsoon (figure S44). Evidence during the May–June period (figure 4) suggests that the large decreases in total precipitation received during these anomalously late monsoon years (figure 1(b)) were sufficient to overcome the relatively higher fractions of solid precipitation during the cooler pre-monsoon conditions at Parlung 4 and can dictate the mass balance of the entire summer (figures 4 and 5). This suggests that the tendency towards a later monsoon onset (figure S35), combined with the increasing liquid precipitation events during the summer (Jouberton *et al* 2022), could further exacerbate glacier health in the southeastern Tibetan Plateau.

In contrast to this, the small Nepalese glacier (Yala) was much less sensitive to the wetter conditions at the start of the Millennium, resulting in a more continuous mass loss (figure 3), consistent with modelled long term mass balances in northwestern Nepal (Arndt *et al* 2021). Although the size of the glacier and its limited accumulation area (Stumm *et al* 2021, Sunako *et al* 2020) may have dictated its reduced sensitivity to the expansion of the monsoon period, an early monsoon actually produces less snowfall during the monsoon transition period (May–June) at this glacier, despite shifting the occurrence of snow sooner. A weakening monsoon intensity and drier conditions, coinciding with warmer air temperatures of recent decades (figure 2) can explain half of the mass balance variability at this glacier, but the amount of snowfall during late June is also of great importance (figure 6).

Because of its relatively high elevation, cold temperatures and arid conditions characteristic of our central Tibetan glacier (Mugagangqiong), long term changes, while evidently negative over the course of four decades (figure 3), are ∼14 times less negative than Yala. Because of its location on the border of the monsoon dominated region (figure 1(a)), a late monsoon arrival actually results in a greater May–June precipitation, perhaps due to an increasing incidence of westerly storm fronts. This re-emphasises the potential importance of westerly circulation patterns for glacier accumulation regimes on the Tibetan Plateau, as shown by Mölg *et al* (2014) and Li *et al* (2018), and might explain the correlation of increased active monsoon periods with more negative glacier mass balance at Mugagangqiong (figure S43). However, this finding contrasts somewhat with those aforementioned studies in which an earlier and stronger monsoon onset resulted in higher accumulation patterns for Zhadang and Qiangtang No.1 glaciers. This might be explained in part by the location of those glaciers further east within the inner Tibetan Plateau, whereby westerly intrusions are weakened and result in a less dominant source of pre-monsoon snowfall, but also may relate to the different methodological approaches, datasets and time-frame of this current work. An early retreat of monsoon conditions, especially in the absence of westerly disturbances during late summer, produces a more negative post-monsoon mass balance at Mugagangqiong (figure 5), due to the large reduction of precipitation and the limited westerly activity during those months.

Ultimately, our results indicate that warmer atmospheric conditions, which coincide with a weakening of the summer monsoon (figure 1(c)), are the main driver of continued mass loss at glaciers across HMA (principally through increased net shortwave radiation (figure S50)) and are comparable to the patterns of glacier sensitivity suggested by Sakai and Fujita (2017). While a late monsoon arrival and reduced snowfall can dictate much of the mass loss for Parlung 4 Glacier (figures 4(c) and 5(b)), the annual mass balance of summer-accumulation glaciers (Yala and Mugagangqiong) are less controlled by the timing of monsoon. Rather, for those sites, the intensity of the core monsoon season and its impact on (i) the total amount of snowfall and (ii) its interaction with westerly storm events (Mugagangqiong) have greater impact (figures 4 and 6). This highlights the non-uniform response of glaciers in HMA to the monsoon and the need for a greater focus on sub-regional monsoon intensity and its interaction with westerly storms and general warming trends of the last half century.

In general, high elevation, long-term measurements are still too scarce to piece together a full picture of the monsoon's influence on glacier mass balance across all HMA, and even then, uncertainty surrounding the elevation gradients of precipitation may still hamper our ability to identify clear signals relating it to regional climatic drivers. Of particular benefit would be the inclusion of rare meteorological and mass balance datasets in understudied regions of the western Kunlun Mountains and western-central Tibetan Plateau (e.g. Zhu et al 2018, 2022, Yang et al 2022) that would help clarify the spatial limits of the monsoon's influence beyond our three selected sites. The inclusion of debris-covered glaciers would additionally benefit the understanding of glacier response to the monsoon across HMA (Fugger et al 2022), though those glaciers are currently subject to greater uncertainties with respect to spatial variability in debris cover thickness and properties that evolve over multi-decadal time scales.

Here we were able to generate longer term insights into the variable changes of glaciers in different climatic sub-regions of HMA which cannot be revealed by diverse and discontinuous, geodetic observations alone (figures 3(a) and S20, Bhattacharya et al 2021, Hugonnet et al 2021). Nevertheless, our forcing data are still subject to uncertainties that stem from parameter choices (table S1) and its coarse spatial resolution (9 km) which may mis-represent the dynamical processes governing the timing and magnitude of precipitation at very local scales (e.g. Bonekamp et al 2018). Further still, our long term analysis is made computationally feasible by the adoption of a physically-based, but semi-distributed modelling framework. Though we have confidence in the robustness of the approach to derive glacier-wide mass balances, there are likely feedbacks due to local topography and ice-atmosphere interactions as glaciers shrink (Florentine et al 2018, Shaw et al 2021) that we cannot represent with the adopted methodology in this study. Advancements in kilometre/sub-kilometre resolution atmospheric models (Collier and Immerzeel 2015, Bonekamp et al 2018, Zhou et al 2021) and the increasing availability of high elevation meteorological networks in high mountain, glacierised regions (e.g. Zhu et al 2018, Yang et al 2022) should continue to improve our ability to represent local glacier responses to regional scale monsoon dynamics moving forward.

5. Conclusions

We apply a multi-decadal (1980–2019) land surface model, driven by hourly bias-corrected WRF outputs to simulate the changing mass balance of three distinct glaciers in HMA and their relation to the summer monsoon. Our results demonstrate a differing response of glacier energy and mass balance to the patterns of the monsoon at the three sites, governed principally by the surface albedo and affected by the role of pre-monsoon/early monsoon snowfall amount and phase and by the intensity of the monsoon period. While all three glaciers have experienced long-term mass losses (ranging from -0.04 ± 0.09 to -0.59 ± 0.20 m w.e. a^{-1}) in line with widespread warming across the region, inter-decadal variability in the timing and strength of the monsoon precipitation has strongly modulated the glacier surface conditions at the site in the southeastern Tibetan Plateau. This is largely in line with the notable increases of early 2000s precipitation due to the expansion of the monsoon duration. Considering the critical May–June transition period, we highlight that a late monsoon arrival generates significantly less total snowfall for the glacier ($\sim$130 mm on average) in the southeastern Tibetan Plateau, producing consistently more negative mass balances (-0.5 m w.e. on average compared to early onset years).

Conversely, the arrival of the monsoon has less impact on the annual mass balance of the Himalayan glacier, which is more sensitive to the temperature and snowfall amount of the core monsoon season and its cessation. For the arid central Tibetan Plateau, a later arrival of the monsoon results more positive mass balances, likely due to the greater role of westerly storm events in providing early summer snowfall. The monsoon cessation determines a greater variability in post-monsoon energy balance at this site, however, due to the amount of monsoon precipitation in the absence of post-monsoon westerlies. Nevertheless, we found that the monsoon timing is less important than the overall intensity of monsoon conditions for the mass balance of summer-accumulation glaciers in the Nepalese Himalaya and central Tibet. Our findings elaborate on the complexity of glacier response to the diverse sub-climates in the region and we suggest the need for more high elevation observations combined with highly resolved atmospheric model simulations and long-term, fully distributed energy/mass balance studies.

Data availability statement

9 km WRF simulations are publicly available at: http://biggeo.gvc.gu.se/TPReanalysis/. Data for the Langtang catchment are publicly hosted by the ICIMOD RDS at: http://rds.icimod.org/.

Reconstructed WRF time-series data at each glacier site and key model outputs are hosted at the following repository: https://doi.org/10.5281/zenodo.6418550.

The source code of the T&C model is available at https://doi.org/10.24433/CO.0905087.v2.

The data that support the findings of this study are openly available at the following URL/DOI: https://doi.org/10.5281/zenodo.6418550.

Acknowledgments

This work was supported by the SNF Sino-Swiss Science and Technology Cooperation (SSSTC) Project (IZLCZ0_189890) 'Understanding snow, glacier and rivers response to climate in High Mountain Asia (ASCENT)' and by JSPS and SNSF under the Joint Research Projects (JRPs: 20191503) scheme. The National Natural Science Foundation of China (41961134035) financially supported the data collection on Mugagangqiong and Parlung No. 4 glaciers. D Chen is supported by the Swedish Research Council (VR: 2019-03954). The computations of the 9 km WRF were enabled by resources provided by the Swedish National Infrastructure for Computing (SNIC) at the National Supercomputer Centre in Sweden (NSC) partially funded by the Swedish Research Council through Grant Agreement No. 2018-05973. We acknowledge funding from the European Research Council (ERC) under the European Union's Horizon 2020 research and innovation program Grant Agreement No. 772751, RAVEN ('Rapid mass lossess of debris covered glaciers in High Mountain Asia'). We recognise the hard fieldwork efforts of Utrecht University, ETH and ICIMOD in providing data for the Langtang catchment. S Sunako is thanked for the provision of updated glacier DEMs and outlines for Yala Glacier. W Immerzeel, R de Kok and members of the WSL HIMAL group are thanked for their valuable discussions at early stages of this work. We thank the editor and two anonymous reviewers for their constructive comments that improved the quality of the manuscript.

Conflict of interest

The authors declare that there are no conflicts of interest in the submission of this work.

Ethics statement

The authors declare that there are no ethical issues arising from this work.

ORCID iDs

T E Shaw https://orcid.org/0000-0001-7640-6152
E S Miles https://orcid.org/0000-0001-5446-8571
D Chen https://orcid.org/0000-0003-0288-5618
A Jouberton https://orcid.org/0000-0001-8509-9350
M Kneib https://orcid.org/0000-0002-2420-0475
S Fugger https://orcid.org/0000-0002-6847-4099
T Ou https://orcid.org/0000-0002-6847-4099
H-W Lai https://orcid.org/0000-0003-3813-0276
K Fujita https://orcid.org/0000-0003-3753-4981
W Yang https://orcid.org/0000-0001-6290-2227
S Fatichi https://orcid.org/0000-0003-1361-6659
F Pellicciotti https://orcid.org/0000-0002-5554-8087

References

Arndt A, Scherer D and Schneider C 2021 *Atmosphere* **12** 1–29
Baral P, Kayastha R B, Immerzeel W W, Pradhananga N S, Bhattarai B C, Shahi S, Galos S, Springer C, Joshi S P and Mool P K 2014 *Ann. Glaciol.* **55** 9–14
Bhattacharya A, Bolch T, Mukherjee K, King O, Menounos B, Kapitsa V, Neckel N, Yang W and Yao T 2021 *Nat. Commun.* **12** 1–13
Bollasina M A, Ming Y and Ramaswamy V 2011 *Science* **334** 502–5
Bombardi R J, Moron V and Goodnight J S 2020 *Int. J. Climatol.* **40** 641–67
Bonekamp P N, Collier E and Immerzeel W 2018 *J. Hydrometeorol.* **19** 1565–81
Botter M, Zeeman M, Burlando P and Fatichi S 2021 *Biogeosciences* **18** 1917–39
Brunello C F, Andermann C, Marc O, Schneider K A, Comiti F, Achleitner S and Hovius N 2020 *Geophys. Res. Lett.* **47** e2020GL088420
Cannon A J 2018 *Clim. Dyn.* **50** 31–49
Collier E and Immerzeel W W 2015 *J. Geophys. Res.: Atmos.* **175** 238

de Kok R J, Kraaijenbrink P D A, Tuinenburg O A, Bonekamp P N J and Immerzeel W W 2020 *Cryosphere* **14** 3215–34

de Kok R J, Tuinenburg O A, Bonekamp P N and Immerzeel W W 2018 *Geophys. Res. Lett.* **45** 2047–54

Ding B, Yang K, Qin J, Wang L, Chen Y and He X 2014 *J. Hydrol.* **513** 154–63

Ding B, Yang K, Yang W, He X, Chen Y, Lazhu G X, Wang L, Wu H and Yao T 2017 *Water Resour. Res.* **53** 3146–78

Faghih M, Brissette F and Sabeti P 2021 *Hydrol. Earth Syst. Sci. Discuss.* **26** 1545–63

Fatichi S, Ivanov V Y and Caporali E 2012 *J. Adv. Model. Earth Syst.* **4** M05003

Fatichi S, Peleg N, Mastrotheodoros T, Pappas C and Manoli G 2021 *Sci. Adv.* **7** 1–9

Feng X *et al* 2020 *J. Geophys. Res.: Atmos.* **125** 1–11

Florentine C, Harper J, Fagre D, Moore J and Peitzsch E 2018 *Cryosphere* **12** 2109–22

Forsythe N, Fowler H J, Li X F, Blenkinsop S and Pritchard D 2017 *Nat. Clim. Change* **7** 664–70

Fugger S *et al* 2022 *Cryosphere* **16** 1631–52

Fujita K, Takeuchi N and Seko K 1998 *Bull. Glacier Res.* **16** 75–81

Fyffe C L *et al* 2021 *J. Geophys. Res.: Atmos.* **126** 1–22

Ha K J, Kim B H, Chung E S, Chan J C and Chang C P 2020 *Environ. Res. Lett.* **15** 034055

Hugonnet R *et al* 2021 *Nature* **592** 726–31

Immerzeel W W *et al* 2020 *Nature* **577** 364–9

Jouberton A, Shaw T E, Miles E S, McCarthy M J, Fugger S, Ren S, Dehecq A, Yang W and Pellicciotti F 2022 *Proc. Natl Acad. Sci.* **119** e2109796119

Li S, Yao T, Yang W, Yu W and Zhu M 2018 *J. Geophys. Res.: Atmos.* **123** 6390–409

Litt M, Shea J, Wagnon P, Steiner J, Koch I, Stigter E and Immerzeel W 2019 *Sci. Rep.* **9** 1–13

Mastrotheodoros T *et al* 2020 *Nat. Clim. Change* **10** 155–61

Maussion F, Scherer D, Mölg T, Collier E, Curio J and Finkelnburg R 2014 *J. Clim.* **27** 1910–27

Meyer J, Kohn I, Stahl K, Hakala K, Seibert J and Cannon A J 2019 *Hydrol. Earth Syst. Sci.* **23** 1339–54

Miles E, McCarthy M, Dehecq A, Kneib M, Fugger S and Pellicciotti F 2021 *Nat. Commun.* **12** 2868

Mölg T, Maussion F and Scherer D 2014 *Nat. Clim. Change* **4** 68–73

Mölg T, Maussion F, Yang W and Scherer D 2012 *Cryosphere* **6** 1445–61

Ou T, Chen D, Chen X, Lin C, Yang K, Lai H W and Zhang F 2020 *Clim. Dyn.* **54** 3525–39

Prasad V S and Hayashi T 2005 *Geophys. Res. Lett.* **32** 1–5

Pritchard H D, Kush H, Alai P and Shan K 2017 *Nature* **545** 169–74

Ren Y Y, Ren G Y, Sun X B, Shrestha A B, You Q L, Zhan Y J, Rajbhandari R, Zhang P F and Wen K M 2017 *Adv. Clim. Change Res.* **8** 148–56

Saha A and Ghosh S 2019 *Environ. Res. Commun.* **1** 061006

Sakai A and Fujita K 2017 *Sci. Rep.* **7** 1–8

Shaw T, Yang W, Ayala A, Bravo C, Zhao C and Pellicciotti F 2021 *Cryosphere* **15** 595–614

Shaw T E *et al* 2022 Reconstructed, long-term meteorological forcing and mass balance over glaciers in High Mountain Asia [Data set] *Zenodo* (available at: https://doi.org/10.5281/zenodo.6418550)

Steiner J F, Gurung T R, Joshi S P, Koch I, Saloranta T, Shea J, Shrestha A B, Stigter E and Immerzeel W W 2021 *Res. Observartory Catchments* **35** 1–7

Stigter E E, Litt M, Steiner J F and Bonekamp P N J 2018 *Front. Earth Sci.* **6** 1–16

Stumm D, Joshi S P, Gurung T R and Silwal G 2021 *Earth Syst. Sci. Data Discuss.* **13** 3791–818

Sun H, Su F, He Z, Ou T, Chen D, Li Z and Li Y 2021 *J. Hydrometeorol.* **22** 2055–71

Sunako S, Fujita K, Izumi T, Zamaguchi S, Sakai A and Kayastha R 2020 *J. Glaciol.* 3–29

Veh G, Korup O and Walz A 2020 *Proc. Natl Acad. Sci. USA* **117** 907–12

Viviroli D, Kummu M, Meybeck M, Kallio M and Wada Y 2020 *Nat. Sustain.* **3** 917–28

Yang W, Guo X, Yao T, Yang K, Zhao L, Li S and Zhu M 2011 *J. Geophys. Res. Atmos.* **116** 1–11

Yang W, Zhao C, Westoby M, Yao T, Wang Y, Pellicciotti F, Zhou J, He Z and Miles E 2020 *Remote Sens.* **12** 2389

Yang W, Zhu M, Guo X and Zhao H 2022 *J. Appl. Meteorol. Climatol.* **61** 1–35

Yao T *et al* 2012 *Nat. Clim. Change* **2** 663–7

Yao T *et al* 2022 *Nat. Rev. Earth Environ.* (https://doi.org/10.1038/s43017-022-00299-4)

Zemp M *et al* 2019 *Nature* **568** 382–6

Zhang W, Zhou T and Zhang L 2017 *J. Geophys. Res.* **122** 5808–22

Zhou X, Yang K, Ouyang L, Wang Y, Jiang Y, Li X, Chen D and Prein A 2021 *Clim. Dyn.* **57** 1673–87

Zhu M, Yao T, Thompson L G, Wang S, Yang W and Zhao H 2022 *Clim. Dyn.* (https://doi.org/10.1007/s00382-022-06283-4)

Zhu M, Yao T, Yang W, Maussion F, Huintjes E and Li S 2015 *J. Glaciol.* **61** 595–607

Zhu M, Yao T, Yang W, Wu G, Li S, Zhao H and Thompson L 2022 *J. Geophys. Res.: Atmos.* **84** 1511–8

Zhu M, Yao T, Yang W, Xu B, Wu G and Wang X 2018 *Clim. Dyn.* **50** 3457–84

Zhu Y, Sang Y F, Chen D, Sivakumar B and Li D 2020 *Environ. Res. Lett.* **15** 124067

Supplementary Information for:

Multi-Decadal Monsoon Characteristics and Glacier response in High Mountain Asia

CONTENTS:

S1 DATA

S1.1 Glacier sites and AWS details

Yala Glacier: An off-glacier AWS at Yala Basecamp (28.232°N, 85.612°E, 5090 m a.s.l. Fig. 1C) has been operated by Utrecht University/ICIMOD since 2012 (Steiner et al., 2021), logging hourly data for air temperature ('TA', °C), relative humidity ('RH', %), air pressure ('PR', mb), incoming and outgoing shortwave ('SWIN'/'SWOUT', Wm-2) and longwave ('LWIN'/'LWOUT', Wm-2) radiation, wind speed ('FF', m s-1) and precipitation ('PP', mm hr). Since 2016, an on-glacier AWS (Stigter et al., 2018) has been operational on Yala Glacier (28.234°N, 85.617°E, 5291 m a.s.l.), recording TA, RH, SWIN, SWOUT, LWIN, LWOUT, FF and snow depth ('SD', m). Additional 'MicroMet' stations provided TA, RH and FF data (Stigter et al., 2018; Steiner et a., 2021) in order to calibrate appropriate vertical gradients for distributing meteorological variables across the glacier (section S2.2). Approximately 16% of the data record for Yala Basecamp AWS since 2012 is missing, largely due to data gaps in 2015, following the Gorkha Nepal earthquake.

Parlung Number 4 Glacier: Off-glacier data are available from an AWS 4 km from the terminus of Parlung Number 4 Glacier ('PAR4'). The off-glacier AWS (29.314°N, 96.955°E, 4588 m a.s.l.) has been logging TA, RH, SWIN, LWIN, PR, FF and PP data uninterrupted since 2012. An on-glacier AWS has also operated on the glacier ablation zone (29.245°N, 96.927°E, 4800 m a.s.l.) since 2012, with sporadic measurements during earlier years (such as 2009, Ding et al., 2017). All variables except PP are provided by this AWS. An upper AWS during 2010 (5200 m a.s.l., Zhu et al., 2015) and ice core measurements during 2006

(5500 m a.s.l., Xu et al., 2009) also help to constrain appropriate vertical gradients of precipitation, following Jouberton et al. (2022).

Mugagangqiong Glacier: For Mugagangqiong Glacier (‘MUGA’), only an off-glacier AWS exists for the study period, though it is located very close to the glacier (32.231°N, 87.493°E, 5850 m a.s.l.) and considered to be partially affected by the glacier boundary layer. Accordingly, we consider that the AWS likely well represents the on-glacier diurnal temperature patterns (Shaw et al., 2021; Yang et al., 2022), high elevation precipitation and timing of snow disappearance, while remaining static and stable at an off-glacier location. The AWS has hourly data on TA, RH, SWIN, SWOUT, LWIN, LWOUT, FF, PP, PR and SD since 2015.

S1.2 Additional WRF data description

Table S1 provides additional details regarding the WRF simulations, assumptions and parameterisation schemes. Additional detail can be found in Ou et al. (2020).

Table 1: The summary information of the WRF parameterisation schemes and assumptions.

Model	The Weather Research and Forecasting (WRF) model v3.7.1
Domain of Model [N, S, W, E] (dd.dddd°)	~[5(N), 45(N), 70 (E), 120(E)] 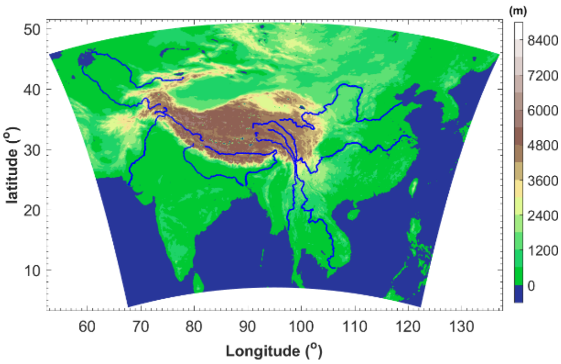
Spatial resolution (m)	9 km
Temporal resolution	Hourly
Period of simulation (dd.mm.yyyy – dd.mm.yyyy inclusive)	1979-2019
Input requirements	ERA5 (pressure and surface levels)
Vertical Levels	Vertical levels: 60 eta vertical levels with model top at 10 hPa
Constraints	(1) Lateral boundaries updated with ERA5. (2) Spectral nudging U/V wind, T,

	geopotential with ERA5; nudging coefficient: 0.0003; no nudging below level 5 (within the PBL)
Convection Scheme	None
Radiation Scheme	New goddard short-wave radiation scheme and RRTMG Long-wave radiation scheme
PBL Scheme	Yonsei University scheme (YSU)
Land Surface Scheme	Unified Noah Land Surface model
Microphysics Scheme	WRF double moment 6-class

S2) METHODOLOGY

S2.1) Multivariate bias-correction examples

As indicated in the main text, we utilise the multivariate bias-correction approach of Cannon (2018) (https://cran.r-project.org/web/packages/MBC/MBC.pdf) and we refer the reader to equations 5-7 of that article for full elaboration of the method. Here we demonstrate in Fig. S1-S3, examples of the multivariate bias correction applied to the WRF data for each glacier site. We assess the quality of the bias correction using standard metrics (mean absolute error - MAE and root mean square error - RMSE - Table S2) and confirm that the correlation between variables is preserved after correction (Wilcke et al., 2013). Moreover, we demonstrate that the trends of each variable are preserved post-bias-correction (Fig. S4) and that those trends are consistent with the nearest long-term climate station (Fig. S5) such that we retain confidence in the main drivers of glacier mass loss (Fig. 3).

In Fig. S6-S11 we demonstrate the re-constructed mean monthly air temperature and total precipitation series for each glacier, in comparison to the equivalent off-glacier AWS observations (black lines). While the multivariate bias-correction results in some offset for given months at given sites, we consider that the reconstruction of meteorological forcing from WRF is appropriate to address the scientific research questions.

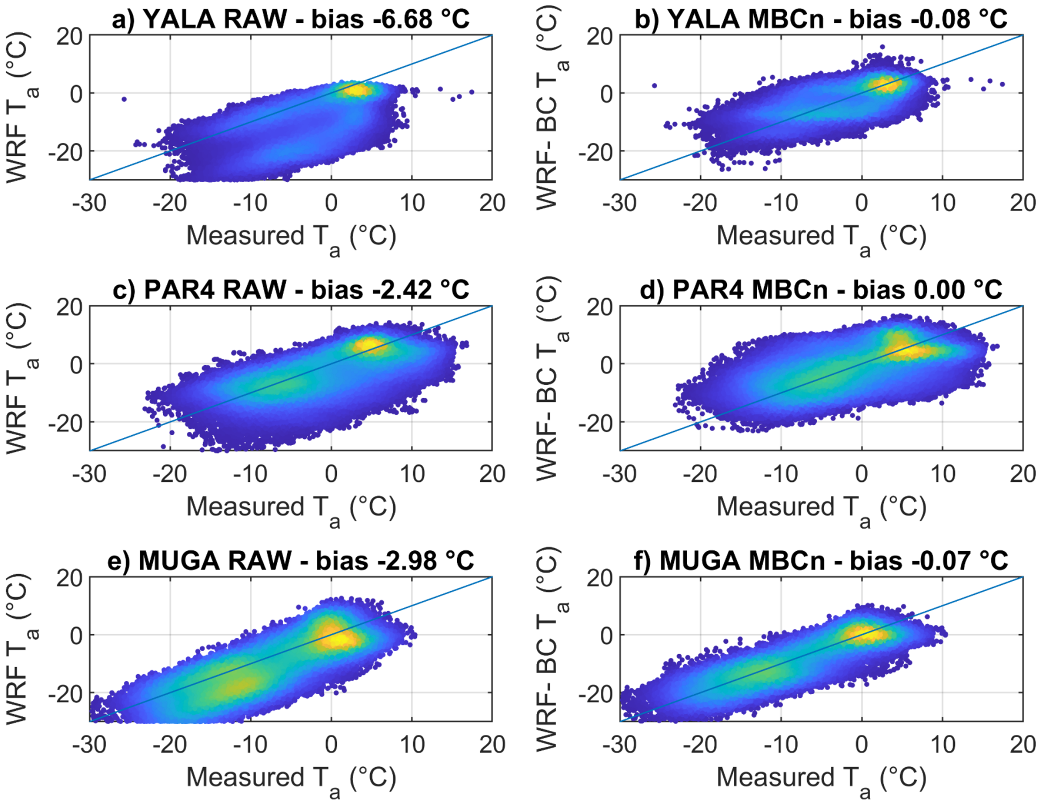

Fig. S1: The raw and bias-corrected air temperatures at each glacier given by a density scatter plot, whereby yellows and greens indicate the highest density of points.

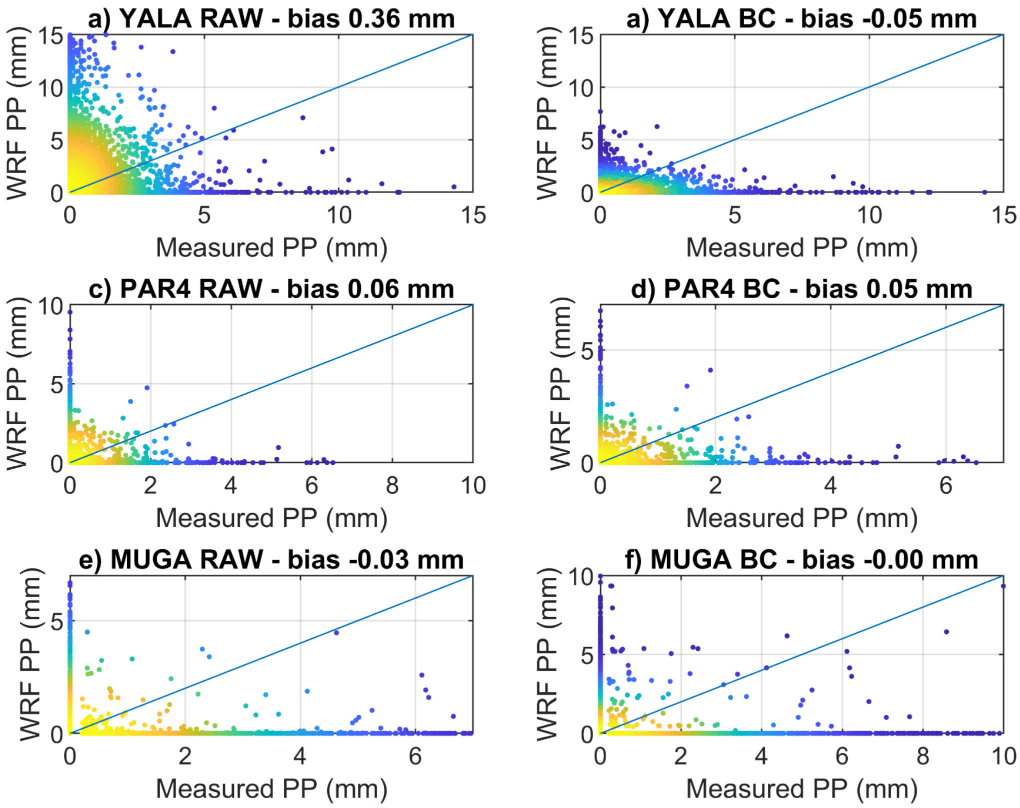

Fig. S2: As Fig. S1, but for precipitation (PP).

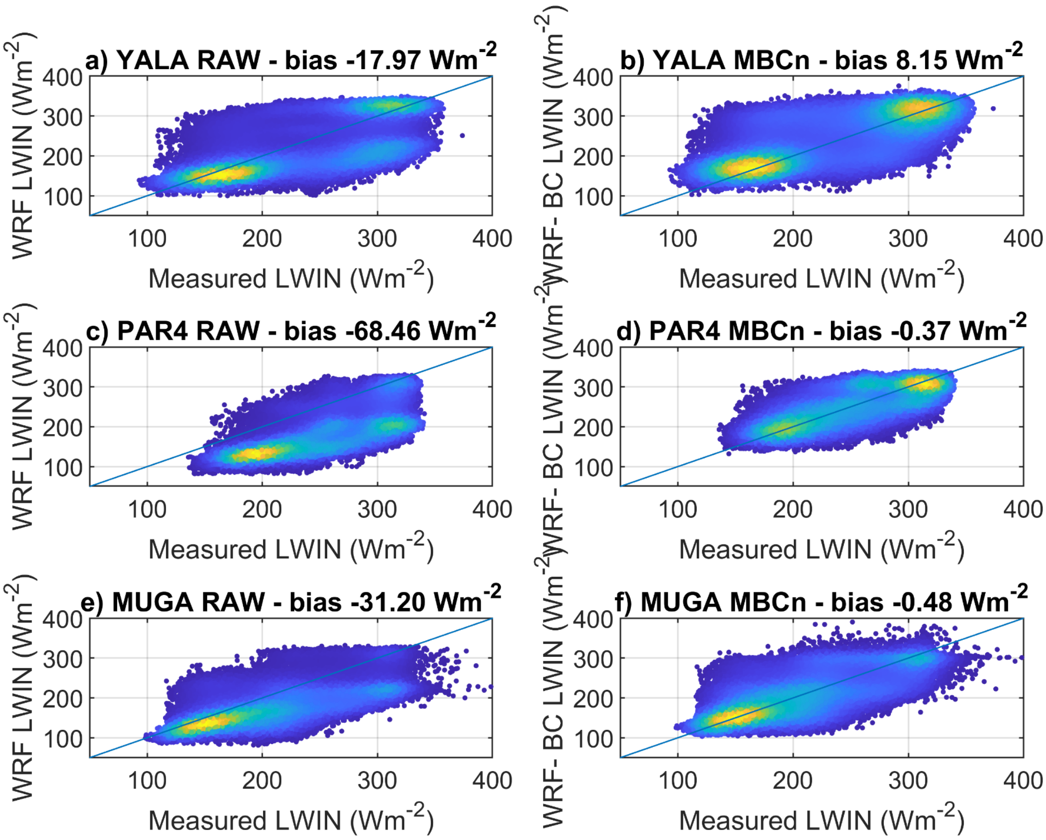

Fig. S3: As Fig. S1, but for incoming longwave radiation (LWIN).

Table S2: Summary statistics of the bias-correction for each glacier site. Biases, mean absolute error (MAE) and root mean squared error (RMSE) are present for the 'RAW' (un-corrected) and 'BC' (bias-corrected) data.

Variable	**Metric**	**YALA**		**PAR4**		**MUGA**	
		RAW / *BC*		RAW / *BC*		RAW / *BC*	
TA (°C)	**Bias**	**-6.67**	***-0.08***	**-2.41**	***0.004***	**-2.97**	***-0.07***
	MAE	7.53	*3.85*	5.32	*3.40*	5.43	*3.61*
	RMSE	9.55	*4.81*	6.80	*5.71*	6.63	*4.42*
PP (mm/ hr	**Bias**	**0.36**	***-0.05***	**0.05**	***0.04***	**-0.03**	***-0.003***
	MAE	0.56	*0.18*	0.22	*0.20*	0.09	*0.09*
	RMSE	1.90	*0.63*	0.73	*0.63*	0.64	*0.60*
RH (%)	**Bias**	**6.79**	***-4.9***	**-4.42**	***-0.37***	**-7.02**	***0.15***
	MAE	26.57	*27.25*	19.94	*21.00*	23.60	*20.90*
	RMSE	37.46	*39.20*	25.33	*26.00*	29.80	*26.80*
SWIN (Wm^{-2})	**Bias**	**43.50**	***10.70***	**98.66**	***-1.53***	**113.03**	***-1.48***
	MAE	364.5	*342.7*	433.6	*355.1*	419.9	*321.3*
	RMSE	509.6	*490.6*	567.3	*473.9*	543.1	*413.5*
LWIN (Wm^{-2})	**Bias**	**-17.90**	***8.14***	**-68.45**	***-0.37***	**-31.20**	***-0.48***
	MAE	42.40	*37.10*	71.02	*27.81*	42.02	*33.06*
	RMSE	56.20	*50.11*	79.60	*35.10*	52.83	*43.50*
FF ($m\ s^{-1}$)	**Bias**	**2.36**	***-0.06***	**2.13**	***-0.59***	**2.27**	***-0.002***
	MAE	2.86	*1.50*	3.55	*2.51*	2.93	*1.80*
	RMSE	3.84	*2.08*	4.57	*3.12*	3.75	*2.25*

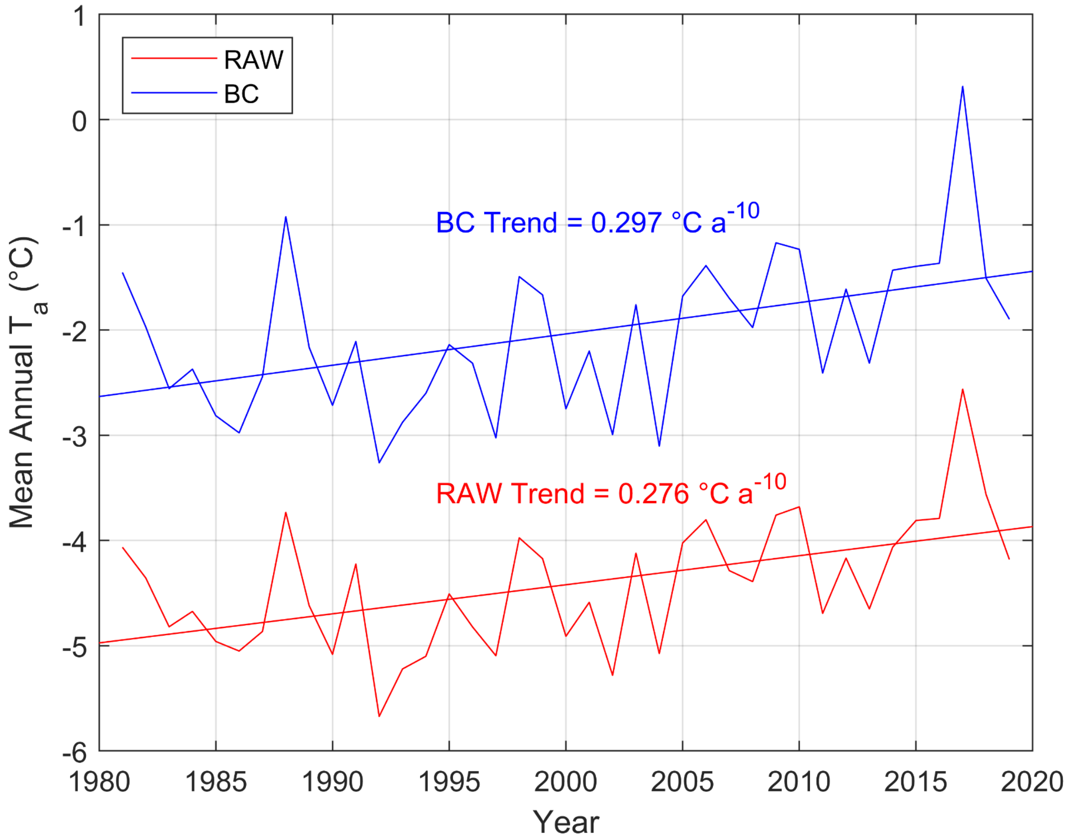

Fig. S4: The trends in mean annual air temperature at PAR4 to exemplify the general trend preservation of the data series after bias-correction. NOTE: trends of PAR4 air temperature are different to those in Fig. 2d, as they represent annual trends, not for the monsoon period only.

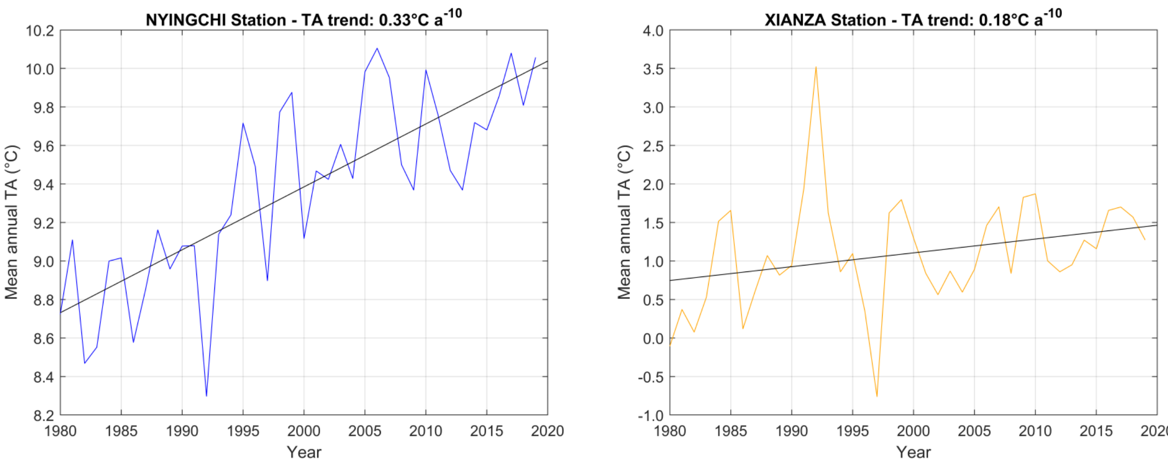

Fig. S5: The trends in annual mean air temperature for long-term regional climate stations for PAR4 (left - cf Fig. S3) and MUGA (right). Comparison with Fig. S35. Station data is taken from the Global Summary of the day (GSOD) available at:
https://www.ncei.noaa.gov/access/metadata/landing-page/bin/iso?id=gov.noaa.ncdc:C00516
NOTE: no long-term stations are available close to YALA with the same climatic conditions.

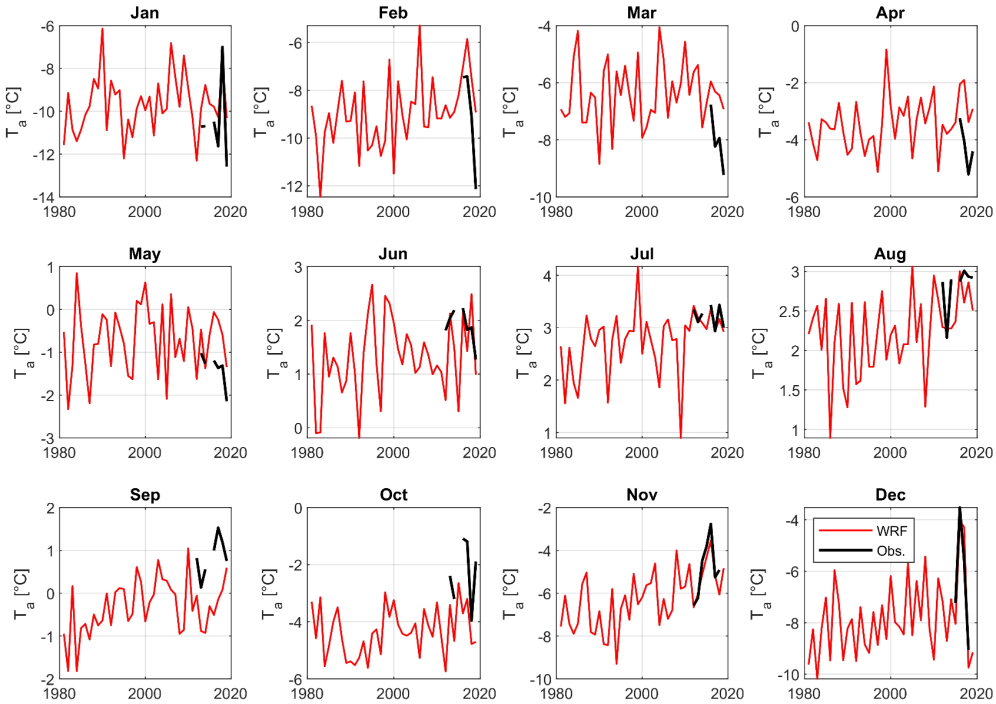

Fig. S6: Inter-annual variability in mean bias-corrected WRF air temperatures (red) and off-glacier AWS observations (black) for Yala Glacier.

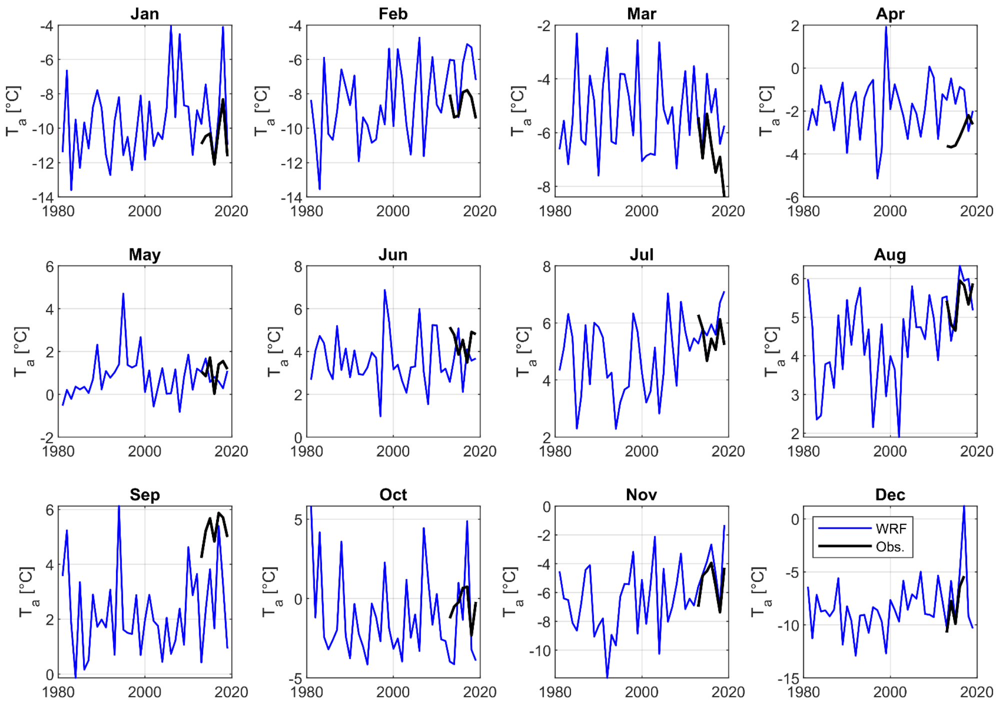

Fig. S7: Inter-annual variability in mean bias-corrected WRF air temperatures (blue) and off-glacier AWS observations (black) for Parlung 4 Glacier.

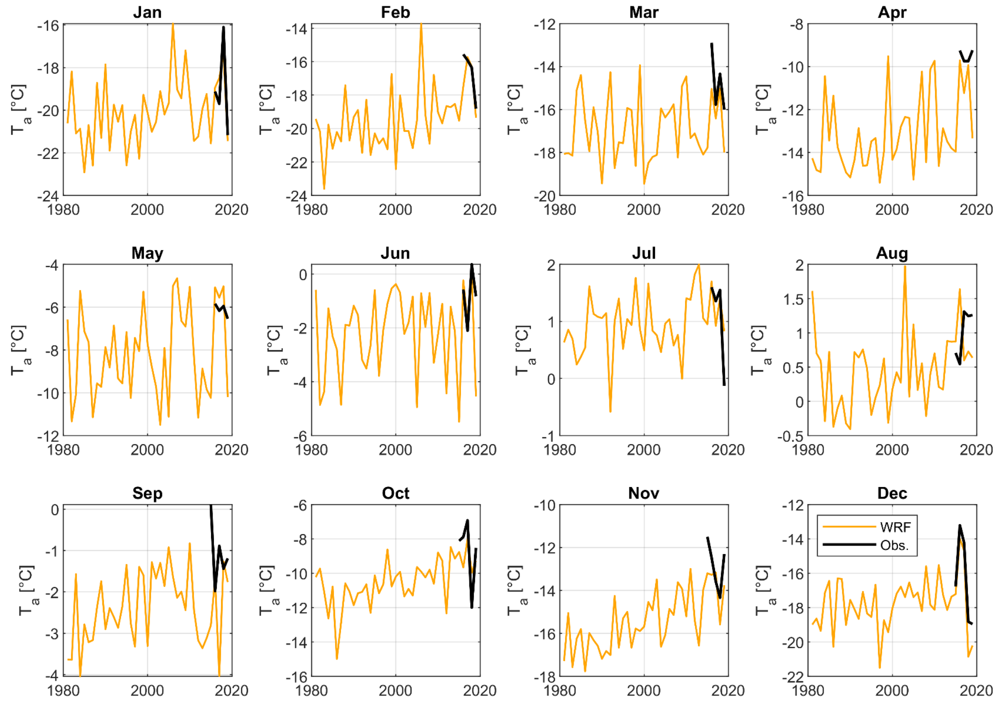

Fig. S8: Inter-annual variability in mean bias-corrected WRF air temperatures (yellow) and off-glacier AWS observations (black) for Mugagangqiong Glacier.

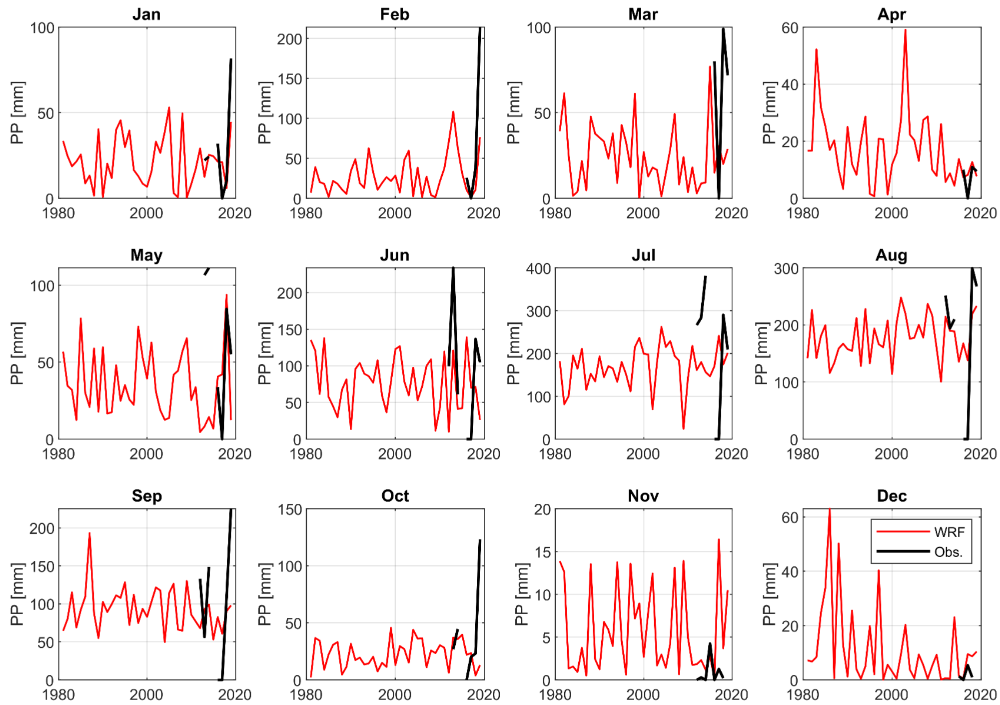

Fig. S9: Inter-annual variability in bias-corrected total WRF precipitation (red) and off-glacier AWS observations (black) for Yala Glacier.

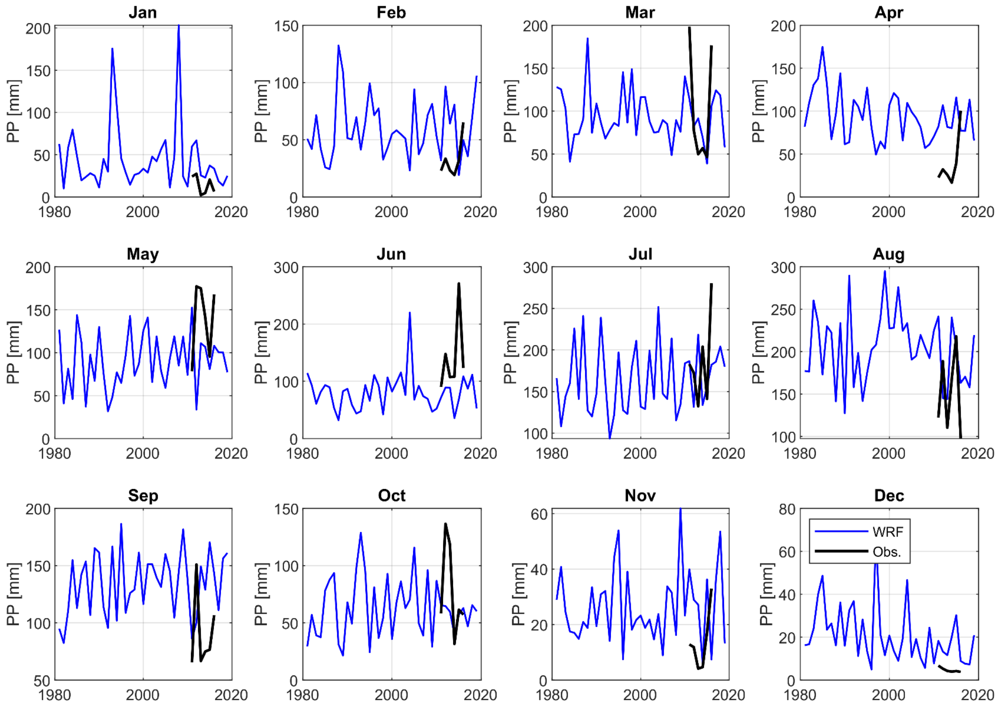

Fig. S10: Inter-annual variability in bias-corrected total WRF precipitation (blue) and off-glacier AWS observations (black) for Parlung 4 Glacier.

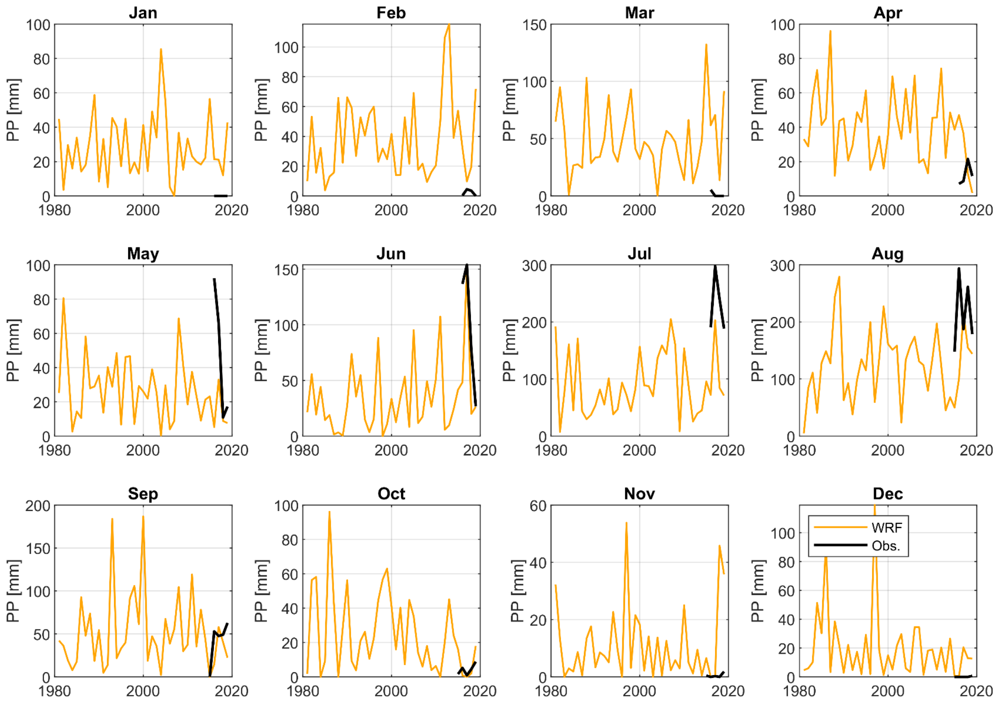

Fig. S11: Inter-annual variability in bias-corrected total WRF precipitation (yellow) and off-glacier AWS observations (black) for Mugagangqiong Glacier.

S2.2) Adjustment of meteorological variables for glacier elevations

We extrapolate the variables of interest to the elevations of the glaciers (Table 1) using locally derived and/or published vertical gradients of temperature and precipitation. The local 'MicroMet' stations, T-loggers and AWS records (Steiner et al., 2021) were used to generate hourly-monthly temperature lapse rates (Fig. S12), and temperatures were adjusted for the boundary layer cooling effect of YALA using the difference of extrapolated off-glacier temperatures and on-glacier temperatures from the AWS on the glacier at 5195 m a.s.l. (Fig. S13). A seasonally changing precipitation gradient was found by Immerzeel et al. (2014) amongst others, though these vertical precipitation gradients were derived from lower elevation stations and the valley also experiences appreciable horizontal gradients of precipitation (Immerzeel et al., 2014; Collier and Immerzeel, 2015; Bonekamp et al., 2018). Accordingly, we consider these published gradients as initial estimates, and calibrate the vertical gradients and precipitation offset factor (accounting for unknown quantities of undercatch and measurement uncertainty) further based upon temporal subsets of ablation stake data at different elevations (see Fig. S14). We consider this a suitable approach given that the gradients of air temperature are more constrained by local off- and on-glacier observations and that precipitation measurement and distribution uncertainties are larger.

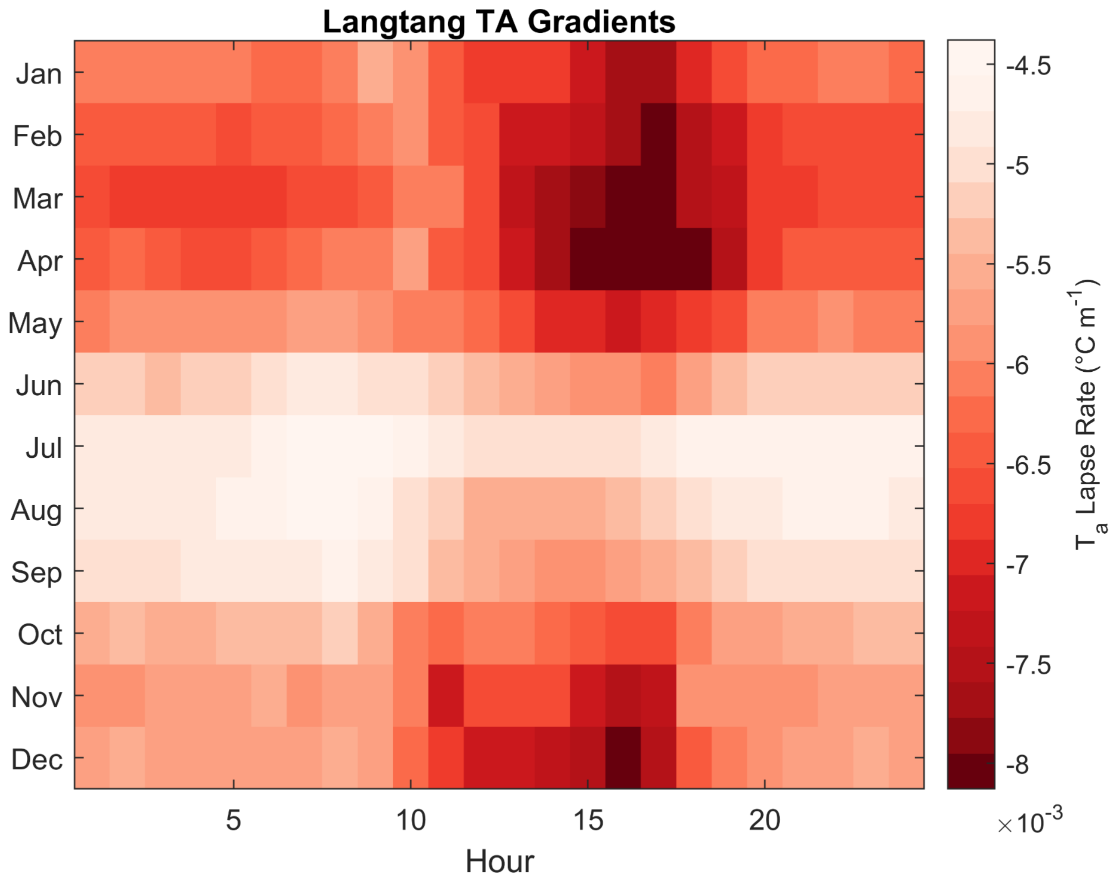

Fig. S12: The mean TA gradients / lapse rates (°C m^{-1}) for different hours and months in the upper Langtang valley (YALA). Gradients were derived between a series of high elevation stations surrounding Yala Glacier. Averages were generated from hourly data from the period 2012-2019.

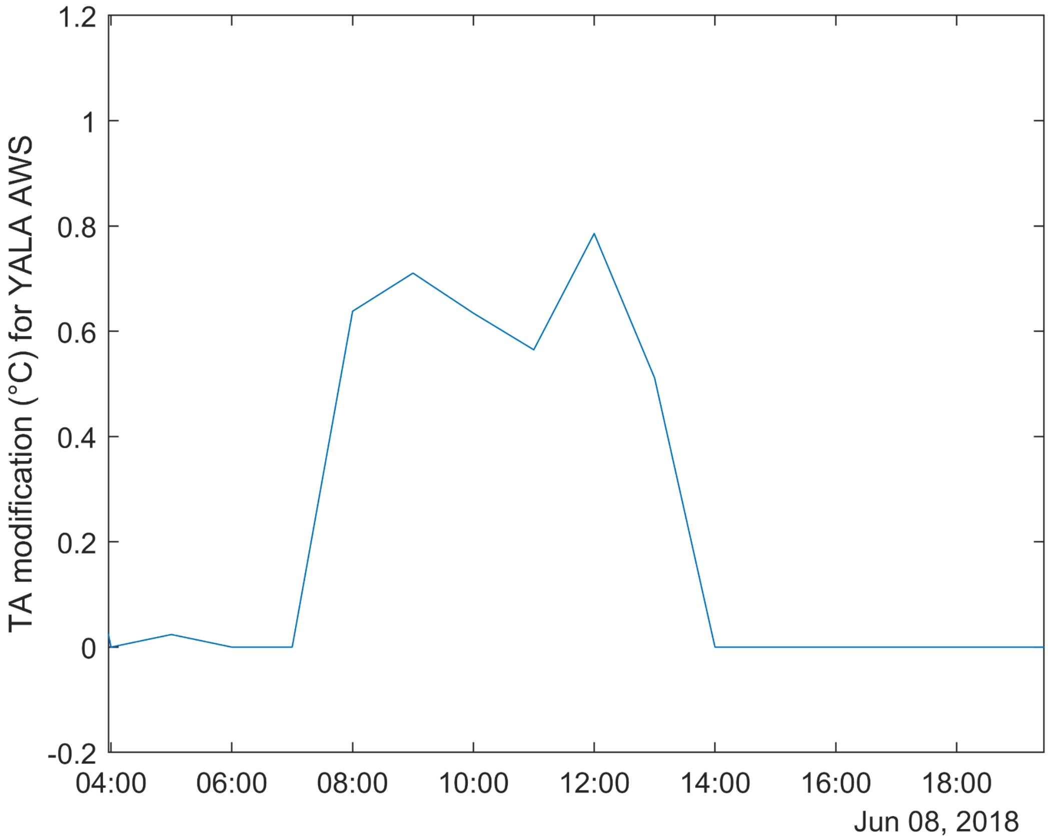

Fig. S13: An example of hourly variable temperature modification factors for YALA derived from the differences between extrapolated off-glacier TA and the on-glacier measured TA (estimated minus observed). A positive 'modification' indicates a cooler above-glacier air temperature.

For PAR4, we consider the off-glacier temperature lapse rates derived from the data of Shaw et al. (2021) for the summers of 2018 and 2019. Following Jouberton et al. (2022), we consider winter lapse rates as those from Kattel et al. (2015), due to the unreliability of high elevation temperature loggers due to thick snowpacks. As for YALA, we utilise the on-glacier AWS to generate hourly correction factors for the distributed air temperature. Jouberton et al. (2022) applied a correction factor of 1.75 and gradient of 14% m^{-1} to account for the distinct precipitation regime between the valley and the glacier. Again, we calibrate this gradient to account for the differences in forcing data for this study, though utilising the same high elevation data (2006 ice core) for calibration.

For MUGA, we distribute air temperature using published gradients for the catchment (Yang et al., 2022). Based upon the observed elevation pattern of ablation from stake data, we calibrate precipitation gradients, a temperature modification factor and a precipitation correction factor at the AWS. In calibrating precipitation gradients and precipitation correction factors, we seek to minimise mean bias and root mean squared errors when comparing the model to the multitemporal stake data. The forcing distribution parameters for each glacier are provided in Table S3.

Table S3: Overview of parameters applied to distribute meteorological forcings from the off-glacier, bias-corrected WRF dataset. 'TA LAPSE', 'TA MOD', 'PP GRAD' and 'PP OFFSET' refer to the air temperature lapse rate, air temperature modification factor over glacier surfaces, the precipitation gradient and the base station correction factor, respectively. Values in parentheses are the ranges provided in Monte Carlo runs to give an estimate of forcing uncertainty.

Parameter	**YALA**	**PAR4**	**MUGA**
TA LAPSE	Monthly-Hourly variable	Monthly-Hourly variable	-0.0055°C m^{-1}
TA MOD	Monthly-Hourly variable (±0.5°C)	Monthly-Hourly variable (±0.5°C)	0.5°C (±0.5°C)
PP GRAD	0.1% m^{-1} (±0.04% m^{-1})	0.16% m^{-1} (±0.04% m^{-1})	0.05% m^{-1} (±0.02% m^{-1})
PP OFFSET	1.82 (±0.2)	1.36 (±0.2)	1.23 (±0.2)

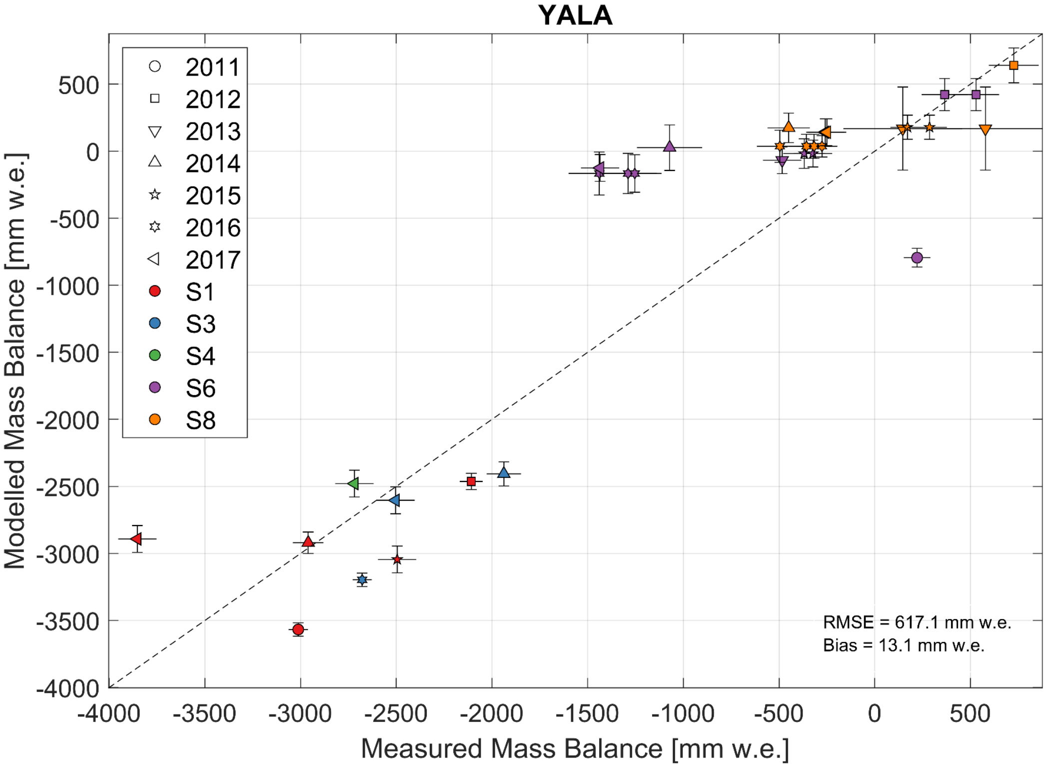
YALA
2011
2012
2013
2014
2015
2016
2017
S1
S3
S4
S6
S8
RMSE = 617.1 mm w.e.
Bias = 13.1 mm w.e.
Modelled Mass Balance [mm w.e.]
Measured Mass Balance [mm w.e.]
500
0
-500
-1000
-1500
-2000
-2500
-3000
-3500
-4000
-4000
-3500
-3000
-2500
-2000
-1500
-1000
-500
0
500

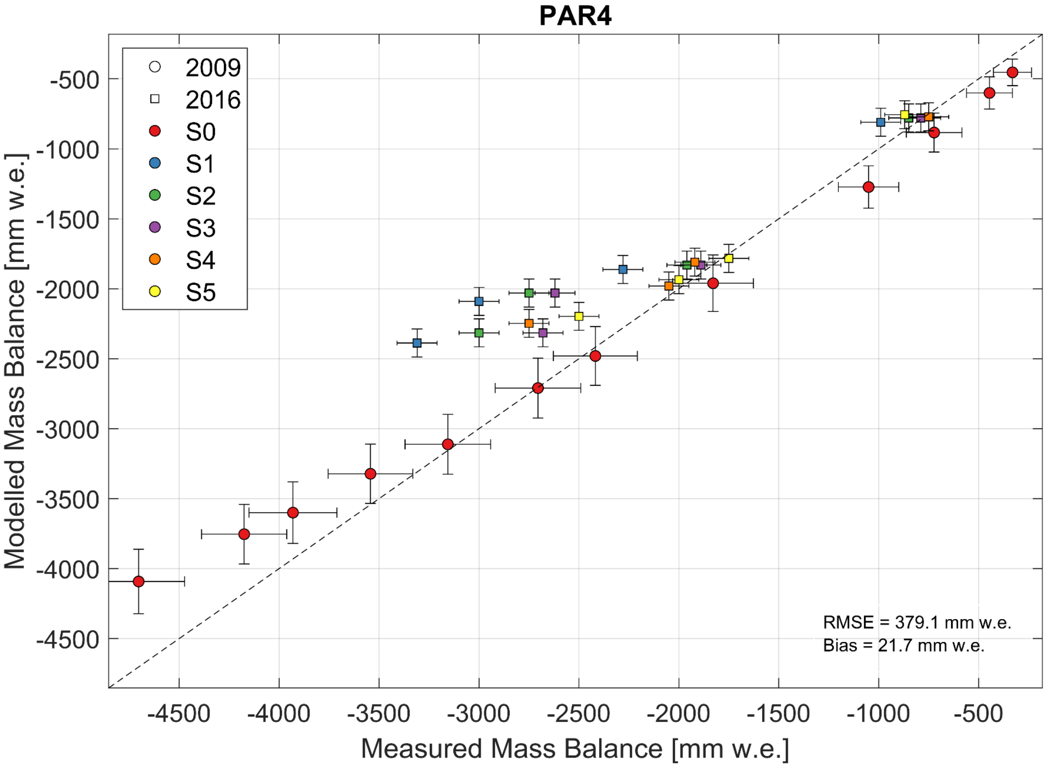
PAR4
2009
2016
S0
S1
S2
S3
S4
S5
RMSE = 379.1 mm w.e.
Bias = 21.7 mm w.e.
Modelled Mass Balance [mm w.e.]
Measured Mass Balance [mm w.e.]
-500
-1000
-1500
-2000
-2500
-3000
-3500
-4000
-4500
-4500
-4000
-3500
-3000
-2500
-2000
-1500
-1000
-500

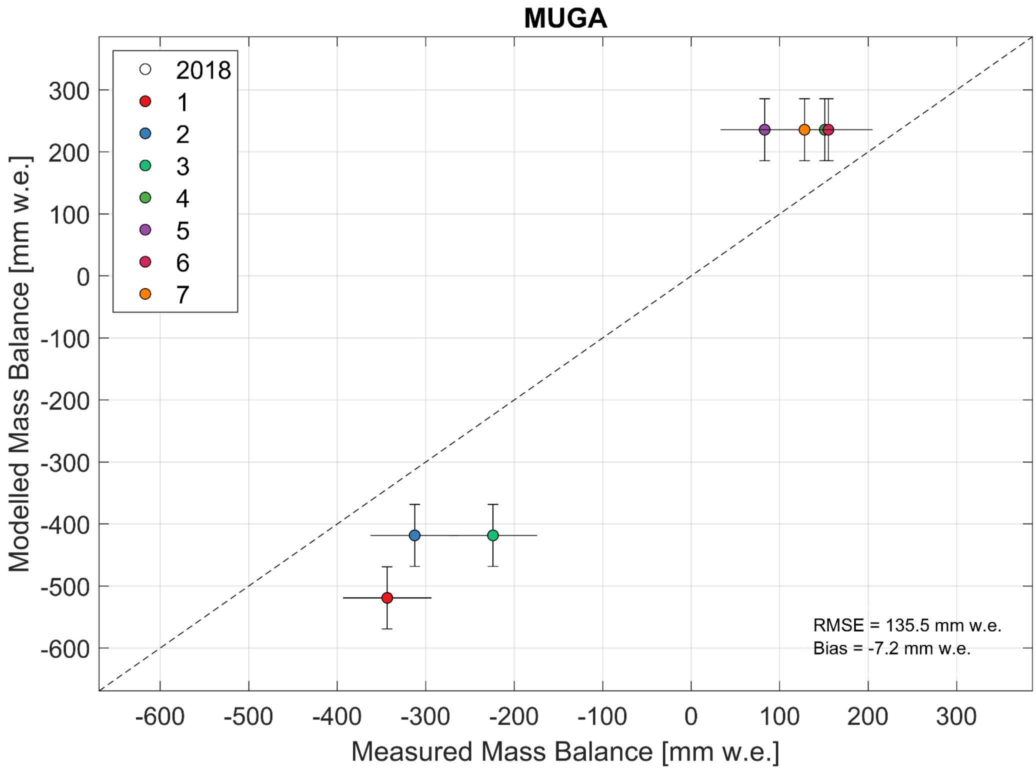

Fig. S14: Calibration of model parameters for temperature and precipitation distribution against observed stake observations for multiple elevations (colour) and years (shape).

S2.3) Tethys-Chloris model, parameterisations and assumptions

We use the detailed land surface model, Tethys-Chloris (T&C) (Fatichi et al., 2012; Mastrotheodoros et al., 2020; Fugger et al., 2021; Fyffe et al., 2021) to simulate the mass and energy balance of each glacier (Fig. S8). We apply the model at a semi-distributed scale with 50 m elevation bands, typically aligning with the on-glacier AWS and ablation stake locations. T&C simulates the energy fluxes of the ice/snow surface and subsurface (including supraglacial debris cover layers, though not relevant to this study), according to the local conditions. The surface energy balance is given for snow:

$$Rn_{SNOW} + Qv_{SNOW} + Qfm_{SNOW} - H_{SNOW} - LE_{SNOW} - G_{SNOW} - dQ_{SNOW} = 0, \quad [1]$$

and for ice:

$$Rn_{ICE} + Qv_{ICE} - H_{ICE} - LE_{ICE} - G_{ICE} - dQ_{ICE} = 0, \quad [2]$$

where *Rn* (Wm^{-2}) is the net radiation absorbed by the surface, Qv (Wm^{-2}) is the energy from precipitation, Qfm (Wm^{-2}) is the energy gained or released by melting or refreezing within the snowpack, H (Wm^{-2}) and LE (Wm^{-2}) are the sensible and latent energy fluxes and G (Wm^{-2}) is the conductive energy flux from the surface to the subsurface. Conduction of energy within ice is represented to a depth of 2m after which it is assumed the ice pack is isothermal. Finally, dQ (Wm^{-2}) is the net energy input to the snow or ice pack. The sign convention is such that fluxes are positive when directed towards the surface. To close the energy balance, a prognostic temperature for the surface is estimated for each computational element. Iterative numerical methods are used to solve the non-linear energy budget equation until convergence for the ice and snow surface temperature, and the heat diffusion equation for the debris surface, while concurrently computing the mass fluxes resulting from snow and ice melt and sublimation. For a full description of the model components, we refer the reader to Fugger et al. (2022), though specify here some of the main assumptions considered in our study.

Precipitation partitioning: We follow the approach of Ding et al. (2014) in order to distinguish between the phase of total precipitation used to force the model. This approach calculates the phase (including mixed phase, sleet events) based upon the wet bulb temperature, using the extrapolated values of TA, RH and PR. The parameterisation was developed based upon >600 meteorological stations across China, including areas of HMA near all study sites, and thus has not been recalibrated.

Albedo: We consider the albedo parameterisation of Ding et al. (2017) which was developed for PAR4 using data presented in this study. Their approach approximates the albedo of fresh snow and mixed-phase precipitation based upon its grain size and albedo decay through snow ageing, following Baker et al. (1990) and Verseghy (1991). When snowfall or sleet occurs, the basic albedo changes drastically with the snow mass, solid percentage of precipitation, and snow cover fraction following:

$$\alpha_b = \alpha_b f_{sn} + \alpha_{b,0} (1 - f_{sn}), \tag{1}$$

where α_s is the basic albedo of the surface covered by fresh snow; $\alpha_{b,0}$ is the basic albedo of the surface before the start of a snowfall or sleet event, which is taken from the previous time step and f_{sn} is the snow cover fraction of the new snowfall. Parameterisations for snow grain diameter, snowfall fractions and snow ageing are the same as those described in Ding et al. (2017) - equations 18-22. We refer the reader to that work and do not repeat those values here. The validation of albedo is given in section S2.4.

Topographical shading: In order to account for variations in topographical shading along the glacier elevation bands, we adjust the bias-corrected incoming shortwave radiation data (SWIN) based upon the solar geometry and the DEM of the glacier and its surroundings, following Corripio (2003). SWIN is averaged for each hour considering all cells ± 25 m of each 50 m elevation band, thus appropriately prescribing a reduced morning and evening SWIN for those elevation bands with steeper surrounding topography.

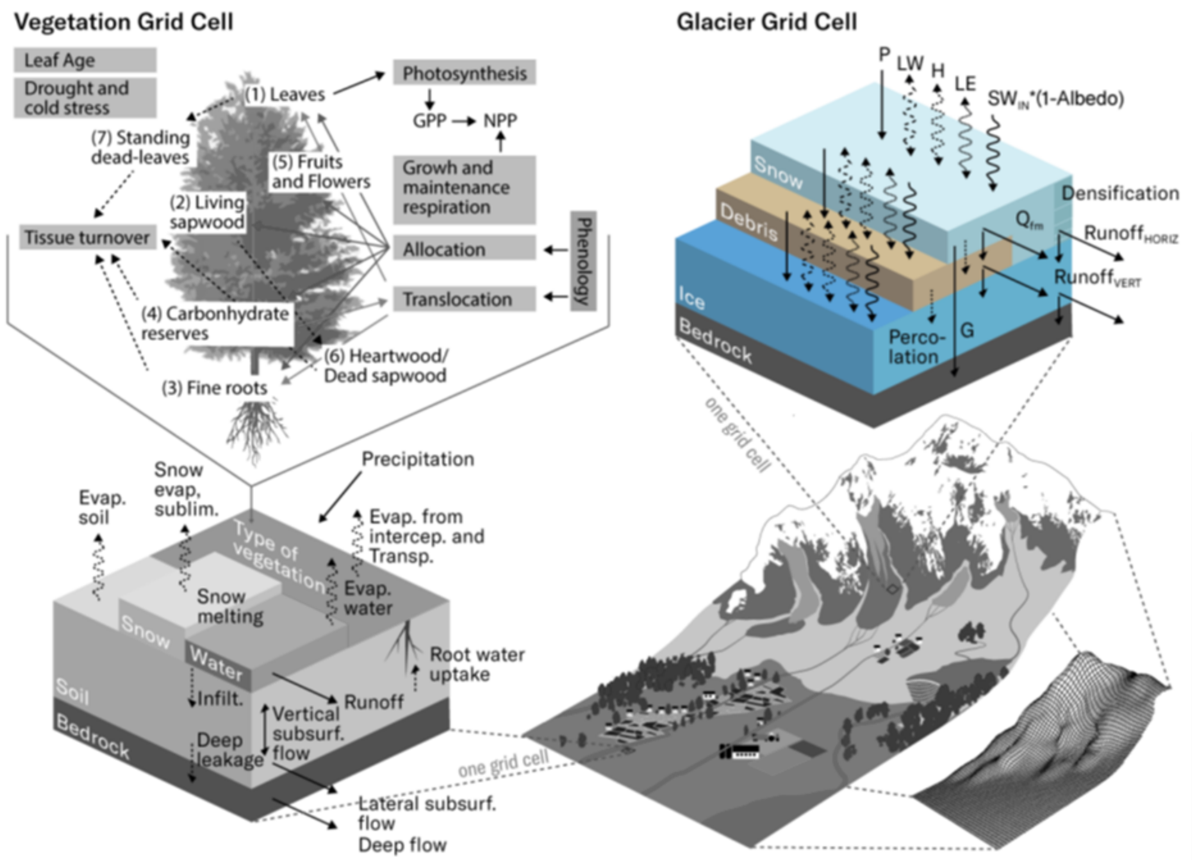

Fig. S15: A schematic of the T&C model and its separate components. Our study focuses upon only glacier-relevant processes (highlighted in colour).

Derivation of glacier-wide mass balance: In order to produce a model estimate of glacier-wide mass balance, we derive the point-based mass balance simulation for each 50 m elevation band as described in S2.2 and adjust the result based upon the area-weighted glacier hypsometry (± 25 m of that elevation band) that evolves in time. The time-evolving glacier hypsometry at each glacier is derived from published glacier outlines and DEMs and interpolated linearly in time between the available dates (Fig.s S9-S11). Outlines and DEMs for YALA are taken from Sunako et al. (2022) and the data for PAR4 are that presented by Jouberton et al. (2022). For MUGA, we derive new outlines and DEMs from imagery over the glacier (only since 2000). DEM derivation on the acquired imagery was processed in the AMES stereo pipeline utilising standard parameters (Shean et al., 2016).

For PAR4, the differences in mass input due to avalanches are modelled using the spatially distributed TOPKAPI-ETH model as presented by Jouberton et al. (2022). The differences (ranging between 0.05 - 1.3 m w.e. at 5500 ma.s.l) were added each year to the mass balance at the equivalent elevation band. The occurrence of avalanches at YALA and MUGA are deemed to be minimal and were thus neglected in this study.

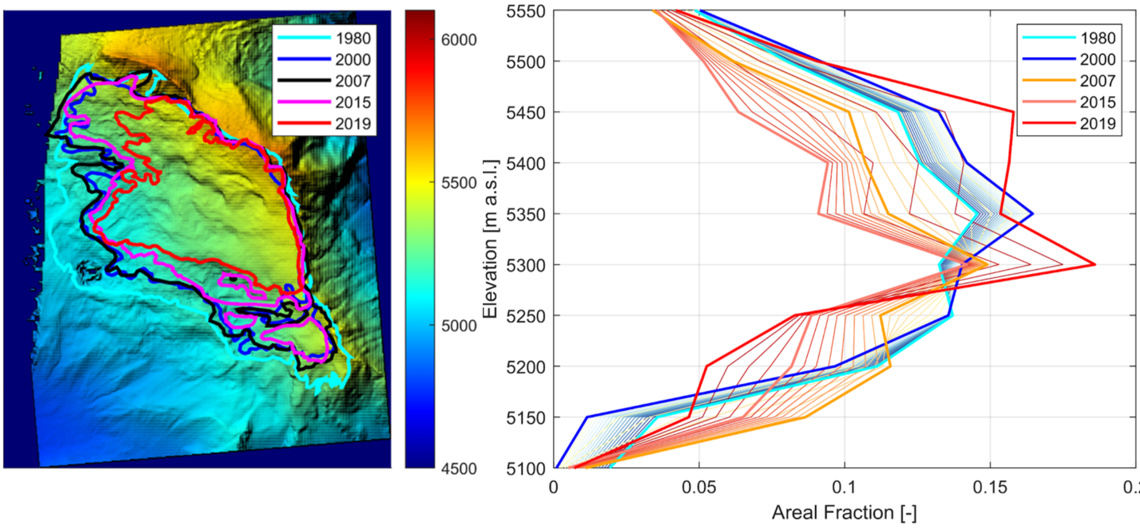

Fig. S16: The glacier area change (left) and time-evolving hypsometries (right) for YALA. Hypsometric changes are linearly interpolated in time for each elevation band between the observed years.

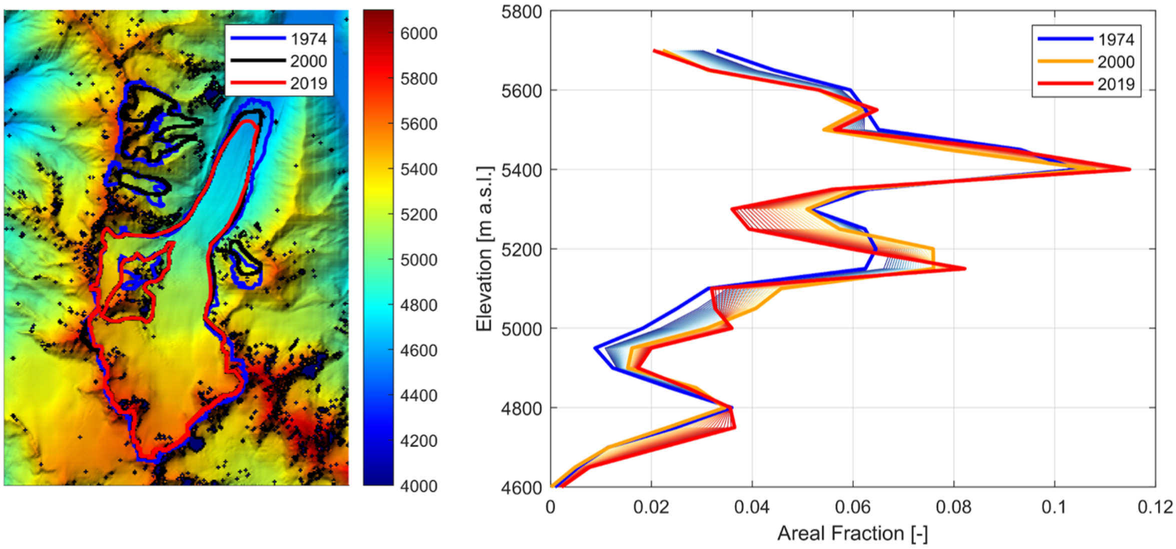

Fig. S17: As Fig. S16, but for PAR4.

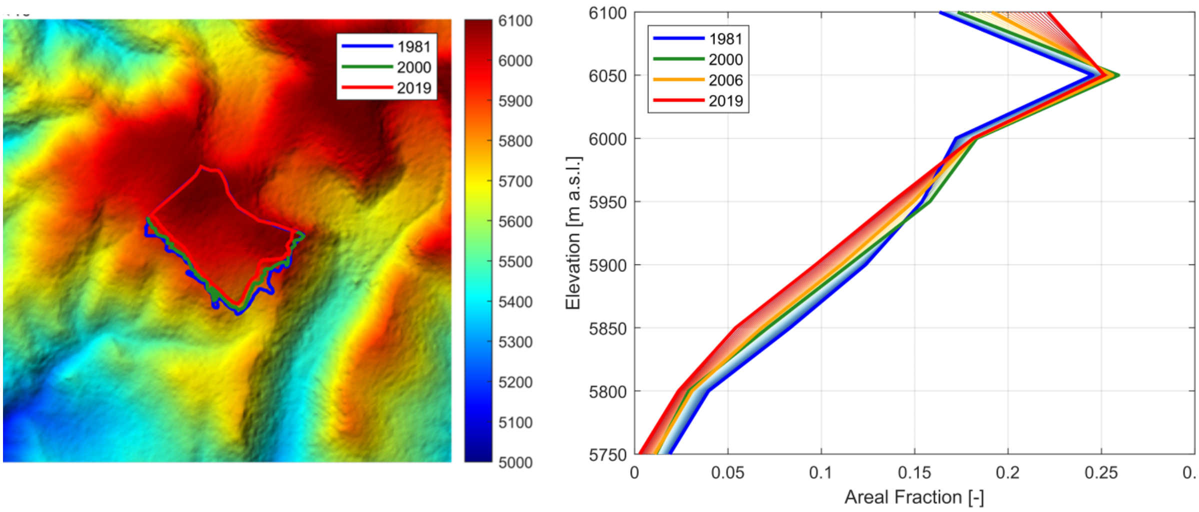

Fig. S18: As Fig. S16, but for MUGA.

Uncertainty analysis: To provide an estimate of modelled uncertainty, we perturb the main parameters utilised to offset and distribute meteorological variables in space and time. Specifically, we perturb the precipitation offset at the AWS and the precipitation gradient (Table S3) that represent unknown quantities which were initially calibrated against stake observations (Fig. S7). Additionally, as our temperature modification over glacier surfaces is based upon adjustment factors at single points (on-glacier AWS) that ignores the spatially variability in glacier cooling effects (Shaw et al., 2021) and is absent for MUGA, we also perturb this parameter. The three parameters are modified in physically realistic ranges (Table S3) and input into a 1000 run Monte Carlo simulation for the full 40 year period.

S2.4) Validation of model at glacier sites

To test the ability of the model to represent glacier changes through time, we utilise published values of glacier mass balance from multiple sources. While recent ablation stake data are used to calibrate appropriate gradients of precipitation (Fig. S14), past stake data from YALA is available from work by Fujita et al. (1997). Fig. S19 demonstrates how a reconstructed past period without available AWS records is able to be suitably modelled using the T&C model at varying elevations on YALA. Additionally, a wealth of glacier-wide mass balance records at YALA (Table S4, Sunako et al., 2022) demonstrate an agreement with the model results (Fig. S20), which typically lies within the prescribed observational uncertainty (vertical error bars).

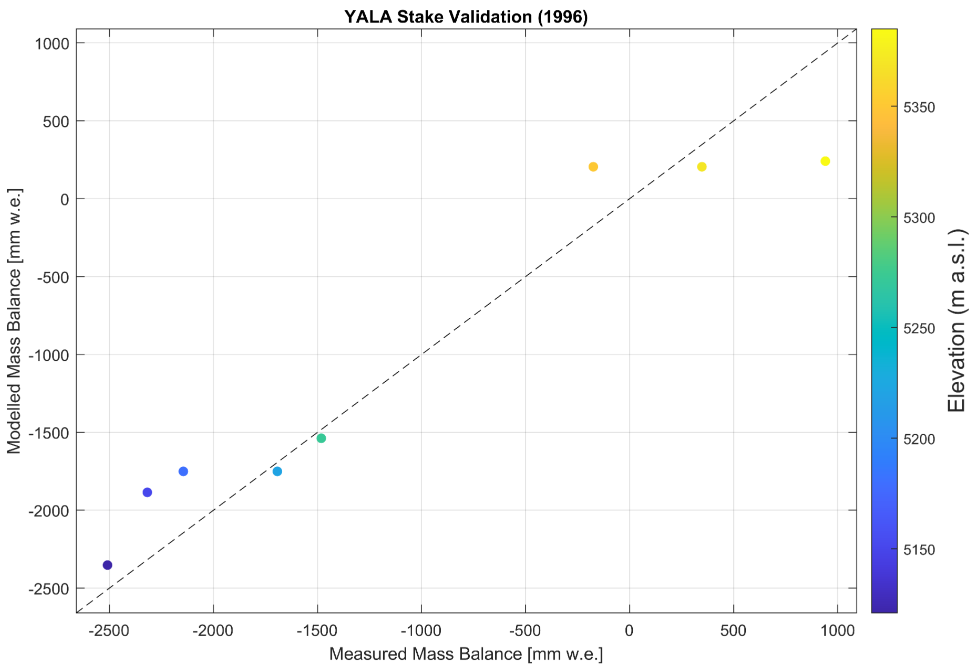

Fig. S19: Observed vs modelled mass balances based upon stake data of Fujita et al. (1997). Data are not used for calibration (cf. Fig. S14).

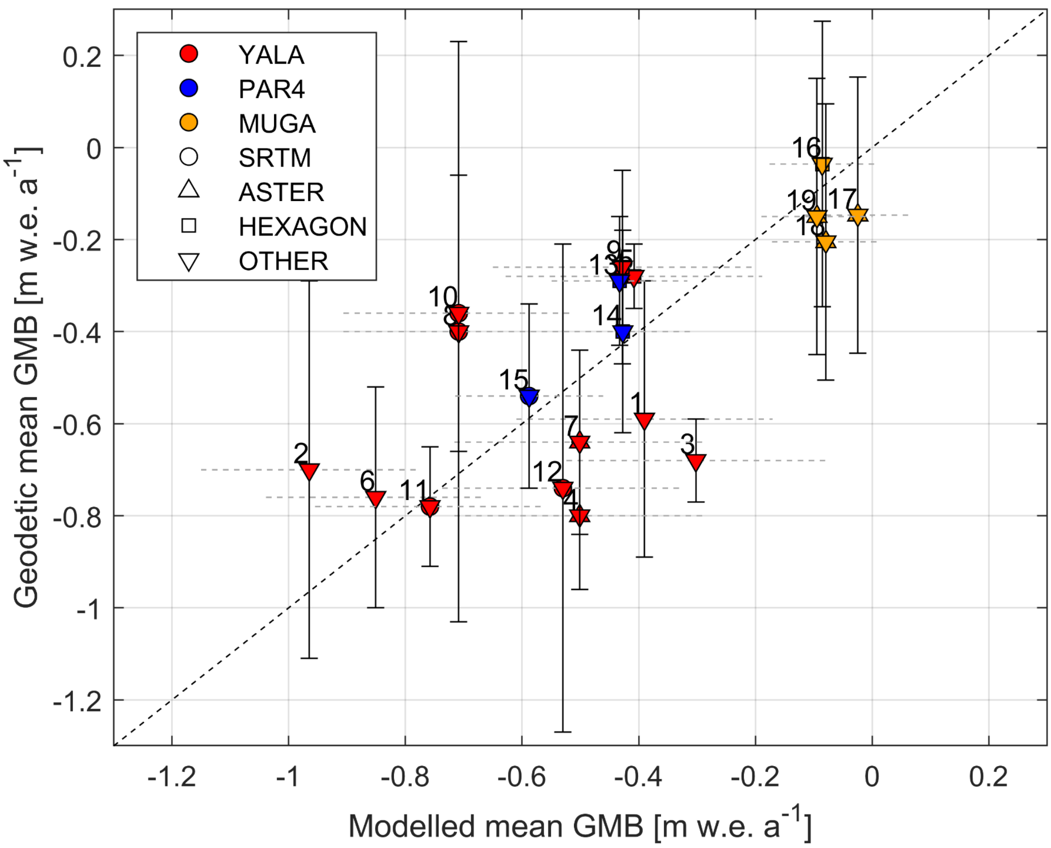

Fig. S20: Geodetic observations (y-axis) and modelled glacier-wide (x-axis) mass balance (m w.e. a^{-1}) for the comparative periods given in Table S4. Numbers refer to the individual studies given in Table S4. Vertical error bars indicate the published geodetic uncertainty values from the literature and dashed, horizontal error bars are derived from the Monte Carlo uncertainty analysis.

Table S4: Geodetic mass balance observations used to validate the outputs of the model (Fig. S20). Details are given for YALA (red), PAR4 (blue) and MUGA (Orange).

ID	*Period*	*Data*	*Reference*
1	*1981-2007*	*Digitised Map - Aerial Imagery*	*Sunako et al. (2022)*
2	*2007-2015*	*Aerial Imagery - UAV survey*	*Sunako et al. (2022)*
3	*1981-1996*	*Ground Photos - Theodolite*	*Fujita and Nuimura (2011)*
4	*1996-2009*	*Theodolite - dGPS survey*	*Fujita and Nuimura (2011)*
5	*1981-2006*	*Hexagon - Cartosat*	*Ragettli et al. (2015)*
6	*2006-2015*	*Cartosat*	*Ragettli et al. (2015)*
7	*1996-2009*	*Theodolite - dGPS survey*	*Suigyama et al. (2013)*
8	*2000-2016*	*ASTER*	*Brun et al. (2017)*
9	*1981-2000*	*Hexagon - ASTER*	*Maurer et al. (2019)*

10	*2000-2016*	*ASTER*	*Maurer et al. (2019)*
11	*2000-2018*	*ASTER - Worldview*	*Shean et al. (2020)*
12	*2000-2012*	*SRTM - GeoEye*	*Stumm et al. (2019)*
13	*1981-2000*	*Hexagon - SRTM*	*Jouberton et al. (2022)*
14	*1981-2014*	*Hexagon - TANDEM-EX*	*Jouberton et al. (2022)*
15	*2000-2017*	*SRTM - ZY3*	*Ren et al. (2020)*
16	*2006-2019*	*ALOS PALSAR - DEIMOS*	*This Study*
17	*2000-2010*	*ASTER*	*Hugonnet et al. (2021)*
18	*2010-2019*	*ASTER*	*Hugonnet et al. (2021)*
19	*2015-2019*	*ASTER*	*Hugonnet et al. (2021)*

While some care should be given to the interpretation and uncertainty of all the different observations reported (see cited articles for methodological details), the modelled mass balances are reasonably comparable to most geodetic observations. For PAR4 and MUGA, there are fewer observations available, though the mass balances, which act as independent validation data, agree closely with the modelled estimates.

Additional validation of the model comes from satellite-derived surface albedo data. Fig. S21 gives an example of PAR4 snow albedo modelled by T&C and estimated from Landsat 8 imagery, following Ren et al. (2021). At lower elevations, the changing surface type (from snow to ice) results in an over-estimation of surface albedo from the model, though in general the agreement is strong. Validation against on-glacier AWS-derived albedo also provides an indication that the model is able to replicate the seasonal and sub-seasonal variability in albedo well (Fig. S22-23). We note that on-glacier data are scarce and sensor tilt and related issues have limited the temporal period for which albedo can be confidently validated. The performance in this regard is similar to that modelled by previous studies of this type (e.g. Zhu et al., 2018). Moreover, we find that earlier studies applying these same parameterisations within the same land surface model were able to appropriately model the albedo of glaciers in Peru (Fig. S4 of SI in Fyffe et al., 2021) and HMA, including two of the sites of this study (Fugger et al., 2022).

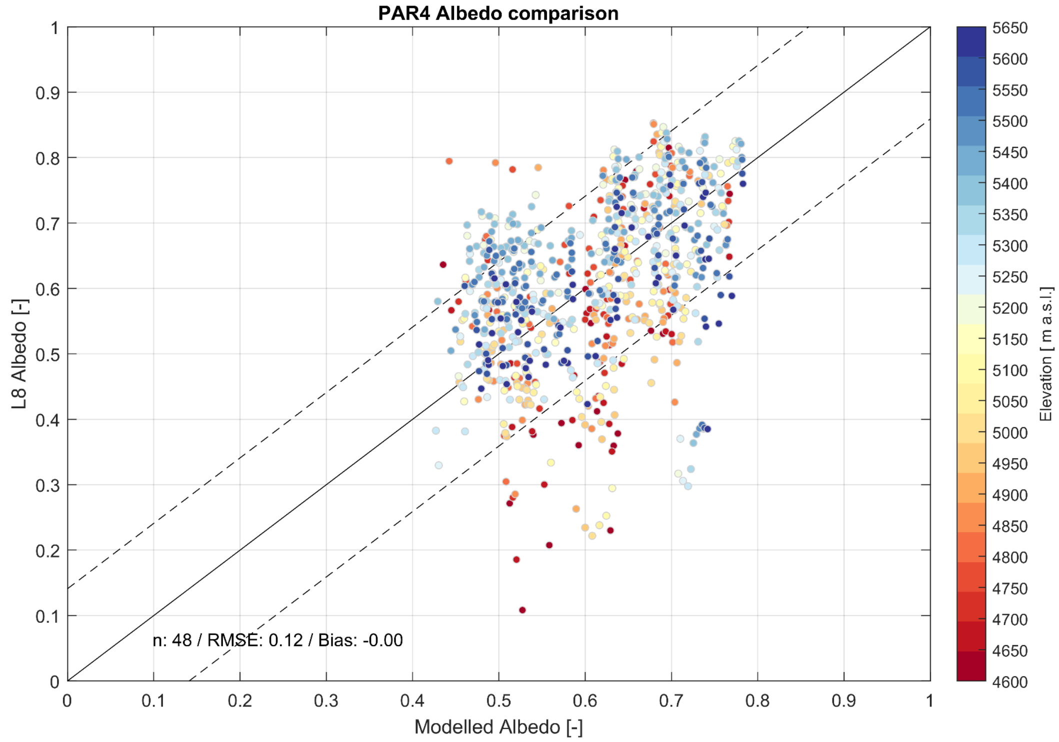

Fig. S21: Example of snow albedo validation using Landsat 8 albedos, derived following Ren et al. (2021). Each point represents the mean albedo for a given observation date at different elevation bands (colours). The dashed lines indicate the mean of the standard deviations from observations either side of the 1:1 line (error bars are not shown for neatness).

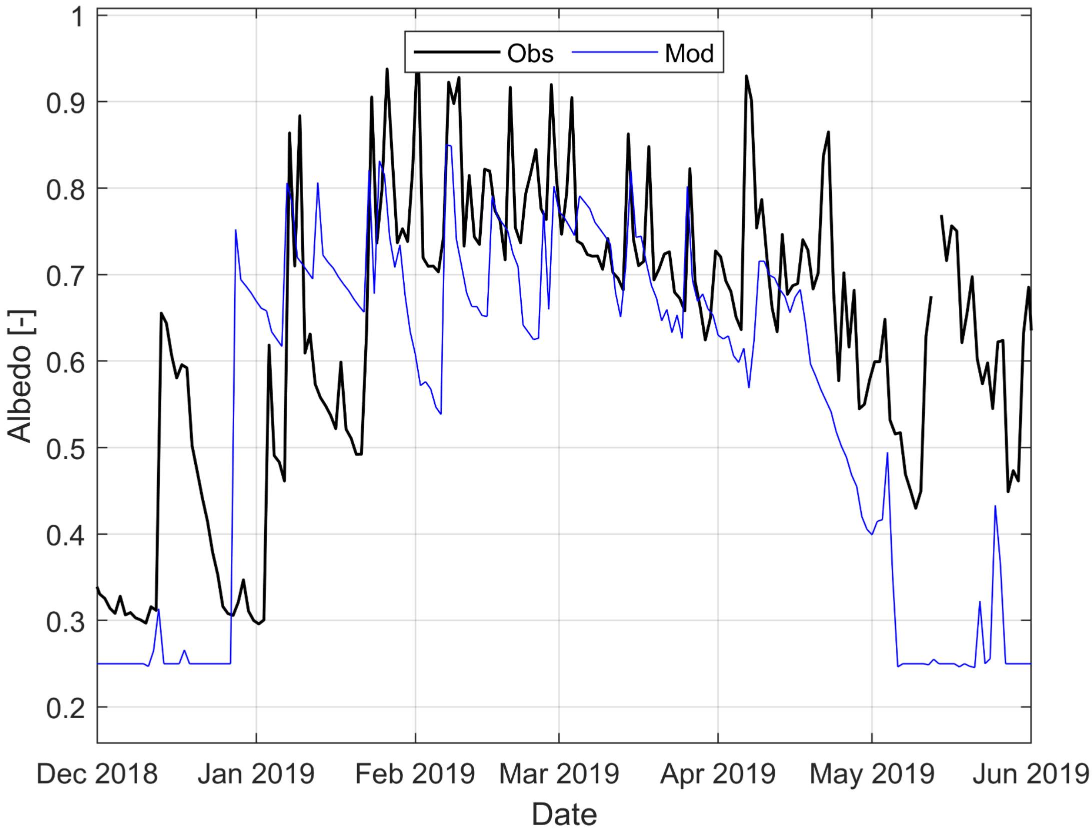

Fig. S22: Validation of modelled albedo (blue) against on-glacier AWS observations at Yala Glacier.

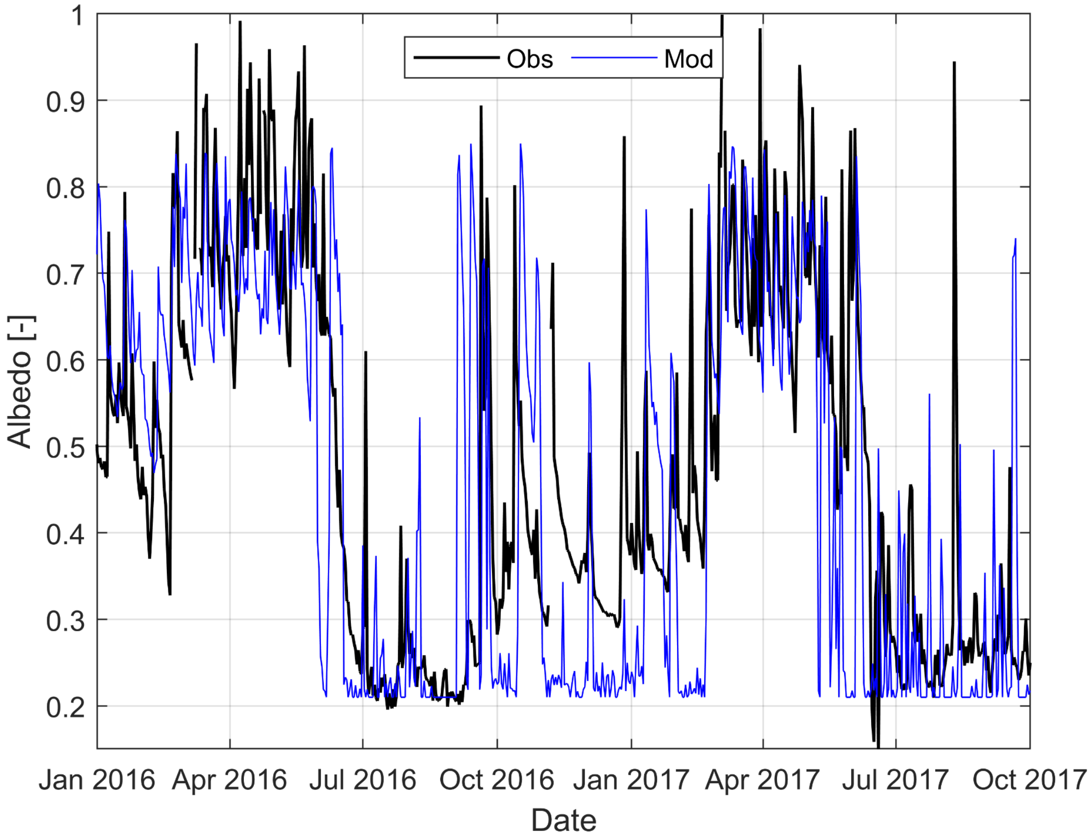

Fig. S23: Validation of modelled albedo (blue) against on-glacier AWS observations at Parlung 4 Glacier.

S2.5) Examples of Horizontal Wind Shear Index (HWSI) monsoon classification

We classify the monsoon occurrence following the approach of Prasad and Hayashi (2007) as employed in similar works by Mölg et al (2012; 2014) and Li et al. (2018), though utilising ERA5 data. We provide examples of the inter-annual variability in the index and the derivation of onset and cessation days and active and break periods in Fig.s S24-S26. We follow those studies in defining active and break periods as >1σ and >1.5σ in the HWSI and northern zonal winds, respectively. Monsoon intensity is defined here as the normalised mean HWSI between June and September. The summary of monsoon conditions are given in Fig. S27.

We note that the monsoon timings derived from the HWSI in this study are similar to those derived from ERA5 precipitation data in Zhu et al. (2020). However, our timings and analysis are partly different to those aforementioned works given a longer timescale (2009-2011 in Mölg et al. (2012) and 2013-2016 in Li et al. (2018)) and those studies utilised different reanalysis forcings (NCEP-NCAR in Mölg et al. (2012)). We therefore caution against a direct comparison of our results to those earlier studies and we consider this in our interpretation of results (see main text).

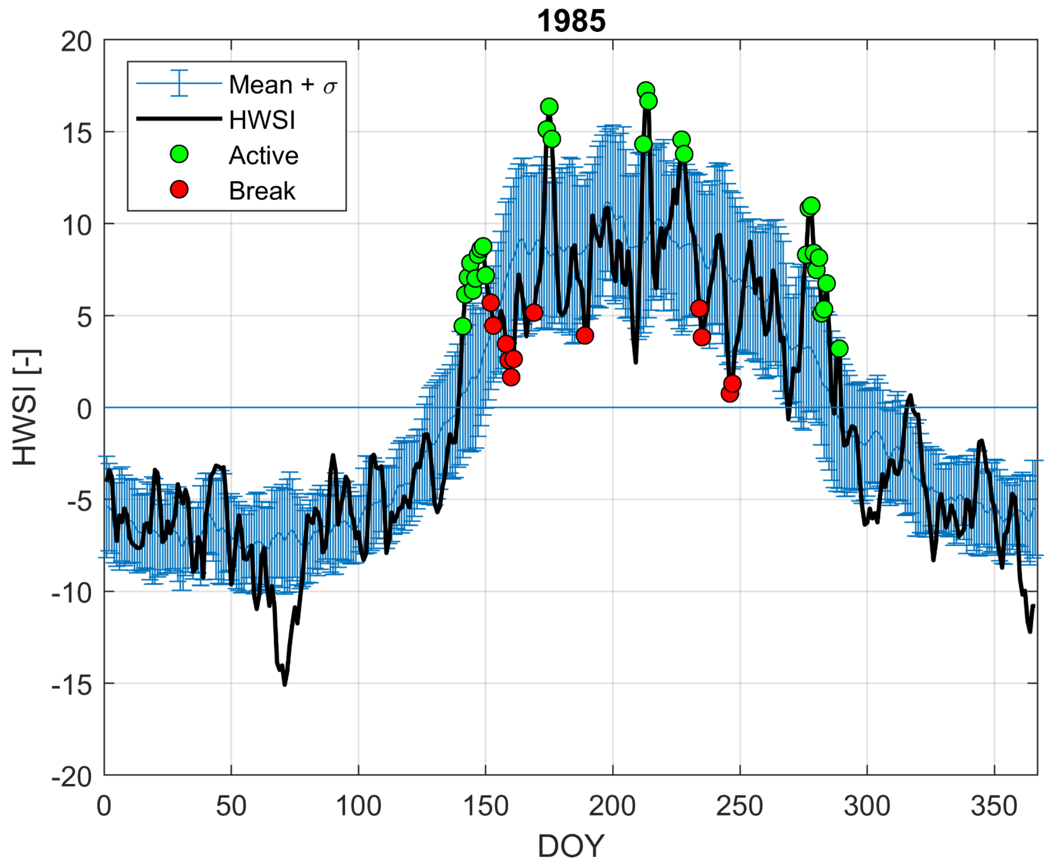

Fig.S24: The regional horizontal wind shear index (HWSI) for 1985 (black line) following Prasad and Hayashi (2007). The mean and standard deviation of the whole period is shown by the error bars. The active periods (green) are defined as those events > 1σ of the total period. Break periods (red) are defined as those > 1.5σ in the northern region, indicative of westerly disruption.

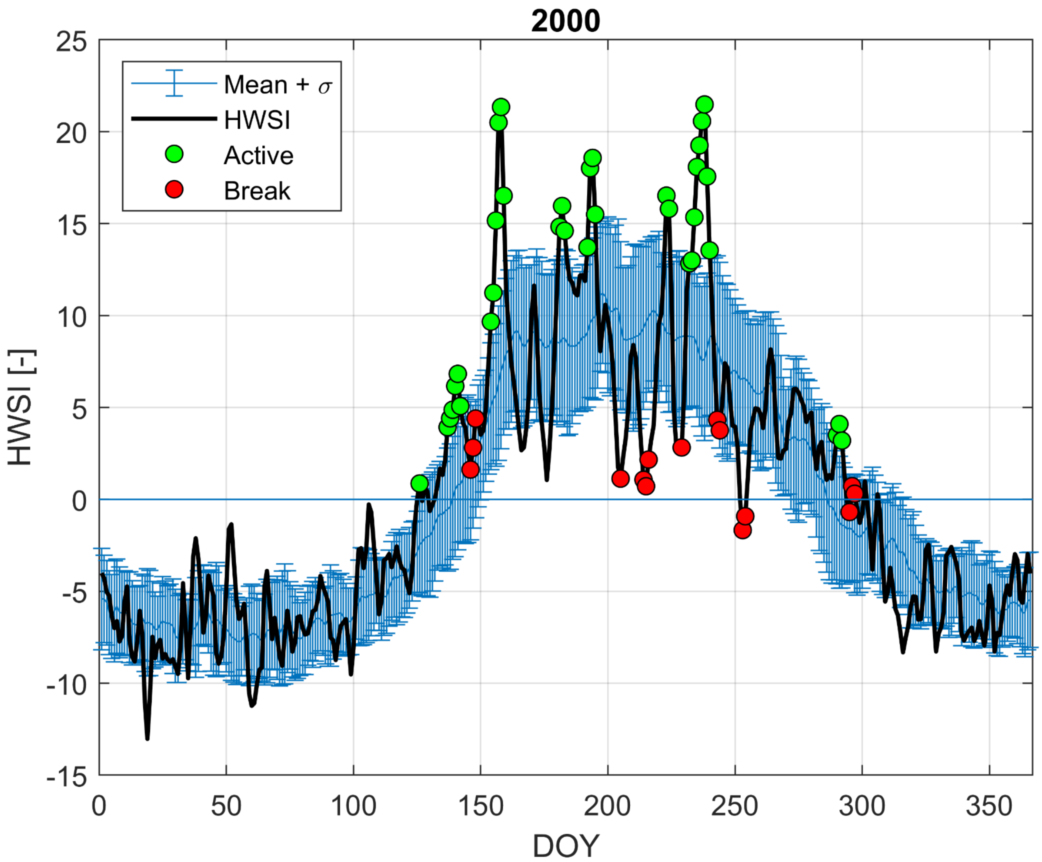

Fig.S25: As Fig. S24, but for the year 2000.

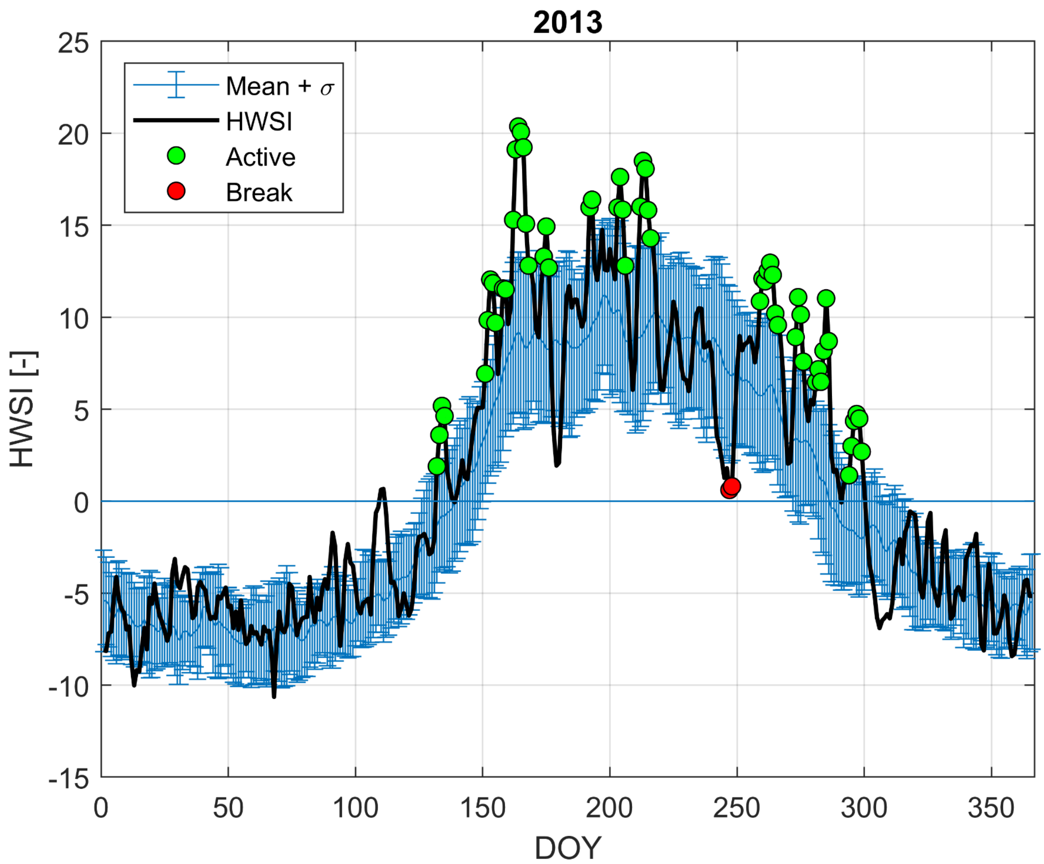

Fig.S26: As Fig. S24, but for the year 2013.

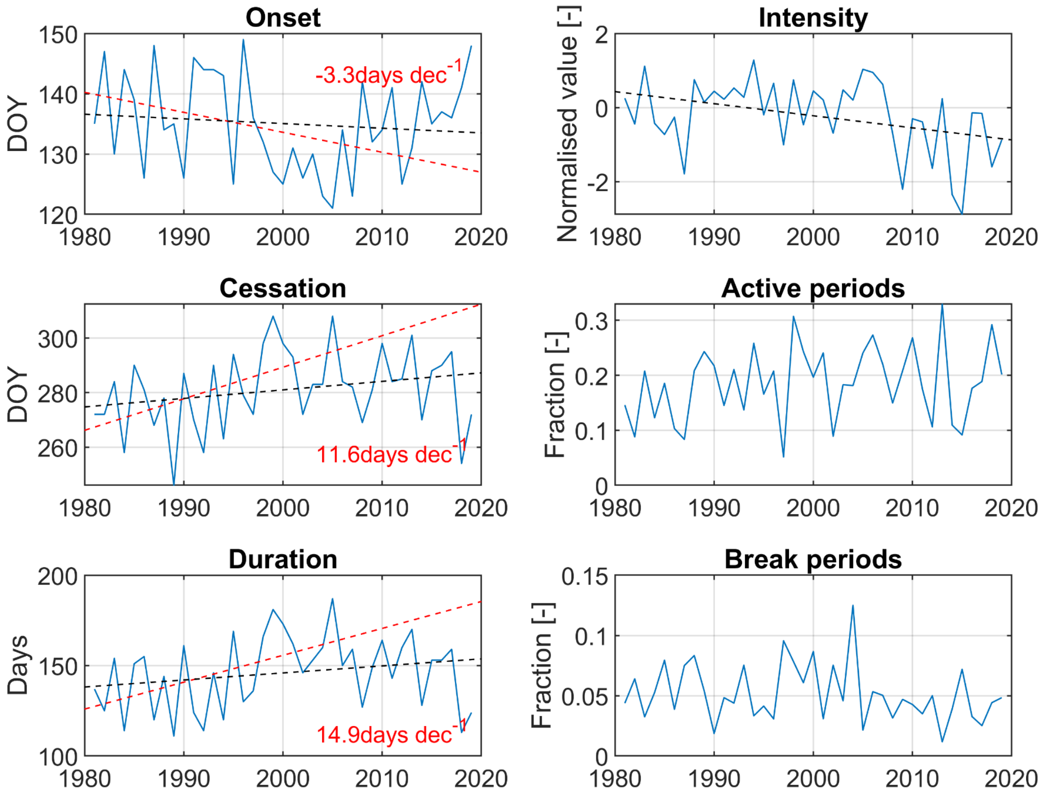

Fig. S27: The summary of monsoon conditions (1981-2019) based upon the HWSI. Black dashed lines indicate the trend lines for the full period, while red dashed lines indicate the pre-millenium trend (with values reported for monsoon timing).

S3) ADDITIONAL RESULTS

S3.1) Regional trends in WRF datasets

To support the key results of the main text, we present trends and patterns of WRF meteorology across HMA in Fig.s S28-S35. Trends in air temperature are found to be significant across the entire HMA based upon the atmospheric model output (Fig. S28), however with a strong seasonality (Fig. S30). While the spring period and monsoon onset period shows no significant trend in air temperature, both late winter (February) and late summer (August-September) months show increases up to 0.8-1°C dec^{-1}. These temperature trends are generally consistent with other results (Li et al., 2020) and winter warming suggested by WRF relates well with the snow water equivalent patterns in SE-TP (Smith and Bookhagen 2020). Other variables demonstrate only patchy trends of significance over the analysis period and relevant only to given months of the year. This is notable for precipitation (Fig. S29) which indicates some drying of the upper Brahmaputra Valley and wetting for parts of central Tibet in summer (Fig. S31). Other variables, such as humidity and shortwave radiation have trends coincident with precipitation due to their high correlation. The trends suggest a slackening of winds across central TP in March and increased storminess in November (Fig. S33). Interestingly, trends in cloudiness (increase in longwave radiation and decrease in shortwave radiation) at the glacier sites, with humidity showing notable increases at YALA and MUGA as well (Fig. S34). Consistent with the regional patterns around western-central Tibet, the increase of humidity and cloudiness are strongest for MUGA (Fig. S35).

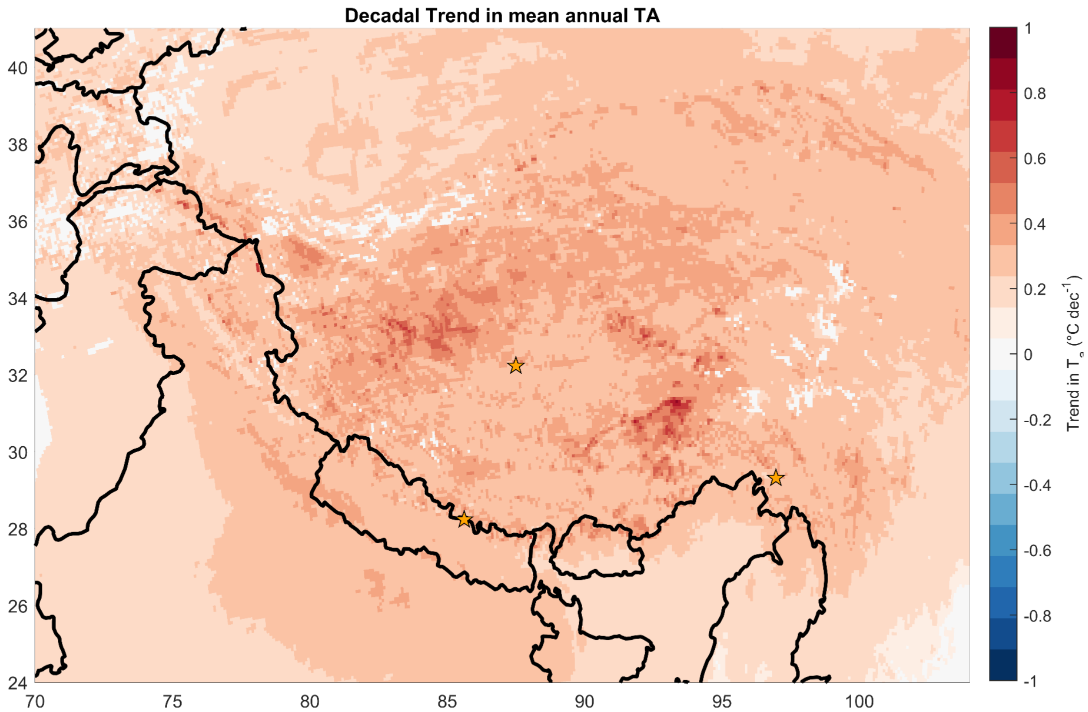

Fig.S28: Decadal trends in mean annual air temperature (°C) derived from WRF (1980-2019). Stars indicate the location of the three glacier sites for this study. Trends not significant to the 0.05 level are not shown.

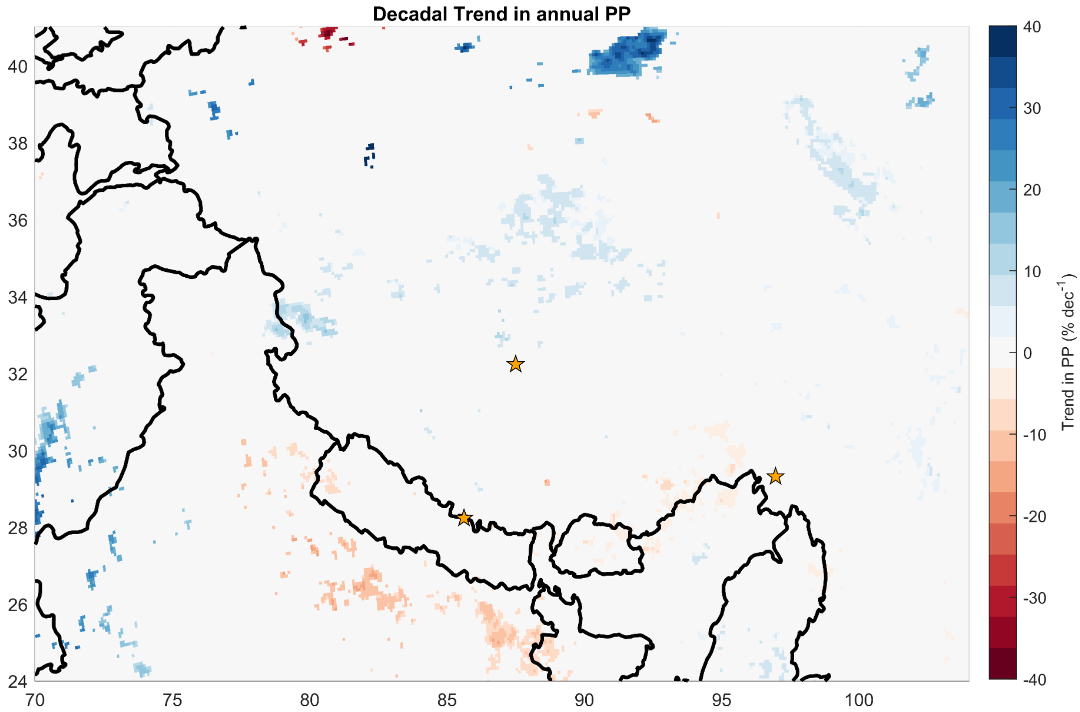

Fig. S29: As Fig. S28, but for decadal trends in annual total precipitation (% relative to the mean of all years)

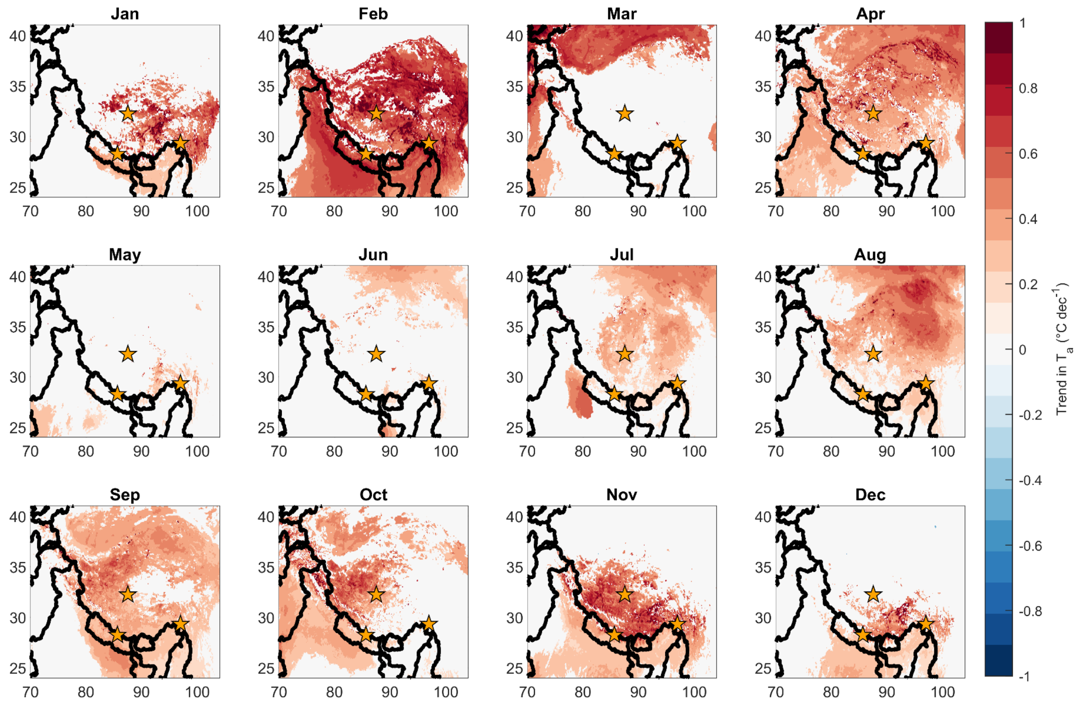

Fig. S30: Decadal trends in monthly mean air temperature (°C) derived from WRF (1980-2019). Stars indicate the location of the three glacier sites for this study. Trends not significant to the 0.05 level are not shown.

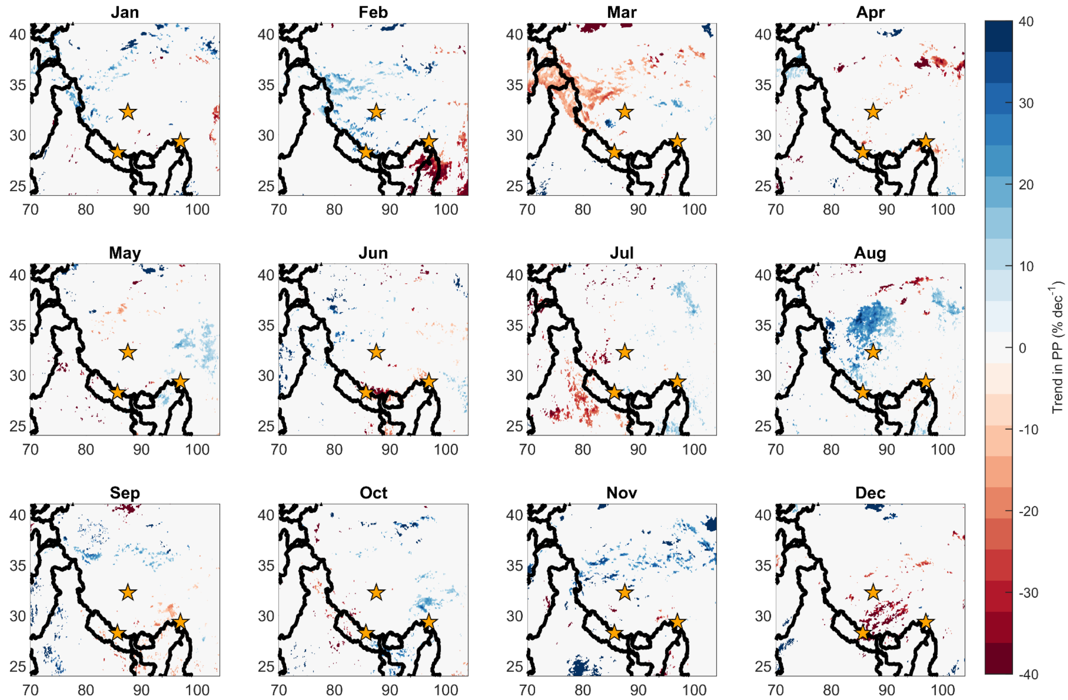

Fig. S31: As Fig. S30, but for decadal trends in monthly total precipitation (% relative to the mean of all years)

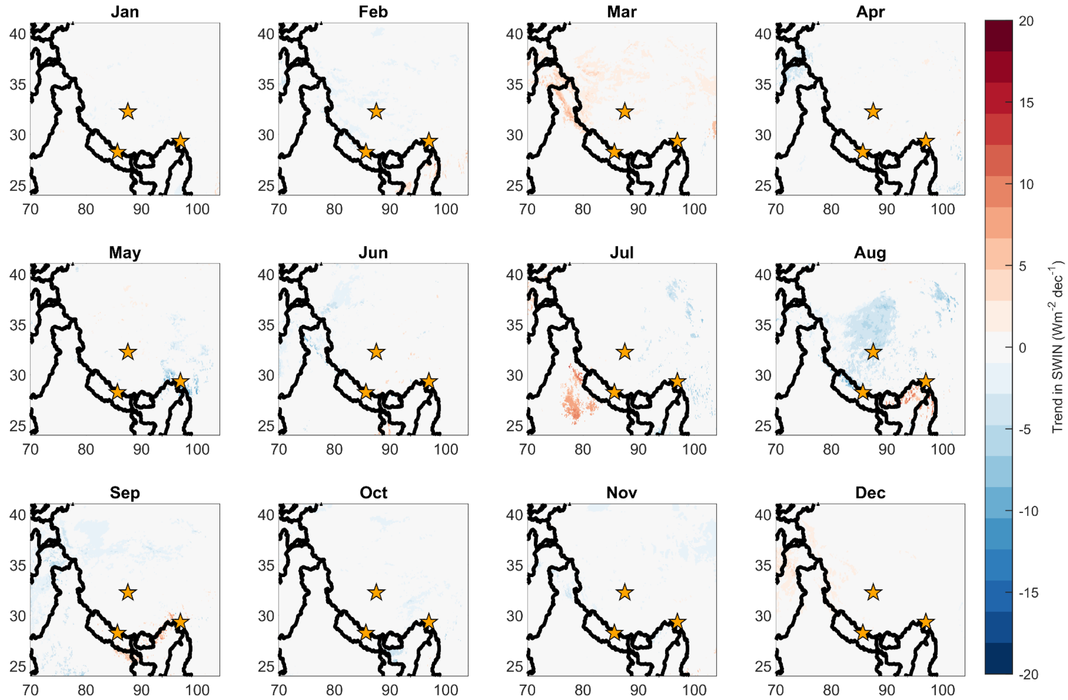

Fig. S32: As Fig. S30, but for decadal trends in mean monthly Shortwave radiation (Wm^{-2}).

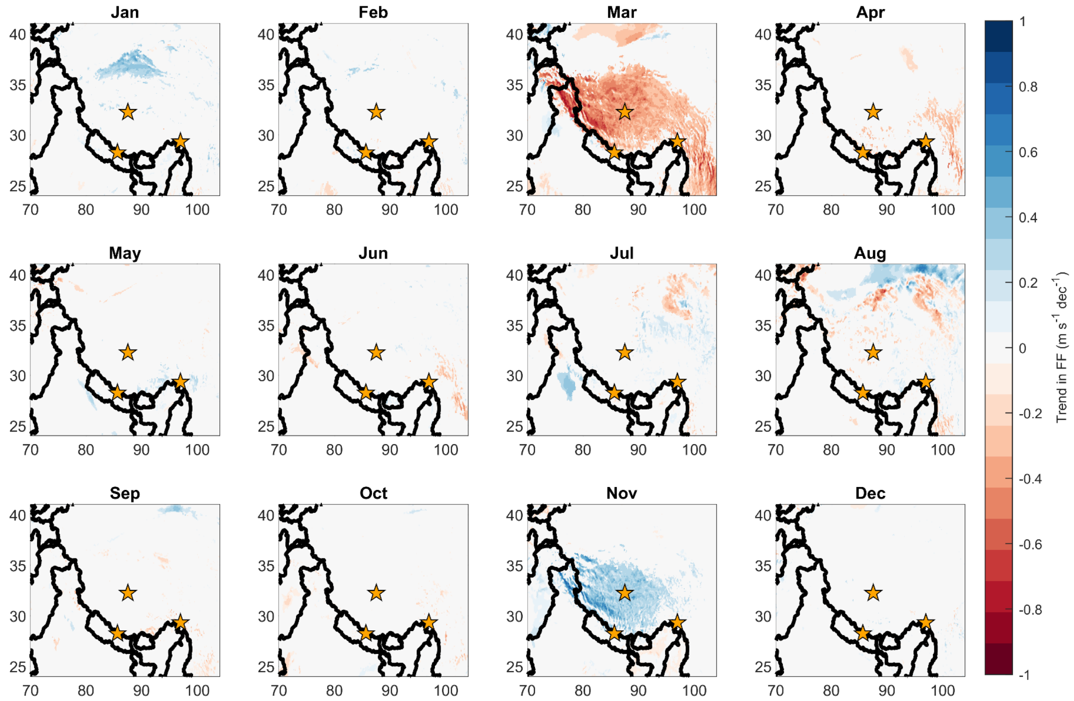

Fig. S33: As Fig. S30, but for decadal trends in mean monthly wind speeds (m s^{-1}).

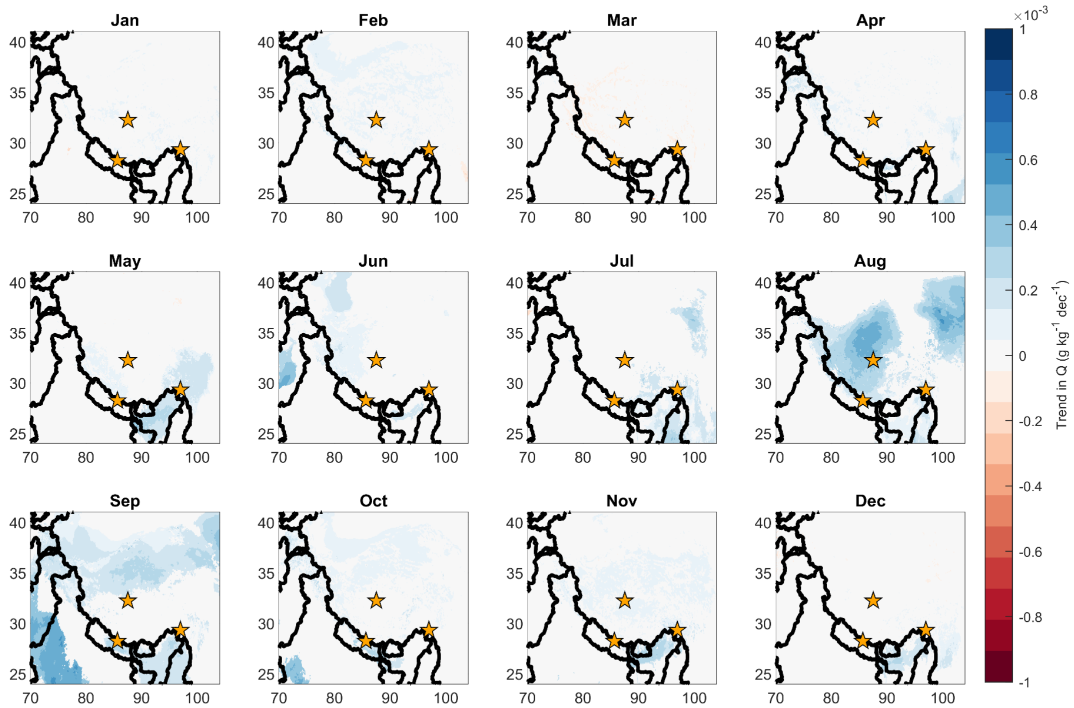

Fig. S34: As Fig. S30, but for decadal trends in mean monthly specific humidity (g kg^{-1}).

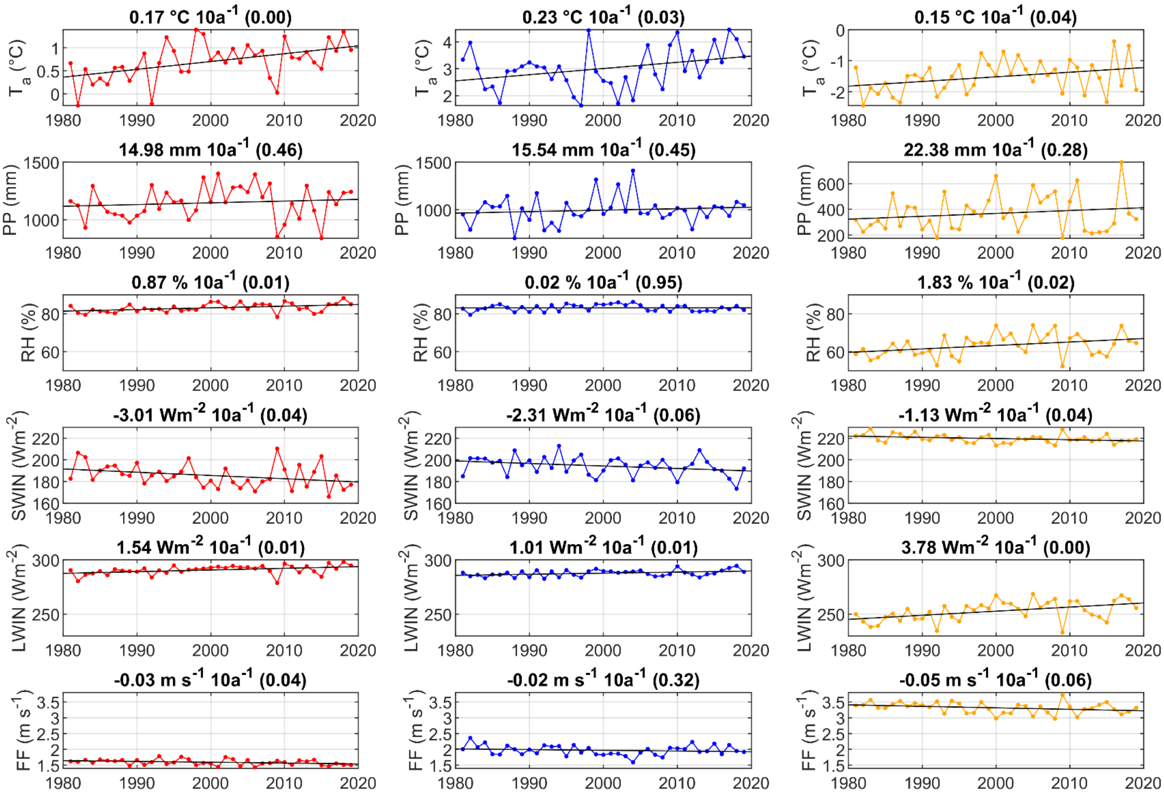

Fig. S35: Point-based trends in mean WRF meteorology during the monsoon at YALA (red), PAR4 (blue) and MUGA (orange) AWS locations.Trends top-to-bottom are for: TA, PP, RH, SWIN, LWIN and FF. Trends per decade and p-values derived from a linear regression model (in parentheses) are given in the header. Y-axis scales for TA and PP are not equal.

S3.2) Relationship of meteorology and the monsoon

Fig. S36 shows the correlation of monsoon characteristics with JJAS air temperature and precipitation. Expanding on the contrasting relationship of meteorology with the monsoon onset (as in Fig. 2), the connection of monsoon duration (controlled strongly by the cessation date - Fig. S27) and air temperature is more consistent across the whole HMA, with a notable difference from the lowland regions of northern India. In the south-east, an expanding monsoon results in an increase of cloudiness, lowering the maximum temperatures and raising the minimum and mean temperatures. Conversely, a longer monsoon duration and later cessation date produces increased precipitation for PAR4 and the southeastern Tibetan Plateau (consistent with the early 2000's wetter period - Fig. 2 + 3), but this pattern reverses toward central Tibet, suggestive of the weakening, yet lengthening of the monsoon (Bollasina et al., 2011). Evidence from Fig. S37, however, also indicates that years within earlier monsoon onset (green stars) and longer monsoon duration also coincided with increases in the early spring precipitation for PAR4 in particular. This emphasises that the interaction of pre-monsoon conditions and monsoon arrival produce a complex variability in surface and energy balance conditions during the monsoon.

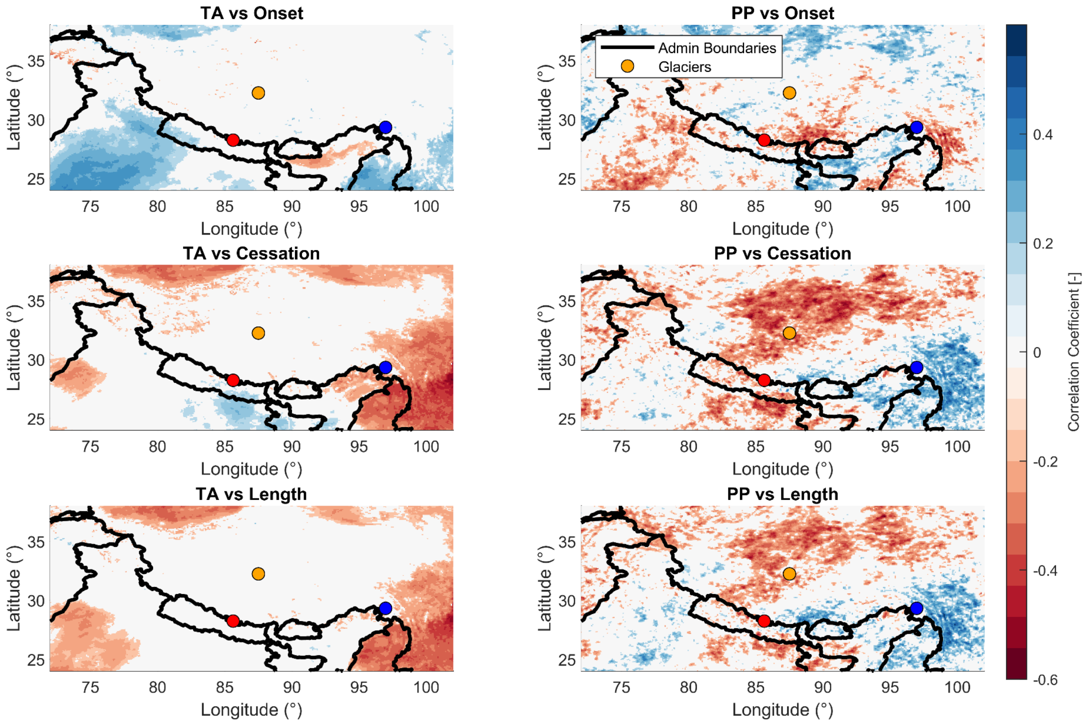

Fig.S36: Pearson correlations between mean JJAS air temperature (left) and total precipitation (right) and the monsoon onset DOY (top), cessation DOY (middle) and length (bottom). Areas not significant to the 0.8 level are shown in white (zero correlation).

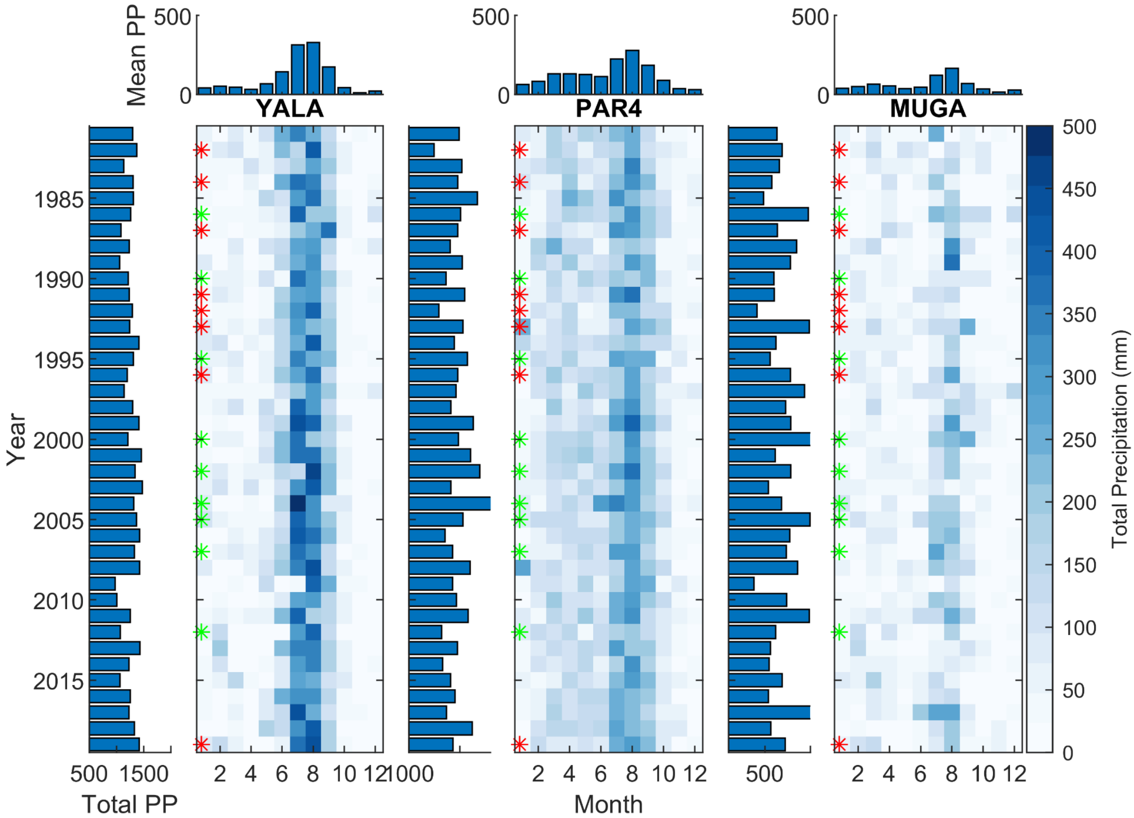

Fig.S37: The occurrence of precipitation by months and year at the three glacier study sites. The coloured grids indicate the total precipitation of each month in each year, whereas the horizontal bars show the summed annual totals, and vertical bars above show the monthly mean precipitation totals. Green and red stars indicate the early and late monsoon onset years, respectively.

S3.3) Energy/mass balance and the monsoon at individual sites

Fig. S38 shows the inter-annual variability in the key energy fluxes at each glacier. While the different energy balance characteristics of each site are quite apparent, the inter-annual variability in mean fluxes is relatively muted. Though the early 2000's period highlights a modification of net shortwave radiation for PAR4, YALA reveals the strongest fluctuations in net radiation, especially for the early 2010's. These differences for MUGA are highlighted by larger longwave losses and positive sensible heat fluxes, resulting in a small net energy surplus available for melting.

The surface melting is strongly controlled by albedo and related to the fraction of solid precipitation (Fig. S39). While the elevation of MUGA produces only subtle changes to the lowest elevation, the snow fraction for PAR4 emphasises its high sensitivity to prevailing conditions and increasing temperatures over a larger elevation range (Jouberton et al., 2022).

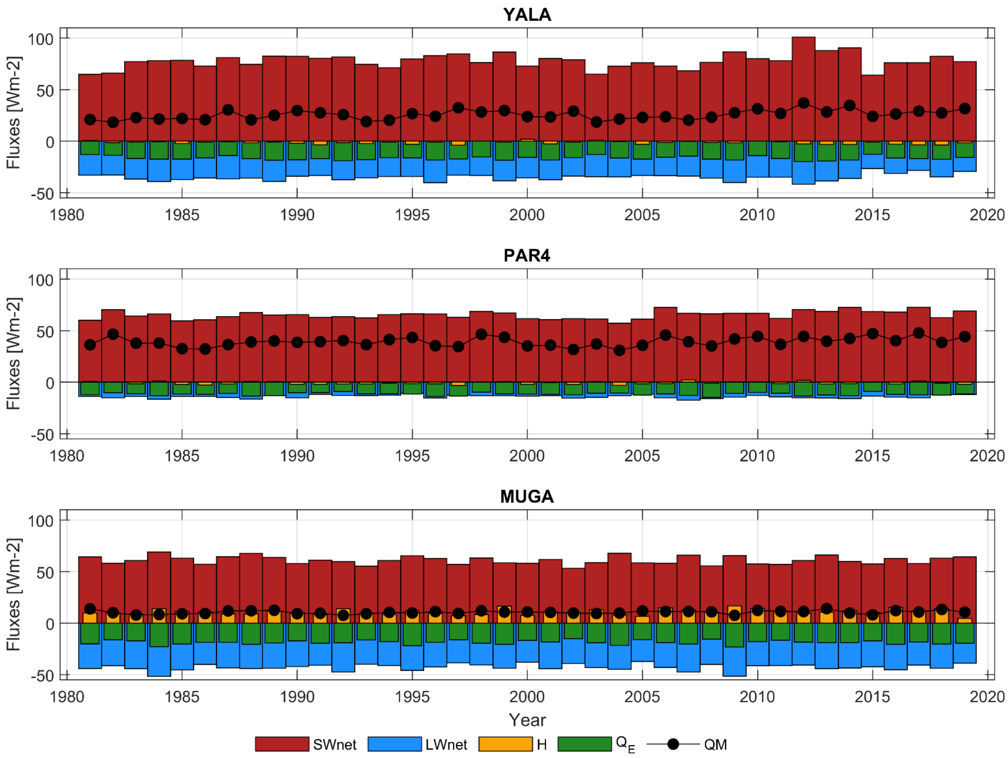

Fig.S38: The mean energy fluxes per year at YALA (top), PAR4 (middle) and MUGA (bottom). The energy available for melt (QM) is a product of the net shortwave (SWnet), longwave (LWnet), sensible (H) and latent (Q_E) heat fluxes and heat flux to the ground (not shown).

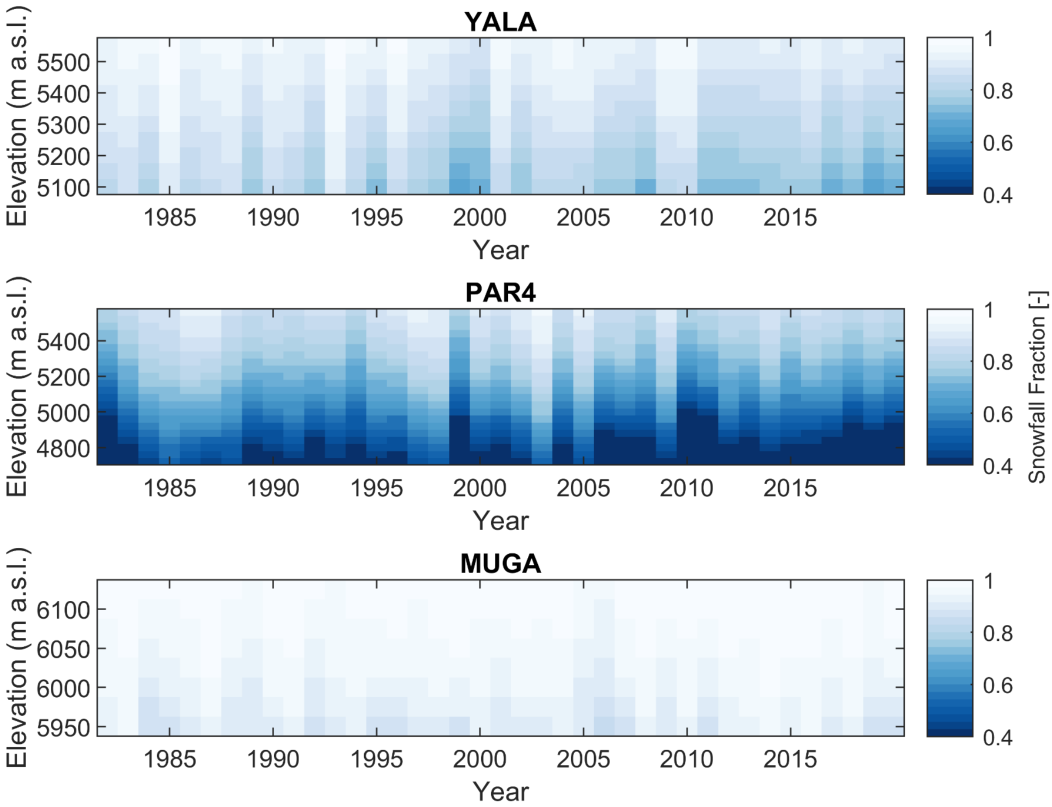

Fig.S39: The snowfall solid fraction (1= snow / 0 = rain) for each year and elevation band at YALA (top), PAR4 (middle) and MUGA (bottom).

Fig.s S40-42 expand on the monsoon's relation to summer (JJAS) energy and mass balance at the different glaciers (Fig. 5). For PAR4, a later monsoon arrival results in less precipitation falling as snow, lower net shortwave and higher melt (Fig. S40) while a later cessation date and longer duration generally increase the mean temperatures and prolong the period of melting (Fig.s S41 and S42). For YALA and MUGA, a late monsoon onset has less impact upon the net shortwave radiation (Fig. S40), though early onset, later cessation and thus longer duration has a stronger control on the melting of the glacier through warmer average conditions and a shift toward more positive LWnet. Accordingly, a later monsoon more often coincides with more positive mass balances at YALA due to the contraction of the warmer and wetter monsoon period. At MUGA, the impact of the monsoon has a less clear signal. Shorter monsoon periods and earlier cessation dates result in the promotion of cooler, yet sunnier conditions which, combined with stronger westerly winds after monsoon cessation generates higher rates of sublimation (Fig. S41). Nevertheless, this effect does not translate into a clear signal of mass balance resulting from the monsoon due to the comparable absolute values of sublimation.

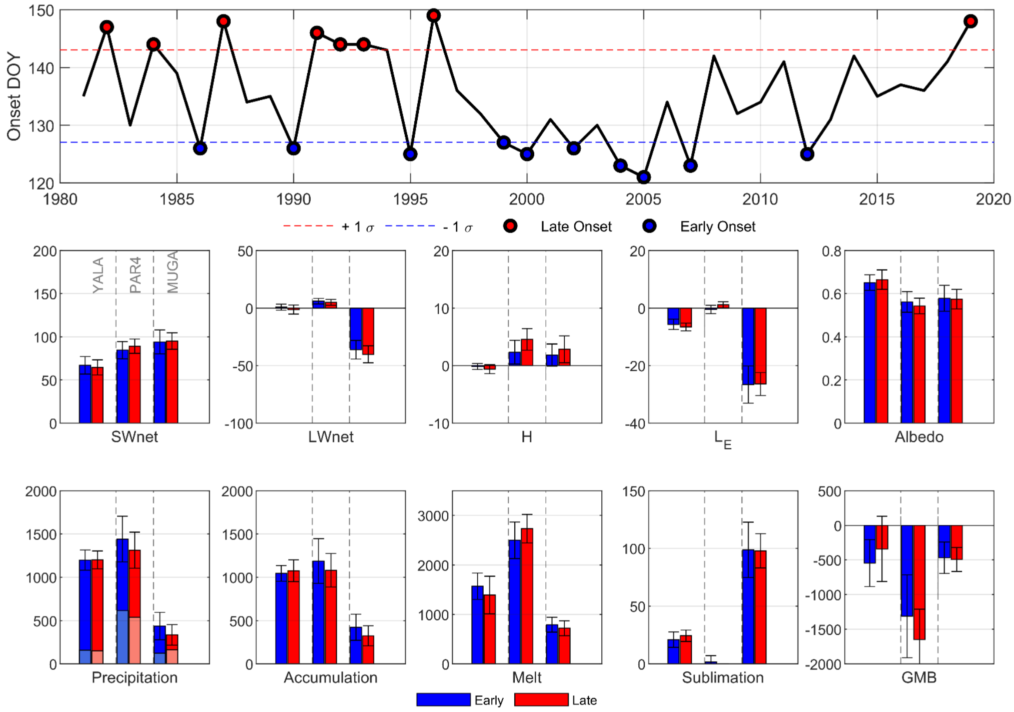

Fig.S40: Variability in the onset date of the monsoon (top panel) and mean (bar) and standard deviations (error bar) of energy fluxes (middle) and mass fluxes (bottom) for the JJAS period. Blue bars indicate the mean conditions for early monsoon onset years and red for late onset years. For precipitation, faded bars indicate the variability in pre-monsoon precipitation for early and late onset years.

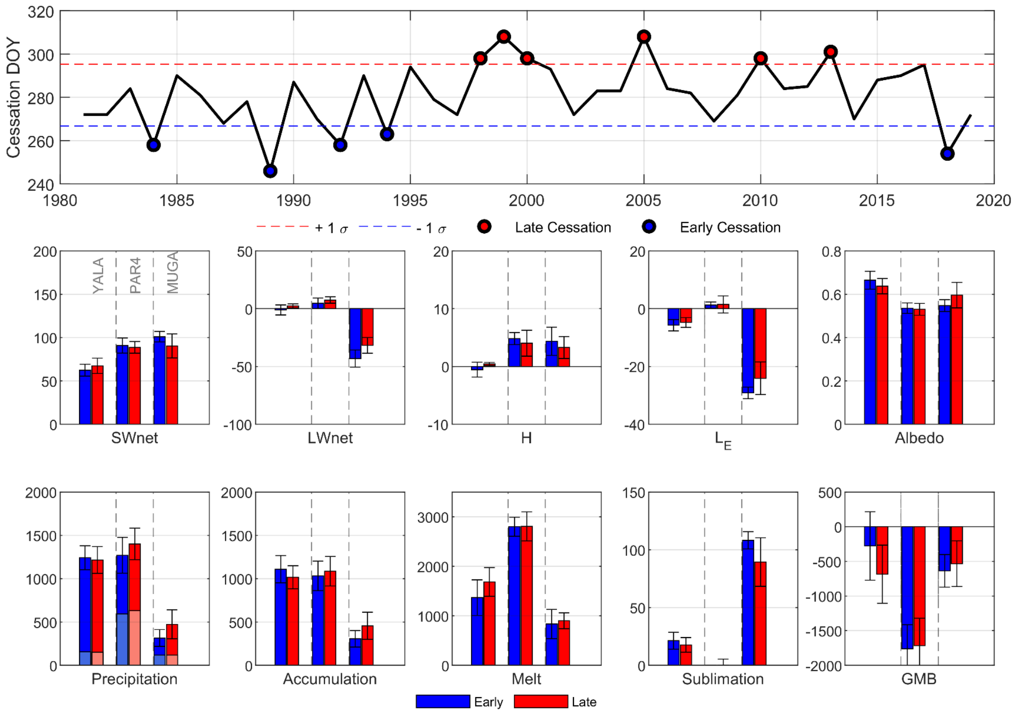

Fig.S41: As Fig. S40, but for early and late monsoon cessation years.

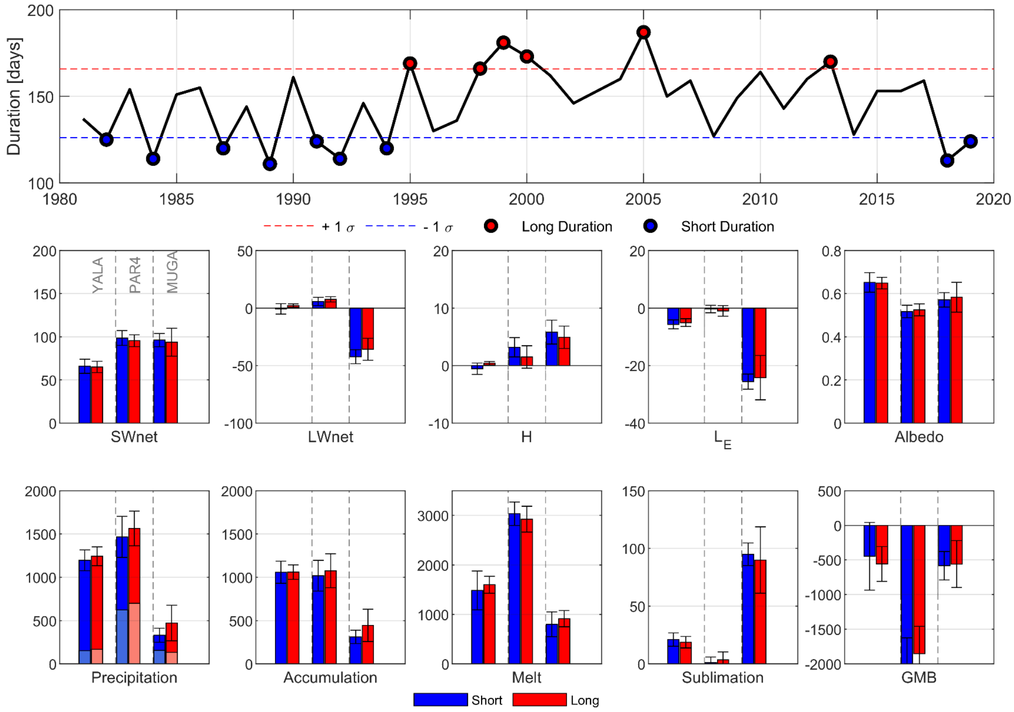

Fig.S42: As Fig. S40, but for short (blue) and long (red) monsoon duration years.

The correlations plots in Fig. S43 show that seasonal meteorological conditions can be explain much of the variance of inter-annual mass balance at all sites, though the direct influence of monsoon timing and intensity is less clear. Comparing to Fig. 5, a late monsoon onset at Parlung produces a consistently negative mass balance response due to the reduction of precipitation and the resultant lower albedo and high net shortwave radiation (Fig. S43). However, a highly variable response to an early monsoon arrival produces a poor overall correlation to the timing of onset as a metric to determine annual glacier health. Partly due to the May-June transition and monsoon arrival (Fig. 4), pre-monsoon snowfall and monsoon snowfall relate well to glacier mass balance, again because of the control on surface albedo. Fig. 43 highlights the different conditions of the three sites, whereby latent heat fluxes and sublimation are more dominant at Mugagangqiong and air temperature and sensible heat fluxes are more evident at parlung 4 and Yala.

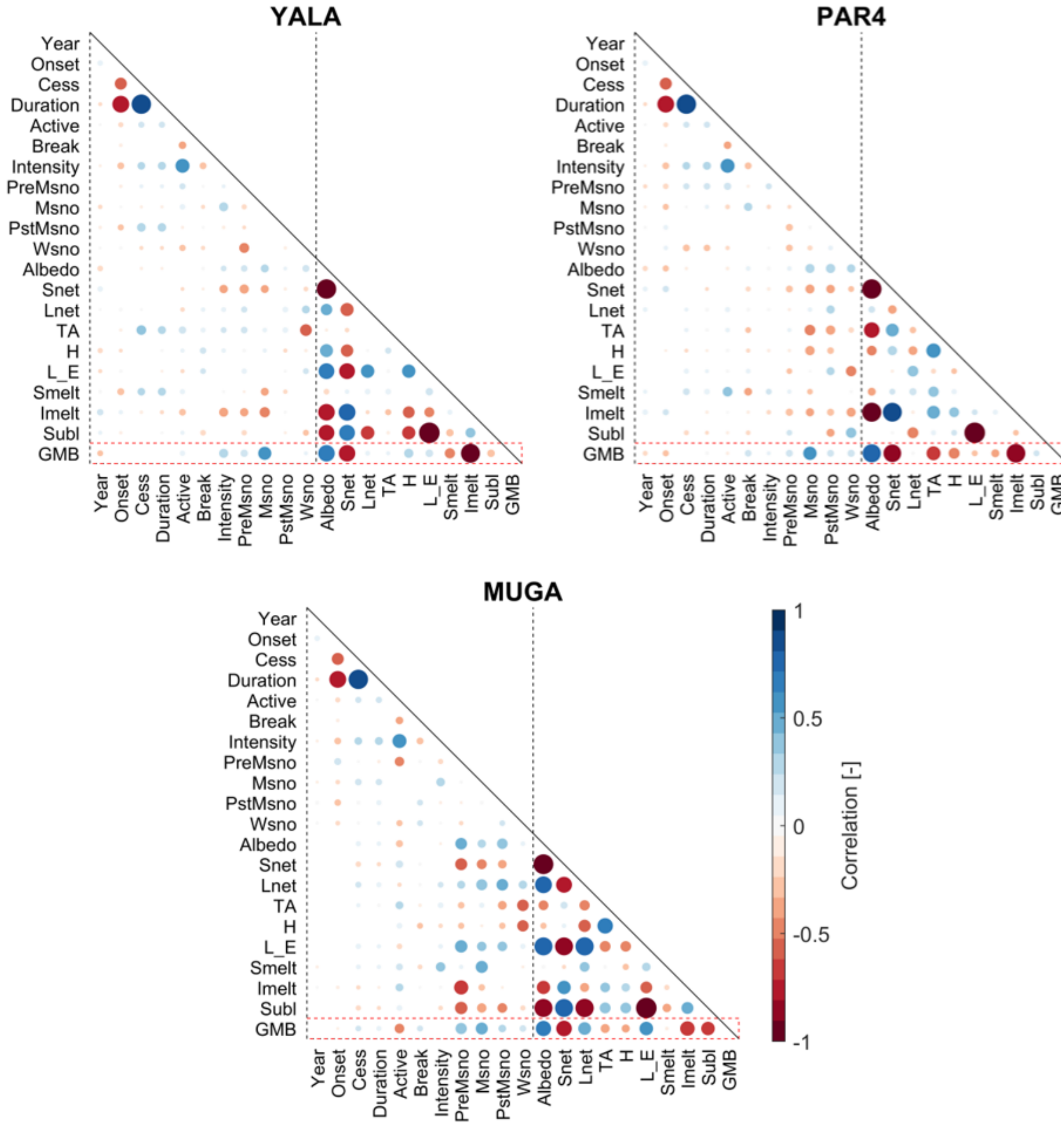

Fig. S43: Correlation of monsoon characteristics, mass and energy fluxes at each glacier study site during JJAS. Circle size and colour indicates the magnitude and sign of pearson correlations. Variables to the left of the vertical line indicate those related to monsoon characteristics and seasonality. "PreMsno", "Msno", "PostMsno" and Wsno" refer to pre-monsoon, monsoon, post-monsoon and winter snow, respectively. Variables to the right of the vertical line represent energy and mass balance components where: "Alb" = albedo, "TA" = temperature, "Snet" = net shortwave radiation, "Lnet" = net longwave radiation, "H" = sensible heat flux, "L_E" = latent heat flux, "Smelt", "Imelt" and "Tmelt" = snow, ice and total melt, "Subl" = sublimation and "GMB" = glacier mass balance. Non-significant correlations are shown by the smallest circle size, but are retained to highlight the relationships between all variables.

Altitudinal patterns of glacier mass balance highlight the high mass turnover of PAR4 compared with YALA and MUGA (Fig. S44). While MUGA is losing mass at a low rate due to its high elevation and balance of low temperatures and dry, continental conditions, YALA's negative mass balance is the product of its size and limited accumulation area. Unlike these glaciers, PAR4 experiences greater mass loss for years where the monsoon arrives late (Fig. S44b), largely related to the differences in surface albedo (Fig. S44i), especially between

5000-5400 m a.s.l. While increasing temperatures and reduced solid fraction of precipitation are largely responsible for the increased mass loss since 2005 at PAR4 (Jouberton et al., 2022, Fig. S39), increased precipitation (Fig. 1b) accounts for an average albedo increase of 0.06 for early monsoon onset years compared to late monsoon onset years. YALA's mass balance is more variable for late arrival of the monsoon, though in general, there are no strong differences in the response of the glacier surface albedo for the monsoon's arrival date.

Assessing the pre-monsoon to monsoon transition period (May-June), reveals an interesting balance of snowfall timing and amount in determining the early monsoon surface conditions (Fig. 4, Fig. S45). As demonstrated in Fig. 4, a late monsoon results in consistently reduced precipitation for the whole period at PAR4, whereas at YALA a later monsoon merely shifts the snowfall later, but results in more overall solid precipitation for the May-June period because of cooler conditions and the promotion of more snowfall. For MUGA, this pattern is reversed, whereby late monsoon arrival relates to higher total snowfall on the glacier, as a result of westerly storms being more dominant in the monsoon onset months. Fig. S45 highlights that these features are consistent when only considering pre-2000 years of the simulation, such that the observed behaviours are not influenced notably by the long-term warming trend across HMA.

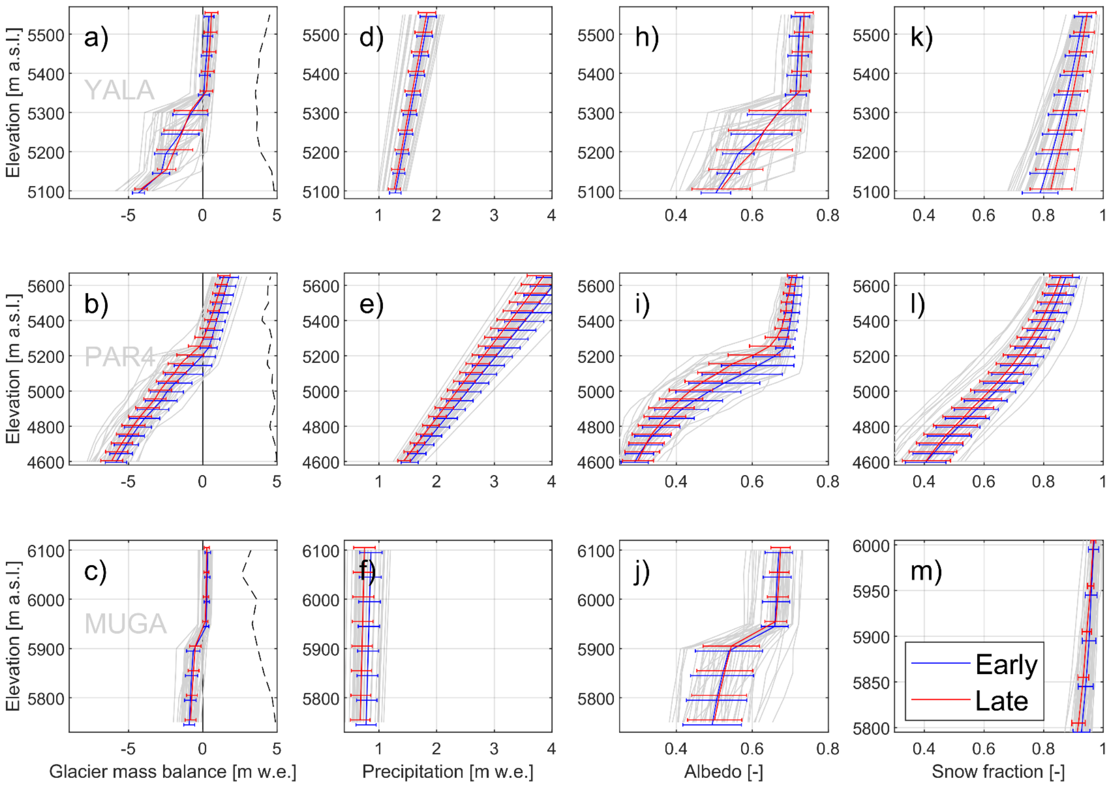

Fig. S44: Altitudinal patterns of annual glacier mass balance (a-c), total precipitation (d-f), annual-average albedo (h-j) and snow fraction (k-m) for YALA (a,d,h,k), PAR4 (b,e,i,l) and MUGA (c,f,j,m). Individual years are plotted in grey with blue and red error bars representing the mean and standard deviation of early and late monsoon years, respectively. Early and late monsoon years are *classified as those which exceed minus or plus one standard deviation from the mean of onset dates, respectively.*

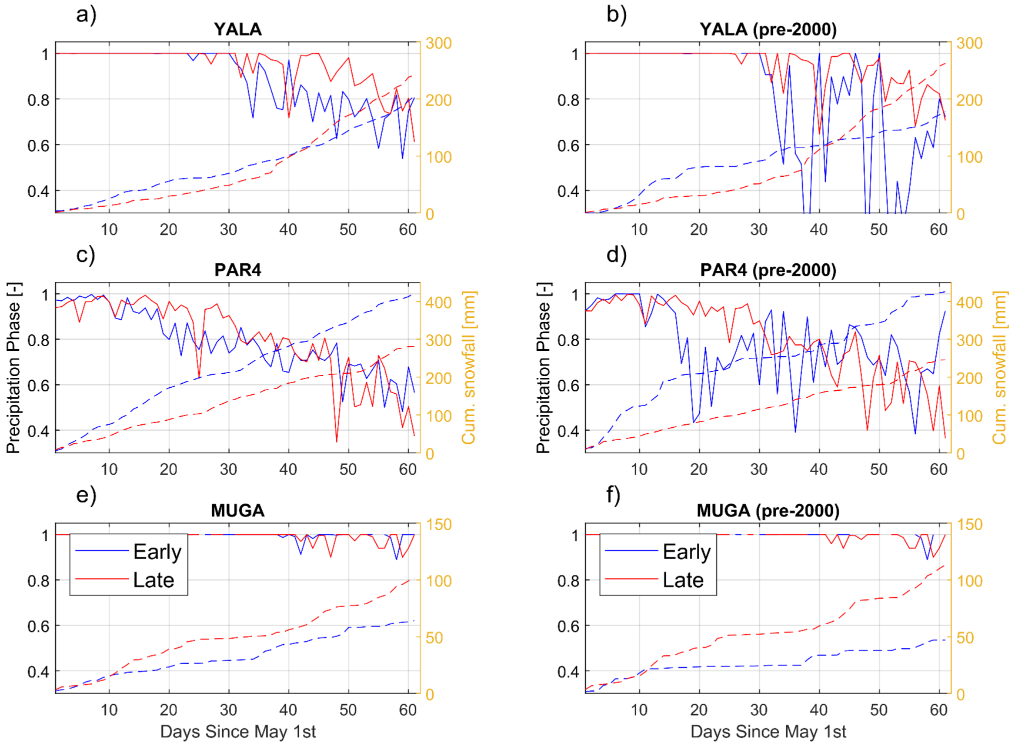

Fig.S45: As Fig. 4 of the main text, but also considering only early and late monsoon years of the pre-2000 period (see Fig. S40).

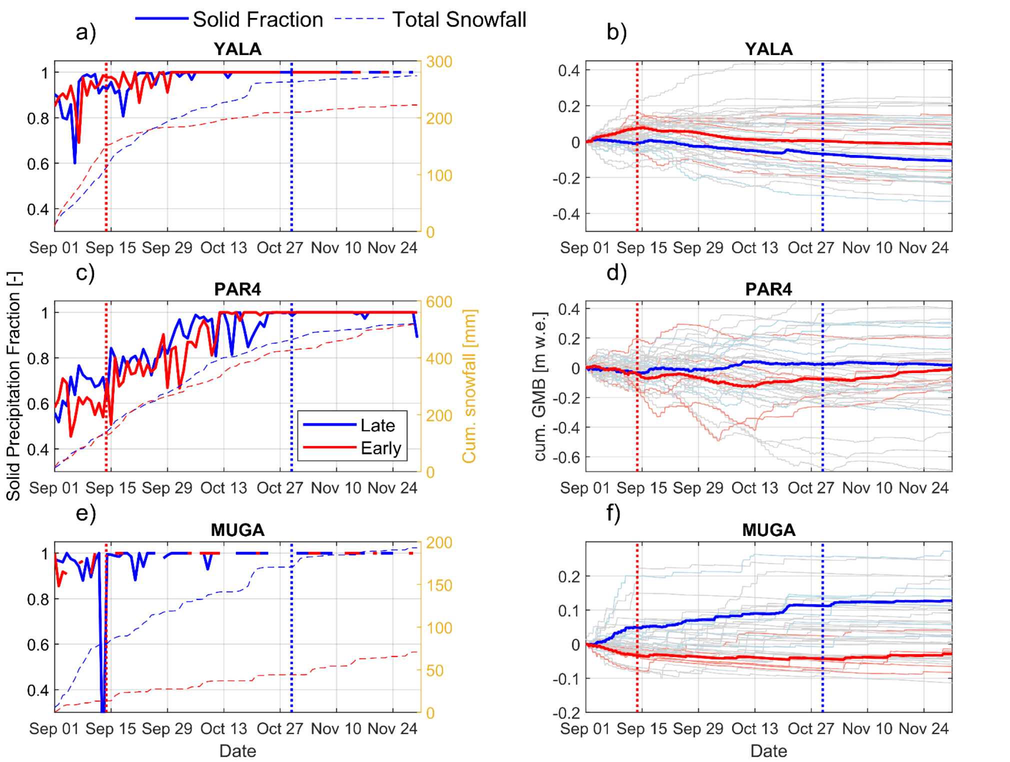

Fig. S46: As Fig. 4 of the main text, but demonstrating the cessation period and energy/mass *balances for the September-November period. Vertical dashed lines indicate the mean late (blue) and early (red) cessation dates.*

To support the meteorological conditions experienced during certain monsoon years, we additionally demonstrate the cumulative air temperatures and precipitation amounts occurring during the early and late monsoon onset (Fig. S47) and early vs late cessation (Fig. S48). These Fig.s highlight that the correlations between monsoon onset and glacier mass balance (e.g. Fig. 5) are due to non-significant differences in the meteorological conditions at Yala especially. Nevertheless a late onset for Parlung 4 resulted in more negative mass balances (Fig. 4), especially given the greater sensitivity to precipitation changes over a large elevation range (e.g. Fig. S44).

Conversely, the mass balances of Yala and Mugagangqiong glaciers are more responsive to a late monsoon cessation, but for different reasons: a later cessation relates to increased air temperatures (Fig. S43, Fig. S48a) which drives more melting and more negative mass balances (Fig. S46b); for Mugagangqiong, a later cessation date provides a longer period with precipitation (Fig. S48f), and thus produces a more positive mass balance. For the latter, a clear signal of increased albedo is evident (Fig. S48l), despite that no notable changes in precipitation phase are evident at high elevations.

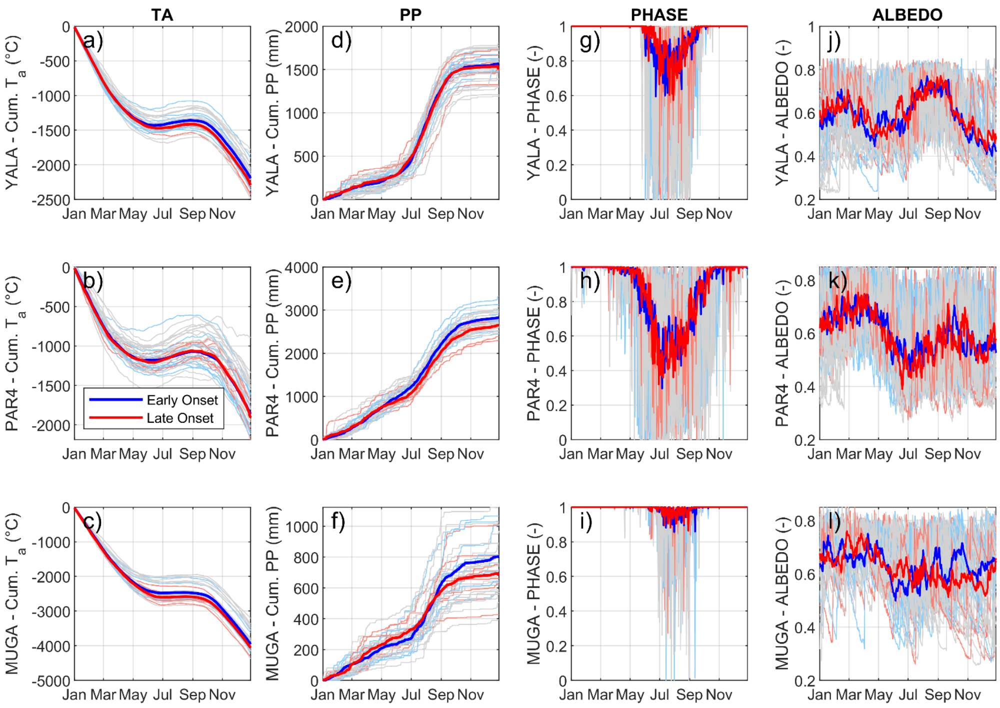

Fig. S47: The cumulative air temperatures (a-c), cumulative total precipitation (d-f), precipitation phase (g-i) and albedo (j-l) for Yala (top), Parlung 4 (middle) and Mugaganqiong (bottom). The anomalously early (late) onset years (+/- one standard deviation from mean of all years) are indicated by the light blue (red) lines and the mean of those conditions are shown by the bold coloured lines.

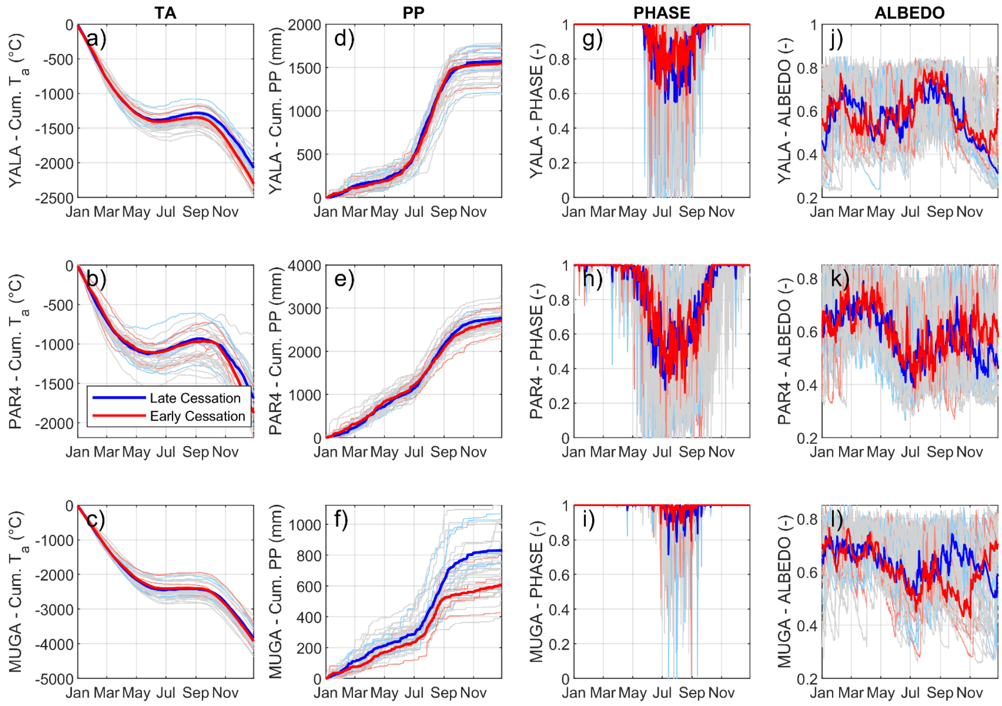

Fig. S48: The cumulative air temperatures (a-c), cumulative total precipitation (d-f), precipitation phase (g-i) and albedo (j-l) for Yala (top), Parlung 4 (middle) and Mugaganqiong (bottom). The anomalously late (early) cessation years (+/- one standard deviation from mean of all years) are indicated by the light blue (red) lines and the mean of those conditions are shown by the bold coloured lines.

Presenting these same elements against anomalously negative mass balance years (Fig. S49) reveals a clear pattern of decreased precipitation and increased temperatures for more negative mass balance years. The drivers of which are notably the reduced surface albedo (Fig. S49j-l) and increased shortwave radiation (Fig. S50a-c). Turbulent fluxes are notably more negative for high mass loss years at Yala (Fig. S50), largely due to the dominance of clearer skies and increased shortwave vs longwave heat fluxes. For Tibetan sites, sensible heat fluxes are generally much greater and contribute more to mass loss in the most negative years. Because mass loss is highly driven by albedo and shortwave radiation, the contribution of a decreasing precipitation phase (i.e. a shift to more liquid precipitation) is particularly noteworthy. This is especially the case for Parlung 4 (Fig. S39 - Jouberton et al., in press) where the solid fraction of precipitation can explain 41% of the variance of glacier mass balance, after accounting for air temperature itself (pearson partial correlation p = 0). For Yala this change in phase can explain around 21% of the glacier mass balance variability, while the relationship is negligible for Mugagangqoing, where the phase of precipitation is largely unaffected (Fig. 4).

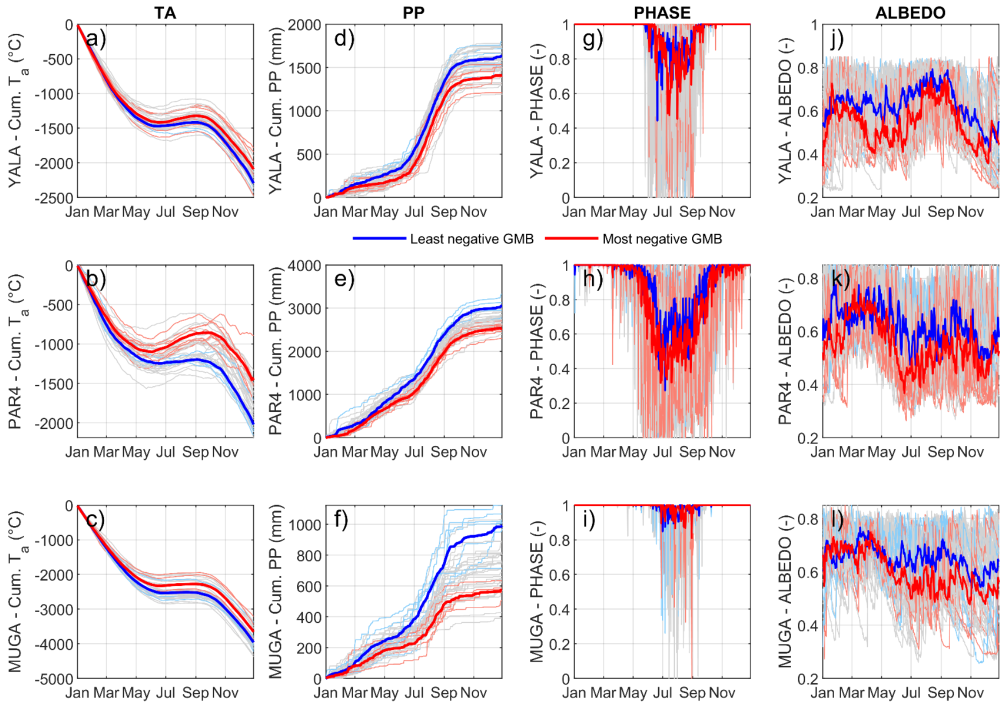

Fig. S49: The cumulative air temperatures (a-c), cumulative total precipitation (d-f), precipitation phase (g-i) and albedo (j-l) for Yala (top), Parlung 4 (middle) and Mugagangqiong (bottom). The least (most) negative glacier mass balance years (+/- one standard deviation from mean of all years) are indicated by the light blue (red) lines and the mean of those conditions are shown by the bold coloured lines.

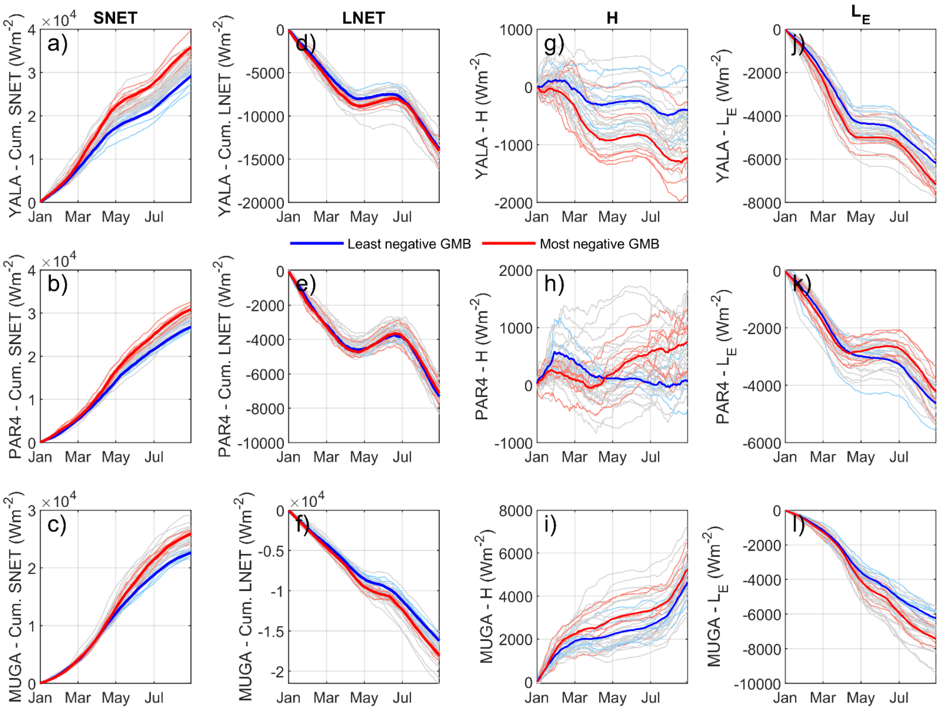

Fig. S50: The cumulative net shortwave radiation (a-c), cumulative net longwave radiation (d-f), cumulative sensible heat fluxes (g-i) and cumulative latent heat fluxes (j-l) for Yala (top), Parlung 4 (middle) and Mugagangqiong (bottom). The least (most) negative glacier mass balance years (+/- one standard deviation from mean of all years) are indicated by the light blue (red) lines and the mean of those conditions are shown by the bold coloured lines.

References

Baker D G, Ruschy D L and Wall D B 1990 The Albedo of Prairie Snows J. Appl. Meteorol. 28 189–97

Bollasina M A, Ming Y and Ramaswamy V 2011 Anthropogenic aerosols and the weakening of the south asian summer monsoon Science (80-.). 334 502–5

Bonekamp P N J, Collier E and Immerzeel W 2018 The Impact of spatial resolution, land use, and spinup time on resolving spatial precipitation patterns in the Himalayas J. Hydrometeorol. 19 1565–81

Cannon A J 2018 Multivariate quantile mapping bias correction: an N-dimensional probability density function transform for climate model simulations of multiple variables Clim. Dyn. 50 31–49

Collier E and Immerzeel W W 2015 High-resolution modeling of atmospheric dynamics in the Nepalese Himalaya J. Geophys. Res. Atmos. 175 238

Corripio J G 2003 Vectorial algebra algorithms for calculating terrain parameters from dems and solar radiation modelling in mountainous terrain Int. J. Geogr. Inf. Sci. 17 1–23

Ding B, Yang K, Qin J, Wang L, Chen Y and He X 2014 The dependence of precipitation types on surface elevation and meteorological conditions and its parameterization J. Hydrol. 513 154–63 Online: http://dx.doi.org/10.1016/j.jhydrol.2014.03.038

Ding B, Yang K, Yang W, He X, Chen Y, Lazhu, Guo X, Wang L, Wu H and Yao T 2017 Development of a Water and Enthalpy Budget-based Glacier mass balance Model (WEB-GM) and its preliminary validation Water Resour. Res. 53 3146–78

Fatichi S, Ivanov V Y and Caporali E 2012 A mechanistic ecohydrological model to investigate complex interactions in cold and warm water-controlled environments: 2. Spatiotemporal analyses J. Adv. Model. Earth Syst. 4

Fugger S, Fyffe C, Fatichi S, Miles E, McCarthy M, Shaw T, Ding B, Yang W, Wagnon P, Immerzeel W, Liu Q and Pellicciotti F 2021 Understanding monsoon controls on the energy and mass balance of Himalayan glaciers Cryosph. Discuss. 1–46

Fujita K and Nuimura T 2011 Spatially heterogeneous wastage of Himalayan glaciers Proc. Natl. Acad. Sci. U. S. A. 108 14011–4

Fujita K, Takeuchi N and Seko K 1998 Glaciological observations of Yala Glacier in Langtang Valley, Nepal Himalayas, 1994 and 1996 Bull. Glacier Res. 16 75–81

Fyffe C L, Potter E, Fugger S, Orr A, Fatichi S, Loarte E, Medina K, Hellström R Å, Bernat M, Aubry‐Wake C, Gurgiser W, Perry L B, Suarez W, Quincey D J and Pellicciotti F 2021 The Energy and Mass Balance of Peruvian Glaciers J. Geophys. Res. Atmos. 126 1–22

Hugonnet R, McNabb R, Berthier E, Menounos B, Nuth C, Girod L, Farinotti D, Huss M, Dussaillant I, Brun F and Kääb A 2021 Accelerated global glacier mass loss in the early twenty-first century Nature 592 726–31 Online: http://dx.doi.org/10.1038/s41586-021-03436-z

Immerzeel W W, Petersen L, Ragettli S and Pellicciotti F 2014 The importance of observed gradients of air temperature and precipitation for modeling runoff from a glacierised watershed in the Nepalese Himalayas Water Resour. Res. 50 2212–26

Jouberton, A., Shaw, T. E., Miles, E. S., McCarthy, M. J., Fugger, S., Ren, S., Dehecq, A., Yang, W., & Pellicciotti, F. (in press). Warming-induced monsoon precipitation phase change intensifies glacier mass loss in the southeastern Tibetan Plateau. Proceedings of the National Academy of Sciences. https://doi.org/10.1073/pnas.XXXXXXXXXX

Kattel D B, Yao T, Yang K, Tian L, Yang G and Joswiak D 2012 Temperature lapse rate in complex mountain terrain on the southern slope of the central Himalayas Theor. Appl. Climatol. 113 671–82 Online: http://link.springer.com/10.1007/s00704-012-0816-6

Mastrotheodoros T, Pappas C, Molnar P, Burlando P, Manoli G, Parajka J, Rigon R, Szeles B, Bottazzi M, Hadjidoukas P and Fatichi S 2020 More green and less blue water in the Alps during warmer summers Nat. Clim. Chang. 10 155–61 Online: http://dx.doi.org/10.1038/s41558-019-0676-5

Maurer J M, Schaefer J M, Rupper S and Corley A 2019 Acceleration of ice loss across the Himalayas over the past 40 years Sci. Adv. 5 1–12

Mölg T, Maussion F, Yang W and Scherer D 2012 The footprint of Asian monsoon dynamics in the mass and energy balance of a Tibetan glacier Cryosph. 6 1445–61 Online: http://www.the-cryosphere.net/6/1445/2012/

Mölg T, Maussion F and Scherer D 2014 Mid-latitude westerlies as a driver of glacier variability in monsoonal High Asia Nat. Clim. Chang. 4 68–73

Ou T, Chen D, Chen X, Lin C, Yang K, Lai H W and Zhang F 2020 Simulation of summer precipitation diurnal cycles over the Tibetan Plateau at the gray-zone grid spacing for cumulus parameterization Clim. Dyn. 54 3525–39 Online: https://doi.org/10.1007/s00382-020-05181-x

Prasad V S and Hayashi T 2005 Onset and withdrawal of Indian summer monsoon Geophys. Res. Lett. 32 1–5

Ragettli S, Pellicciotti F, Immerzeel W W, Miles E, Petersen L, Heynen M, Shea J M, Stumm D, Joshi S and Shrestha A B 2015 Unraveling the hydrology of a Himalayan watershed through integration of high resolution in- situ data and remote sensing with an advanced simulation model Adv. Water Resour. 78 94–111 Online: http://dx.doi.org/10.1016/j.advwatres.2015.01.013

Ren S, Menenti M, Jia L, Zhang J and Zhang J 2020 Glacier Mass Balance in the Nyainqentanglha Mountains between 2000 and 2017 Retrieved from ZiYuan-3 Stereo Images and the SRTM DEM Remote Sens. 12

Ren S, Miles E S, Jia L, Menenti M, Kneib M, Buri P, Mccarthy M J, Shaw T E, Yang W and Pellicciotti F 2021 Anisotropy Parameterization Development and Evaluation for Glacier Surface Albedo Retrieval from Satellite Observations Remote Sens. 13 1–29

Ren Y Y, Ren G Y, Sun X B, Shrestha A B, You Q L, Zhan Y J, Rajbhandari R, Zhang P F and Wen K M 2017 Observed changes in surface air temperature and precipitation in the Hindu Kush Himalayan region over the last 100-plus years Adv. Clim. Chang. Res. 8 148–56 Online: https://doi.org/10.1016/j.accre.2017.08.001

Shaw T, Yang W, Ayala Á, Bravo C, Zhao C and Pellicciotti F 2021 Distributed summer air temperatures across mountain glaciers in the south-east Tibetan Plateau: temperature sensitivity and comparison with existing glacier datasets Cryosph. 15 595–614

Shean D E, Alexandrov O, Moratto Z M, Smith B E, Joughin I R, Porter C and Morin P 2016 An automated, open-source pipeline for mass production of digital elevation models (DEMs) from very-high-resolution commercial stereo satellite imagery ISPRS J. Photogramm. Remote Sens. 116 101–17 Online: http://dx.doi.org/10.1016/j.isprsjprs.2016.03.012

Shean D E, Bhushan S, Montesano P, Rounce D R, Arendt A and Osmanoglu B 2020 A Systematic , Regional Assessment of High Mountain Asia Glacier Mass Balance Front. Earth Sci. 7 1–19

Smith T and Bookhagen B 2018 Changes in seasonal snow water equivalent distribution in High Mountain Asia (1987 to 2009) Sci. Adv. 4 1–8

Steiner J F, Gurung T R, Joshi S P, Koch I, Saloranta T, Shea J, Shrestha A B, Stigter E and Immerzeel W W 2021 Multi-year observations of the high mountain water cycle in the Langtang catchment, Central Himalaya Res. Obs. Catchments 35 1–7

Stigter E E, Litt M, Steiner J F and Bonekamp P N J 2018 The Importance of Snow Sublimation on a Himalayan Glacier Front. Earth Sci. 6 1–16

Stumm D, Joshi S P, Gurung T R and Silwal G 2020 Mass balances of Yala and Rikha Samba Glacier, Nepal from 2000 to 2017 Earth Syst. Sci. Data Discuss. 1–37

Sugiyama S, Fukui K, Fujita K, Tone K and Yamaguchi S 2013 Changes in ice thickness and flow velocity of Yala Glacier, Langtang Himal, Nepal, from 1982 to 2009 Ann. Glaciol. 54 157–62

Sunako S, Fujita K, Izumi T, Zamaguchi S, Sakai A and Kayastha R 2020 Up-glacier propagation of surface lowering of Yala Glacier, Langtang Valley, Nepal Himalaya J. Glaciol. 3–29

Verseghy D L 1991 Canadian Land Surface Scheme for GCMS. I. Soil Model Int. J. Climatol. 11 111–33

Wilcke R A I, Mendlik T and Gobiet A 2013 Multi-variable error correction of regional climate models Clim. Change 120 871–87

Xu B Q, Wang M, Joswiak D R, Cao J J, Yao T D, Wu G J, Yang W and Zhao H B 2009 Deposition of anthropogenic aerosols in a southeastern Tibetan glacier J. Geophys. Res. Atmos. 114 1–8

Yang W, Zhu M, Guo X and Zhao H 2021 Air temperature variability in high-elevation glacierized regions: observations from six catchments on the Tibetan Plateau J. Appl. Meteorol. Climatol. 1–35

Zhu M, Yao T, Yang W, Maussion F, Huintjes E and Li S 2015 Energy- and mass-balance comparison between Zhadang and Parlung No. 4 glaciers on the Tibetan Plateau J. Glaciol. 61 595–607 Online: http://www.igsoc.org/journal/61/227/j14j206.html